## Title

SEARCH FOR THE GAMMA-BRANCH OF THE SHAPE ISOMERS OF SEPARATED U ISOTOPES USING MUON FOR NUCLIDE EXCITATION



## Author

Mireshghi, A.

## Publication Date

1982-12-01

# Lawrence Berkeley Laboratory
UNIVERSITY OF CALIFORNIA

## Physics, Computer Science & Mathematics Division

SEARCH FOR THE GAMMA-BRANCH OF THE SHAPE ISOMERS OF SEPARATED U ISOTOPES USING MUON FOR NUCLIDE EXCITATION

Ali Mireshghi
(Ph.D. Thesis)

December 1982



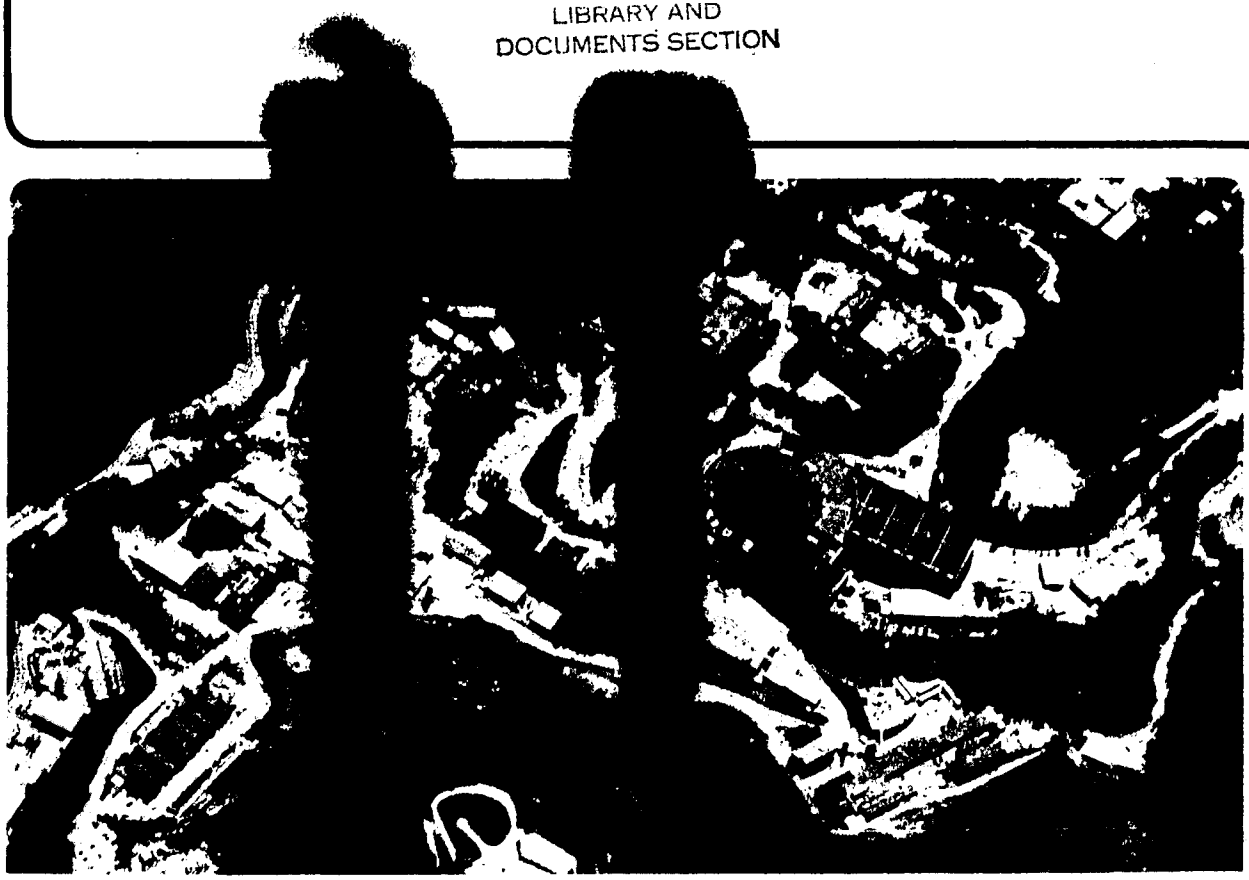



Prepared for the U.S. Department of Energy under Contract DE-AC03-76SF00098

## DISCLAIMER

LBL-15438

# SEARCH FOR THE GAMMA-BRANCH OF THE SHAPE ISOMERS OF SEPARATED U ISOTOPES USING MUON FOR NUCLIDE EXCITATION

By

Ali Mireshghi
(Ph.D. Thesis)

Lawrence Berkeley Laboratory
University of California
Berkeley, California 94720

December 1982

This work was supported by the Director, Office of Energy Research, Office of High Energy and Nuclear Physics, Division of High Energy Physics of the U.S. Department of Energy under Contract Number DE-AC03-76SF00098.

# SEARCH FOR THE GAMMA-BRANCH OF THE SHAPE ISOMERS OF THE SEPARATED U ISOTOPES USING MUON FOR NUCLIDE EXCITATION

By

Ali Mireshghi

## ABSTRACT

We have searched for back-decay gamma rays from the shape isomeric states in $^{235}U$, $^{236}U$, and $^{238}U$ possibly excited in muon radiationless transition. The energies and intensities of gamma rays following muon atomic capture were measured as a function of time after muon stopping. Background was suppressed by requiring that the candidate gamma ray be followed by another gamma ray ($\mu$-capture gamma ray). The prompt gamma-ray spectra included the U-muonic x rays. The measured $^{235}U$ and $^{238}U$ x-ray energies were in good agreement with previously reported results. The x-ray spectrum from $^{236}U$ has not been previously reported. The $^{236}U$ spectrum is very similar to that of $^{238}U$, except that the K x-rays exhibit an isotope shift of approximately 20 kev, the $^{236}U$ energies being higher.

In the analysis of the delayed spectra of $^{236}U$ and $^{238}U$ using the GAMANL peak searching program, and with an effective lower-limit detection efficiency of .15% per stopping muon, no candidate gamma rays for the back decay transitions from the shape isomeric state were observed. However, a more sensitive hand analysis of the "smoothed background-subtracted" spectra resulted in the identification of some delayed gamma activities close to or below the 0.15% level.

For $^{238}U$ most of the transitions observed could be fitted with a characteristic lifetime of 75 ± 18 ns, consistent with muon capture in $^{238}U$. Three of them, at energies of 685, 817, and 1015 kev have been identified as coming from the interactions of fast neutrons emitted in nuclear muon capture by the target nuclei. The 913 kev transition from the Ge(n,n') reaction was also identified.

For $^{236}U$, 9 out of the 12 observed delayed gamma rays could be fitted to a common lifetime of 66 ± 8 ns, consistent with the $\mu$-capture in $^{236}U$. A line at 1278 matched a transition in $^{235}Pa$, and two lines at 845 and 1626 kev are in good agreement with transitions in $^{234}Pa$. Both nuclei would be produced by muon capture on $^{236}U$.

It is concluded that to a yield below 0.15% per muon stopping, there are no observable gamma ray transitions from U shape isomeric states that may be excited by nonradiative atomic transitions of muons. The time distributions and energies of gamma rays observed at this yield limit indicate that they are from nuclear-capture reactions, and due to accidental delayed coincidences.

Selig N. Kaplan

Professor Selig N. Kaplan
Chairman of Thesis Committee

# TABLE OF CONTENTS

بِسْمِ اللَّهِ الرَّحْمَٰنِ الرَّحِيمِ

*In the name of God, Most Gracious,*
*Most Merciful*

الْحَمْدُ لِلَّهِ الَّذِي عَلَّمَ الْإِنسَانَ مَا لَمْ يَعْلَمْ

*Praise be to God, who taught man which he knew not.*

# ACKNOWLEDGEMENTS

I would like to extend my sincere gratitude and appreciation to Professor Selig N. Kaplan for his guidance, advice and criticism. His support and patience has encouraged me throughout the progress of this work.

I am greatly indebted to Dr. Arthur Olin for his invaluable collaboration in the experiments and his suggestions and discussions during the analysis of the data.

I also appreciate the assistance of Professor George A. Beer and other collaborators in running the experiments.

I would like to thank the members of the thesis committee for their critical reviewing of this dissertation and Dr. Morton S. Weiss for his advices and Jeanne M. Miller for helping with typing parts of this thesis.

I am very pleased to heartfully thank my wife Faranak and sun Abazar for their encouragement and love and my parents for their patience and tolerance during the years I have been away from home.

# CHAPTER 1

# INTRODUCTION

For heavy deformed nuclei the phenomenological Liquid Drop Model (LDM) is unable to explain several important features observed in fission cross sections. The model predicts a smooth single-humped fission barrier, of which the penetrability is a steeply rising function of the incidence energy, with no structure , such as the ones observed in some actinides. Furthermore, there is no starting point, other than the ground state, for the nucleus to grow into larger deformations spontaneously, and end up with fission. Therefore, the concept had to be significantly revised in order to be able to explain the existence of the short-lived spontaneously fissioning species observed in the early sixties. The Nilsson single-particle model (Mottelson *et al.* 1959) based on the deformation dependence of the shell effects had previously explained the non-sphericity of the ground state mid-shell nuclei. The LDM barrier was corrected by incorporating into it the deformation dependence of the single-particle energies calculated as a result of extending the Nilsson single-particle model to large deformations (Strutinsky, 1967; Nilsson *et al.* 1969). The resulting fission barrier for actinide nuclei showed a secondary minimum, a so-called "second well", at a deformation about twice that of the ground state.

The new double-humped concept for the fission barrier paved the way for understanding a large number of puzzling experimental results. The short-lived, spontaneously fissioning isomers, then called "shape isomers", were understood to be deformed states of the nuclei trapped in the second well of the barrier.

The shape isomeric state, with an excitation energy of about 2 to 3 Mev above the ground state, can deexcite either by tunneling through the outer barrier, which results in delayed isomeric fission, or by penetrating the inner barrier and making a transition to the some level in the first well. Experimental investigations of these decay modes of the shape isomeric state, not

only result in confirmation of the double-humped concept, but also serve as a tool for providing the necessary data for a quantitative analysis of the inner and outer barriers, namely determination of the parameters characterizing a double-humped fission barrier.

The gamma back-decay mode is expected to dominate in the low Z region of the actinides. This is due to the fact that for the nuclei of this region, the inner barrier is narrower and lower in height than the outer one. However, the back-decay transition has not been observed in most of these nuclei. This can probably be attributed to some extent to the experimental difficulties involved in the detection of gamma rays from such short-lived, weakly-populated isomeric states. The back-decay gamma ray has been searched for by exciting the shape isomeric states in $^{236}$U, $^{238}$U, and $^{238}$Np. For $^{238}$Np shape isomer, no back-decay gamma ray was observed (Borggreen *et al.* 1974), and in $^{236}$U contradictory results exist (Habs *et al.* 1975; Bartsch *et al.* 1978; Butler *et al.* 1980).

Direct reactions have generally been used in populating the shape isomeric states. It was also proposed to use the muon as a probe to excite the shape isomeric state in heavy deformed nuclei (Blocki *et al.* 1972). The role of the muon in this kind of experiment is characterized by its so-called "radiationless" transitions, the process in which the muonic atom undergoes a transition by exciting the nucleus rather than the normal X-ray or Auger electron emission. The isomer produced would then have a negative muon orbiting in its 1S state. The effect of the binding energy of the muon is to increase the height of the outer barrier relative to the inner one, and therefore to facilitate the gamma back-decay mode of deexcitation of the shape isomer. The gamma branch of the shape isomeric deexcitation in muonic $^{238}$U has been investigated by a CERN group (Fromm *et al.* 1977). They have reported observation of several gamma rays, two of which can feed to the transition from the energetically shifted isomeric level to the vibrational and rotational levels of the nucleus in the first well. Based on their results, they have estimated that in the muonic $^{238}$U nucleus, the chance of shape isomer excitation in the muon radiationless transition is about $10^3$ times that of a bare nucleus excited by a direct reaction.

The present work was also aimed at bringing about some conclusive results on the gamma back-decay of the shape isomeric states in the muonic $^{238}U$, $^{236}U$,and $^{235}U$ atoms.

# CHAPTER 2

# THEORY

## 2.1. Introduction

Appearance of a second well in the fission barrier of the actinides as a result of Strutinsky's calculation provides the heretofore missing grounds for understanding of the puzzling situation connected with the anomalously short lived fission isomers. The first fission isomer reported by Polikanov *et*al. (1962) was discovered in $^{242}$Am and exhibited a 14 ns delayed fission activity. The excitation energy $E_{II} = 2.9 \pm .4$ Mev of the isomer was determined from the threshold behavior of the excitation function for the production of the $^{242}$Am fission isomer through the $^{243}$Am (n,2n) reaction (see fig. 2-1). At that time it was not understood how an excited state with 2.9 Mev excitation energy could resist gamma decay for more than 14 ns and manage to undergo fission at a rate much faster than expected from ground state barrier penetration. Soon it was found that the yield of the isomer, compared to the ground state yield, remained unchanged whether it was produced in a (p,n) reaction at the coulomb barrier with no appreciable angular momentum transfer or through a heavy ion reaction introducing 20 to 50 units of angular momentum into the system, thereby, ruling out the possibility of explaining the stability toward gamma decay by ascribing a very high spin value to the isomeric level (Flerov and Polikanov, 1964). Although the idea of "nuclear shape isomerism" implying that the isomer was trapped in an intermediate energy minimum was one of the several possible explanations by Polikanov *et*al. (1962), the manifestation found its strong theoretical support in 1966, when Myers and Swiatecki (1966) incorporated the shell effects into the LDM and especially, when the numerical results obtained by Strutinsky using his macroscopic-microscopic method showed that for a certain region of nuclei among the actinides the liquid drop fission barrier was split into two by a large negative shell correction, and $^{242}$Am lay in that region. More detailed

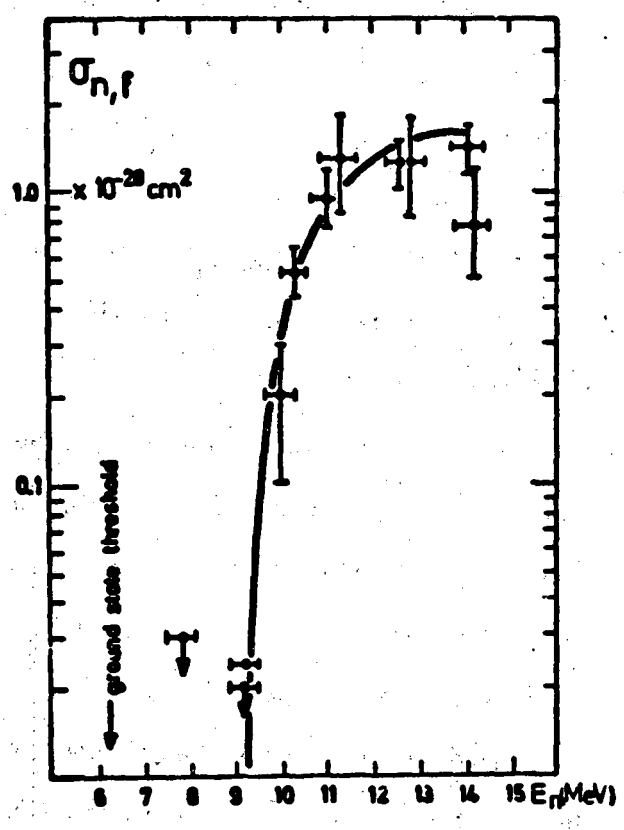


Fig. 2-1 Excitation function for production of the $^{242}$Am fission isomer through the $^{243}$Am(n,2n) reaction (A. Michauden, 1978).

discussion of the shape isomers is given in section 2.2 of this chapter.

The understanding of the phenomena of "shape isomerism" was not the only application for the new idea of double humped fission barrier. In fact, this concept became the center of importance in understanding a vast amount of data on nuclear fission and its development was a great step forward, not only in fission, but in nuclear physics in general. Among others it provided explanations for some previously puzzling features of induced fission, such as, resonant-like structure in sub-barrier fission excitation function and intermediate structure observed in low energy neutron-induced resonance studies. The theory of the double-humped fission barrier, an analysis of its applications in explaining different experimental results and various penetrability calculations are presented in sections 2.3 and 2.4.

It is noticeable that spontaneously fissioning isomers are found predominately among the isotopes of Pu and Am, and are rare for the low Z actinides. Although fission isomers have been identified in $^{236}$U (Lark *et*al. 1969 ;Wolf *et*al. 1970) and in $^{238}$U (Wolf *et*al. 1970; Polikanov *et*al. 1970), their formation cross section is approximately one order of magnitude lower than the values obtained for even-even plutonium shape isomers (Wolf *et*al. 1970). Searches for delayed fission in other isotopes of uranium have produced negative results (Lark *et*al. 1969; Wolf *et*al. 1970; and Britt *et*al. 1971); and the $^{237m}$Np is the only spontaneously fissioning isomer found among neptunium isotopes. The rareness and the low-yield of delayed fission in the low Z end of the actinide region can most probably be explained by the effective competition of the gamma back-decay mode in deexcitation of the shape isomeric state in nuclei in this region. This explanation is supported by a number of indications suggesting the decrease in height of the inner barrier relative to the outer one , as the atomic number decreases. The more penetrable inner barrier, despite the intrinsic hindrance of gamma decay compared to fission, makes it more feasible for the isomer to deexcite through gamma back-decay to the normal ground state than undergo delayed isomeric fission. The preference of the back-decay mode is enhanced if the negative muon is used to probe the excitation of the shape isomeric state. In fact, the

coulomb interaction of the muon in its 1S state with the nucleus results in a favorable perturbation of the double-humped barrier. The muon probe and some theoretical discussion of the non-radiative transition will be presented in sections 2.6.1 to 2.6.3. The gamma back-decay of the shape isomeric state to the normal ground state and the application of its measurement in parameterization of the fission barrier are discussed in section 2.5 of this chapter.

## 2.2. Shape Isomers

Realizing that fission isomers are in effect shape isomers, and that their excitation energy is nothing more than deformation energy, how can one experimentally learn about the size of the quadrupole deformation of these species? In principle, there are two ways of obtaining information about the size of the quadrupole deformation associated with the second well. One way is by determining the intrinsic quadrupole moment of the isomer, and the other -a rather indirect way- is by identifying the lowest rotational band built on the isomeric ground state. An experiment was carried out on the 4 ns $^{240}$Pu fission isomer using the latter method (Specht *et*al. 1972). It was the first experiment that confirmed the interpretation of the existence of fission isomers, in terms of double humped fission barrier shapes. The transition between low-lying rotational levels in even-even nuclei are highly converted, yielding low energy electrons. In spite of the difficulties associated with observation of these low-yield electrons in the presence of many other sources of low energy electrons in the experiments, Specht *et*al. identified the rotational band built on the shape isomeric state by detection of the conversion electrons preceding the isomeric fission using delayed coincidence between the electrons and the fission fragments. A fit of the transition energies to the well known expansion of the rotational energies in powers of the quantity $J(J+1)$ is shown in fig. 2-2. The value found for the rotational constant $\bar{h}^2/2I$ is 3.33 kev. This value is less than half of the value exhibited for the ground state band of 7.16 kev, providing fairly direct evidence that the fission isomers are indeed shape isomers in the second well, as predicted by Strutinsky's calculation, and have a distortion qualitatively different from that of the ground state.

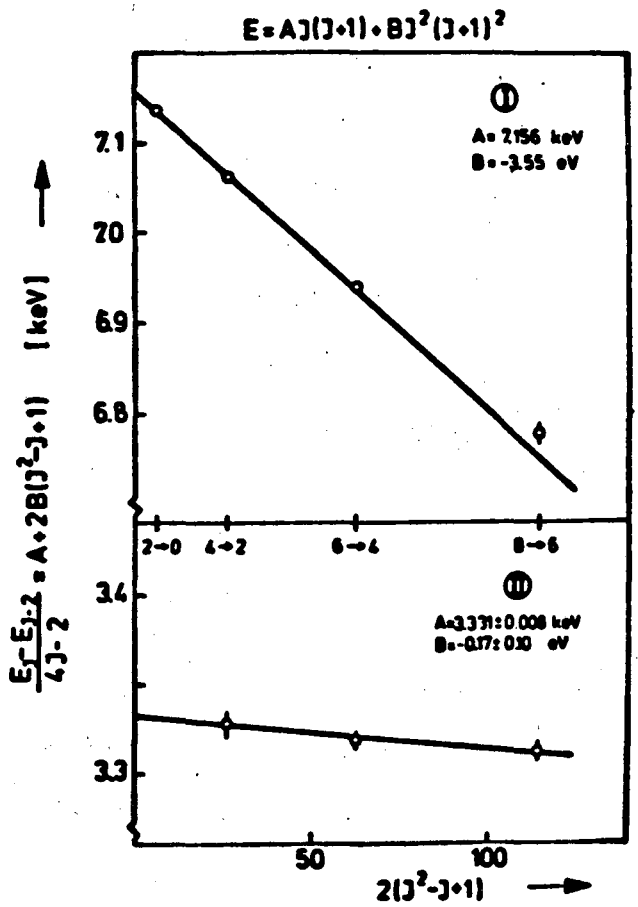


Fig. 2-2 A fit of observed rotational energies of $^{240}Pu$ to the rotational expresion given on the top, (I) for 4 ns fission isomer and (II) for the normal ground state (H. J. Specht, 1974).

The relation between the static quadrupole moment and the shape is less model-dependent than is the relation between the moment of inertia and shape. In case of E2 transitions it is possible to deduce the quadrupole moment from the observed lifetimes. Since the measurement of such subnanosecond half lives was not feasible with direct electronic timing, the Heidelberg group (Halis *et*al. 1977) developed an ingenious "charge plunger" technique. The technique has been applied to a study of the rotational band feeding the 8-$\mu$second isomer of $^{239}$Pu produced in an ($\alpha$,3n) reaction. The decay curve fits into the theoretical curve representing cascade calculations for different values of the rotational band and gives a quadrupole moment of 36 barns.

In another attempt Metag and Slitten (1977), using a rather different approach, deduced a value of 37 barns for a 37-ps isomer of $^{236}$Pu. These values of quadrupole moment, for a prolate spheroid shape correspond to a value c/a $\approx$ 2 for the axis ratio, assuming a radius parameter of $r_o$ = 1.2 fm (Habs *et*al. 1977).

Presently more than 35 fission isomers have been identified in U through Cf with half lives ranging from a few ps to 14 ms. These half lives are shorter by 20-30 orders of magnitude than the fission half-lives of the ground state, because of increased tunneling probability. The occurrence and half lives of these isomers are illustrated in fig. 2-3. The boundaries of this island of shape isomers is consistent with those predicted (Brack et al., 1972; Moller and Nix 1973; Johansson *et*al. 1970; Nix, 1972; Pali, 1973) by "switch-over" in the relative heights of two barriers. For Z >97 the half lives become too short to be observable with current techniques. For Z <92 shape isomeric gamma decay rather than fission presumably becomes dominant. For a number of nuclei occurring in fig. 2-3 two decay periods are given. The one at the top is presumably due to an excited state in the second minimum. Also the common mode of decay for the isomers is seen to be spontaneous fission. In a few cases, namely $^{236}$U, $^{238}$U, and $^{237}$Np the gamma branch to the ground state dominates and the decay probability should be corrected for the gamma decay mode. While the isomeric half lives show strong neutron depen-

dence and a strong odd-even effect (Fig. 2-4), their proton dependence, in contrast, shows a monotonic change as seen in fig. 2-5. The straight line behavior of half lives as a function of proton number for a given neutron number (fig. 2-5) is in qualitative agreement with the decrease in the liquid drop part of the height of the outer barrier with increasing $Z^2/A$. The neutron dependence of the isomeric half lives is completely different from the nearly horizontal lines produced by the liquid drop model. These are consistent with the theoretical calculations that indicate the spontaneous fission isomerism results primarily from a neutron shell effect and not a proton-shell effect (R. Vandenbosch 1977).

The general trend of half lives versus neutron number suggested the existence of a neutron shell around $N \approx 146$ for deformation near that of the second well. Another important feature revealed in fig. 2-4 is the large retardation of the half lives for odd-A and odd-odd nuclei compared to even-even nuclei. The odd-even effect is commonly interpreted as resulting from three different contributions (S. Bjornholm *et*al. 1980):

- An increase in "inertial parameter" and hence a decrease in $\bar{h}\omega_B$ (curvature of the second barrier) with number of unpaired nucleons.

- An increase in the "pairing gap" at the barrier top compared to the gap at the shape isomeric ground state.

- The presence of the unpaired particles may increase the height of the barrier that must be penetrated by an amount sometimes designated as the "specialization" energy and hence decreases the penetration probability

Some specific information on the barrier of the nucleus in the shape isomeric state, in particular on the isomer excitation energy and height of the second barrier can be obtained from study of the experimental data on cross sections for isomer production.

Most of the measurements have used neutron evaporation reactions in which two or more neutrons are emitted prior to reaching the nucleus of interest. The excitation functions, therefore, show an appreciable slope near threshold. Thus, an extrapolation from the lowest energy at

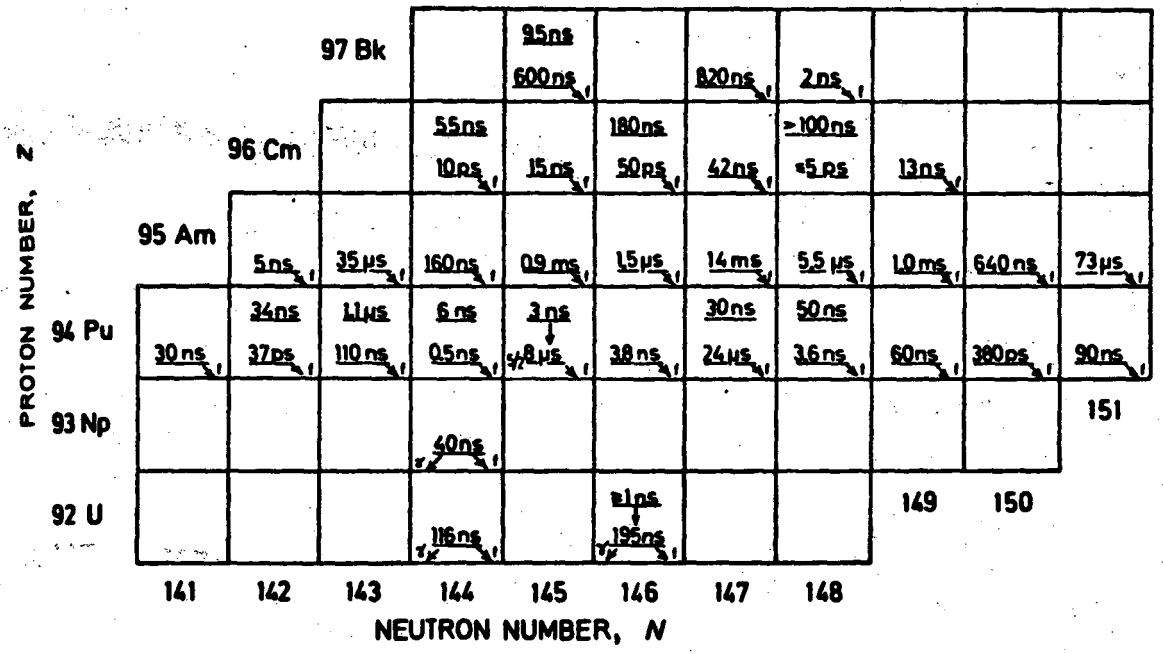


Fig. 2-3 Location of the shape isomers in the actinide region of the isotope chart and their halflives (S. Bjornholm, 1980).

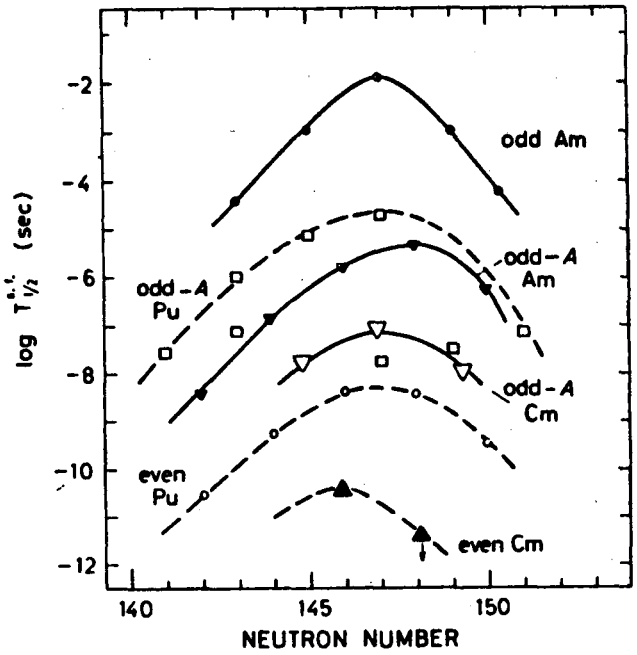


Fig. 2-4 Shape isomeric halflives as a function of neutron number show strong neutron dependance and odd-even effect (S. Bjornholm, 1980).

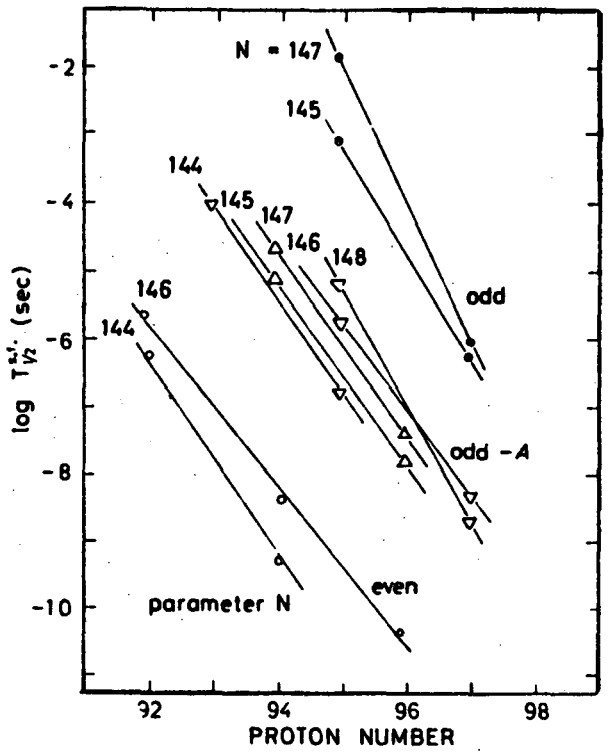


Fig. 2-5 Halflives for spontaneous fission as a function of proton number (S. Bjornholm, 1980).

which measurements are made to the threshold energy is required. This extrapolation is performed with the help of a statistical model. Values between 1.6 and 2.6 Mev have been obtained for a number of Pu, Am and Cm isotopes (Britt *et*al. 1973). In addition, in the case of neutron evaporation reactions, information on the relative transmission coefficients of the inner and outer barriers can be deduced from the maximum value of the excitation curve and the drop in the yield with further increasing excitation energies should be governed by the outer barrier of the final nucleus (S.Bjornholm, 1980).

### 2.3. Theory and Applications of the Double Humped Barrier

Several review articles on the barrier aspects of fission have appeared during the last decade ( for example, Strutinsky and Pauli, 1969; Lynn, 1969; Brack *et al.* , 1972; Nix ,1972; Michaudon, 1973,1976,1978; Grant, 1976 ). The latest and most complete review (Bjornholm and Lynn, 1980) gives a critical and comprehensive account of the information about the double humped fission barrier that can be deduced from experimental work.

The original idea of the fission barrier is based on the classical theory of the electrically charged liquid drop , and dates back to the work of Bohr and Wheeler (1939). The so-called "Liquid Drop Model (LDM)" which accounts only for the smooth trend of the fission barrier potential shape, uses an analogy between nuclear behaviour and that of a charged liquid drop to define the terms of a semiempirical formula for the nuclear ground state . If the nuclear "fluid" is assumed to be incompressible,the volume energy remains constant with variation in the deformation of the nucleus. Therefore, only the coulomb and the surface energy terms contribute to the formation of LDM potential barrier. It was shown by Bohr and Wheeler that a spherical liquid drop nucleus is unstable if

$$\frac{E_{coul}}{2\,E_{surf}} = \frac{c_3}{2\,c_2}\cdot\frac{Z^2}{A} > 1 \qquad (2\text{-}1)$$

where $c_3$ and $c_2$ are coefficients of coulomb and surface energy terms in the standard semiempirical formula, respectively. The above ratio is called the fissility parameter and denoted by X. Values of X appropriate to actinide nuclei are $\approx$ .7 to .8 and most studies of deformation energy contours are concentrated on drops with these fissility parameter values. These energy contours are commonly defined by two of the most important deformation parameters, namely the quadrupole and hexadecapole coefficients in a Legendre polynomial expansion of the coordinates of the liquid surface . The LDM barrier is in fact the energetically most favorable path towards fission in these energy contours (Bjornholm and Lynn, 1980). The LDM fission barrier is shown in fig. 2-6 (broken lines). The maximum of the LDM barrier corresponds to the saddle point in the associated energy contour. At small deformations the surface energy dominates and its growth with deformation counters the effect of the decreasing coulomb barrier. At the saddle point these two energies compensate for each other, and afterwards the coulomb energy starts to have the dominating role. The LDM gives a reasonable phenomenological description of the average properties of the fission process and nuclear masses. As pointed out by Strutinsky and Pauli (1969), there are some intrinsic structure effects in nuclear fission that cannot be explained by this model. For example it was observed that the measured heights of the fission barriers in heavy nuclei do not decrease as fast as the LDM predicts. In fact, they remained rather constant, equal to 5-7 Mev. Also the model overestimated the mass of the magic nuclei such as $^{208}$Pb by 10-15 Mev.

Myers and Swiatecki (1966) attempted to incorporate shell effects into the semiempirical formula in terms of shape factors introduced as coefficients of surface and coulomb energies and also added a shell term which depended on N and Z and had a Gaussian fall off with deformation . Later Strutinsky (1966,1967) developed a macroscopic-microscopic model in which the LDM was used as a macroscopic model to represent the smooth trend of the potential barrier with respect to particle number and deformation and the local fluctuations due to the quantization of single particle motion are taken from a microscopic (single-particle) model.

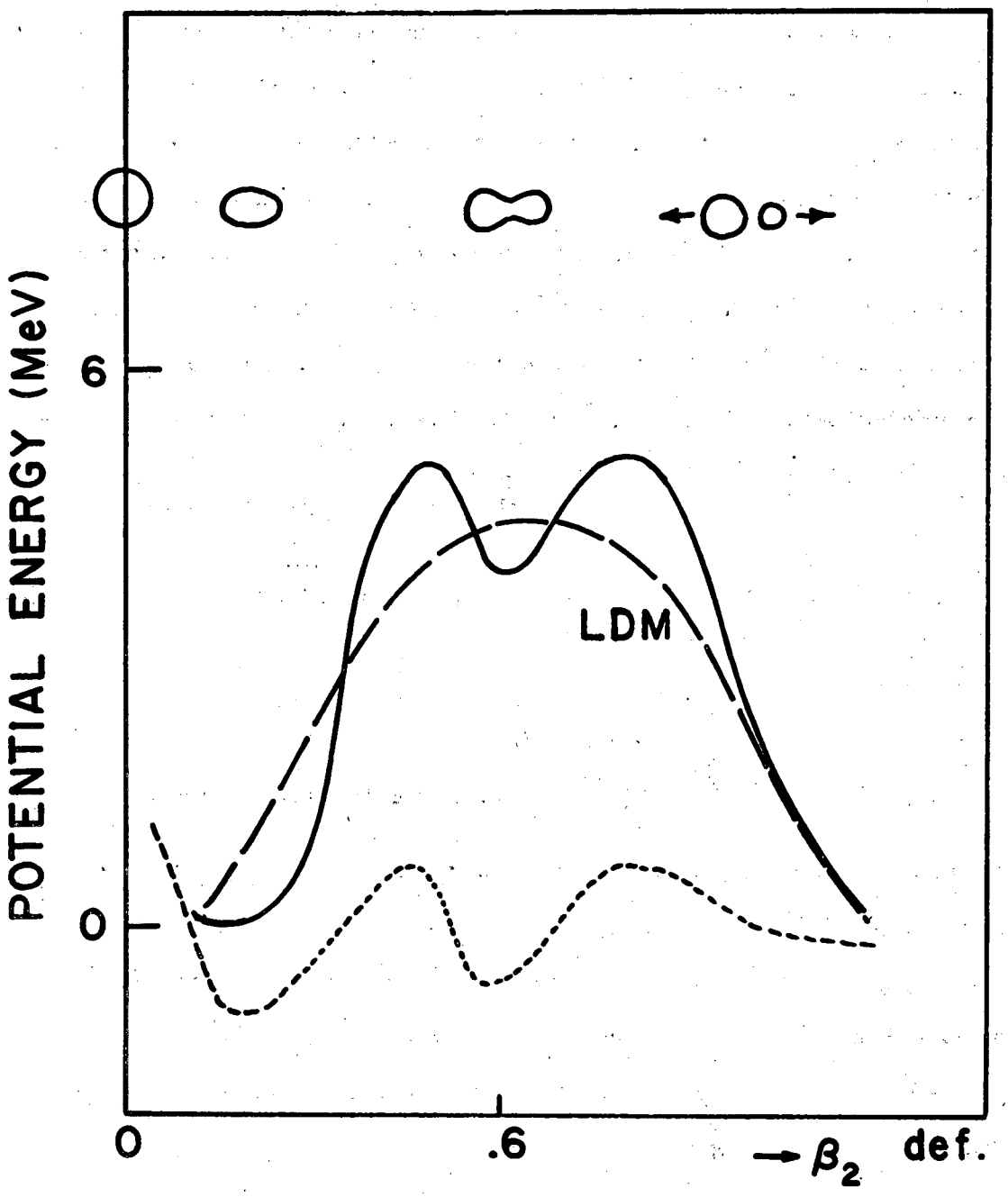


Fig. 2-6 Double-humped fission barrier resulted from superimposing shell-effects (dotted-line) on LDM barrier (broken line).

The technical procedure for carrying out the Strutinsky's model calculation and the physical nature of the results are reviewed by Brack *et al.* (1972) and by Nix (1972). Also in the review of double humped barrier written by Bjornholm (1980) there is a good critical discussion of Strutinsky's method. In his approach, Strutinsky calculates the shell correction, essentially by summing the energies of occupied single particle Nilsson orbitals in a deformed potential well of a given deformation and subtracting from this the smoothed energy. The smoothed energy is calculated by integrating the single-particle energies over a suitably averaged single-particle level density. The shell energy correction is illustrated by A.Michaudon (1976) to have the following form:

$$E_m(\{s\}) = 2 \int_{-\infty}^{\lambda_0} E\, g(E,\{s\})dE - 2 \int_{-\infty}^{\lambda} E\, \bar{g}(E,\{s\})dE \qquad (2\text{-}2)$$

where :

- $\{s\}$ is any a set of deformation parameters.

- $g(E,\{s\}) = \sum_i \delta[(E - E_i(\{s\})]$ is the shell model level density corresponding to a discrete set of levels $i$ having energy $E_i(\{s\})$ at deformation $\{s\}$, energy levels $E_i(\{s\})$ can be calculated from a potential well of almost any shape defined by the set $\{s\}$ of deformation parameters.

- $\bar{g}(E,\{s\})$ is a smooth level density obtained by folding $g(E,\{s\})$ into a smoothing function having a width of 8 to 10 Mev. corresponding to the distance between shells.

- $\lambda_0$ and $\lambda$ are the Fermi energies for the level densities g and $\bar{g}$ respectively and are determined so as to conserve the number of particles.

The subtracted gross energy in 2-2 is then replaced by a realistic energy term $E_{LDM}$ calculated from the LDM (see fig.2-6). Therefore for all deformations along the fission path from the ground state to scission, the total potential energy $E(\{s\})$ of the fissioning nucleus can be expressed as the summation of two terms by

$$E(\{s\}) = E_{LDM}(\{s\}) + E_m(\{s\}) \qquad (2\text{-}3)$$

It should be mentioned however that $E_{LDM}$ is not an accurate substitution for the macroscopic energy. Improvement of the LDM energy can be obtained by using the Droplet Model (Myers *et al.* 1969; 1970; 1974), in which, terms of higher order in $A^{-1/3}$ and $I^2=(\frac{N-Z}{A})^2$ are taken into account in contrast to the LDM, where they are eliminated by truncation in the expansion (Myers and Swiatecki, 1969). Nevertheless, this model also fails to reproduce accurately the macroscopic energy in cases of shapes with too narrow necks or too abrupt irregularities (A.Michaudon, 1976). These shortcomings have been taken care of by a simple method that takes into account finite-range-effects, by calculating the macroscopic energy in terms of a double volume integral over a Yukawa function (Krapper and Nix, 1974).

The Strutinsky method was successful in reproducing the observations that the LDM failed to explain , such as, energies of magic nuclei and the measured heights of fission barriers. One major consequence of this calculation was the demonstration of the oscillatory behavior of the shell correction with deformation, which expresses the fact that the "shell" effect could exist in deformed as well as spherical potential wells. In fact, superposition of this oscillatory shell correction on the smooth LDM energy introduced the double humped feature into the fission barrier of the heavy nuclei (fig. 2-6). The technique for calculating fission barrier potential pointed out here is discussed in more depth and detail in a review by P.Moller and J.R.Nix (1974).

Many shell model potentials have been developed to calculate the shell energy correction. The general pattern of the barrier shape is obtained in all calculations. It is found,for example, that the shell energy correction moves from the small deformation side to the larger deformation side of the LDM saddle point for increasing mass number. Consequently the inner barrier is lower in height than the outer one for light actinides , whereas the opposite is true for heavy actinides. Nevertheless, some differences exist in numerical values. Recently the use of some more sophisticated parameterization of the shape of the nucleus has revealed some details of the

barrier shape. It is shown that axial asymmetry lowers the inner barrier( Larson *et al.* 1972), whereas mass asymmetry lowers the outer barrier (Moller and Nilsson, 1970)[see fig. 2-7]. The latter effect provides a simple explanation for the well-known mass asymmetry in the low energy fission of actinide nuclei (Hans J.Specht, 1974).

Perhaps, the most significant experimental result that can only be explained by the concept of the double humped fission barrier is the shape isomerism. However, there are two other important experimental results explained by this concept. These are vibrational resonances in fission cross sections and the so-called intermediate structure. These two structures are observed in experiments in which the target nuclei have even numbers of neutrons (like $^{230}$Th and $^{240}$Pu), so that the compound nuclear state populated by low energy neutron capture has an energy lower than the fission -barrier height.

Vibrational resonances are observed with neutrons of a few hundred kev, being captured by $^{230}$Th and leading to subbarrier fission (fig.2-8). In this figure experimental resolution is a few tens of kev. The LDM tells us that that fission cross section should increase steeply with increasing excitation, therefore that model can not explain these resonances. It is known that the second potential well, at a deformation of almost twice that of the ground state, is typically about 3 Mev above the normal ground state energy. The vibrational levels of the second well have width smaller than the spacing between class -II (referring to the second well) compound nuclear states and at energies of the magnitude of these lowest class-II vibration, the vibrational levels of the first well are completely damped into the nearly continuous class-I (referring to first well) compound nuclear states. So that if the excitation energy of the compound nucleus E is not much above the second well energy (in the case of a shallow second well, like in $^{230}$Th) the situation can resemble the quantum mechanical problem of penetration of a free particle through a double-humped barrier. The penetration probability of a double-humped barrier calculated in a WKB approximation shows strong resonances at energies equal to those of the bound states of the second well. This structure in the subbarrier penetration then translates into

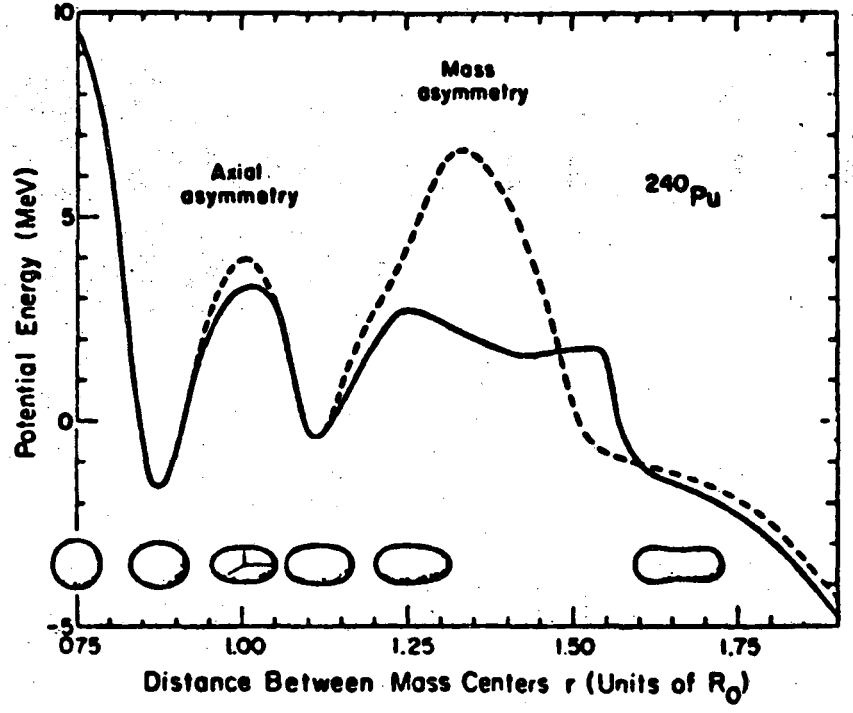


Fig. 2-7 Effect of axial and mass asymmetry on the double-humped barrier of $^{240}Pu$

(A. Michaudon, 1976)

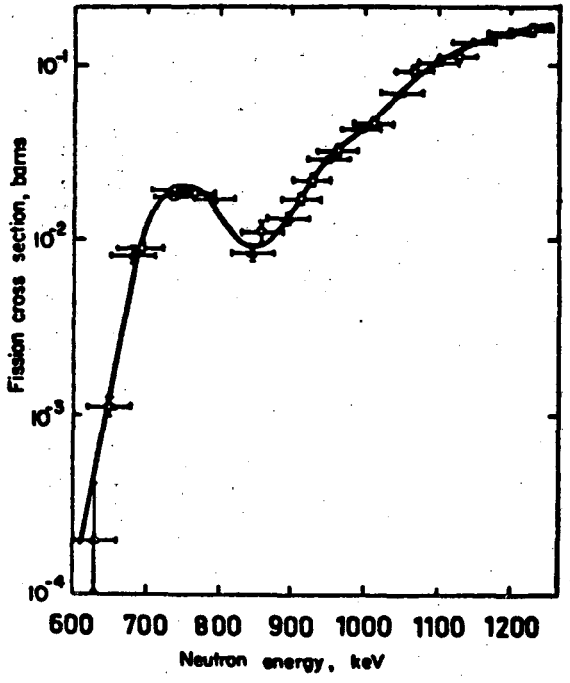


Fig. 2-8 Cross section for neutron induced fission in $^{230}Th$ (M. A. Preston, 1975).

fission cross section ($\sigma_{nf} = \sigma_n.P_f$) , such as the resonances at neutron excitation energy of 715 kev in the fission cross section of $^{230}Th$ (fig. 2-8)and in (d,pf) reactions in the compound nuclei $^{234}U$, $^{236}U$, $^{240}U$, and $^{242}Pu$ (Back *et al.* 1974).

An example of intermediate structure in fission cross section is the grouping of resonances observed in high resolution experiments with neutrons having energies of a few hundred ev or a few kev incident on $^{240}Pu$ (see fig. 2-9). In this figure the fine spacing is in fact the space between class-I compound nuclear states, and the intermediate spacing is due to class-II compound nuclear level spacing. One has to consider that at these low excitation energies both the class-I and class-II compound nuclear levels are discrete, but the vibrational levels have widths greater than the spacing between compound nuclear levels. The narrow resonances are at incident energies that coincide with class-I compound nuclear levels, where the resonances in cross section for compound nuclear formation $\sigma_n$ translates into enhancement of fission cross section at these energies ($\sigma_{nf} = \sigma_n.P_f$). Since for a given excitation energy the class-II compound nuclear levels are much less compact (level spacing of a few hundred ev), a group of class-I states (level spacing of the order of 10 to 15 ev) having energies in the neighborhood of one of these levels can get a strong enhancement by coupling between class-I and class-II compound nuclear states through the intermediate barrier (Andre Michaudon, 1976). This coupling is then responsible for the bunched structure seen in fig. 2-9.

### 2.4. Barrier Penetrability

Most of the important aspects of fission cross sections associated with the double-humped fission barrier are somehow connected to the quantum mechanical tunneling through the barrier. For example, the vibrational resonances in neutron induced fission cross section of low Z actinides was shown to originate from resonant energy dependence of the penetrability of a double-humped fission barrier. Also a large number of experimental data on direct reaction induced fission cross sections are analyzed, using the penetrability of the double-humped barrier. The penetration probability is normally calculated by solving the Schrodinger equation in

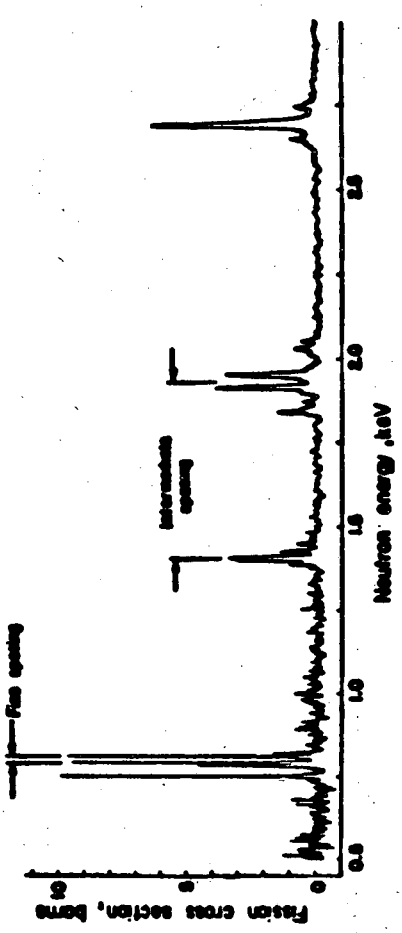


Fig. 2-9 The subthreshold fission cross section of $^{240}Pu$ (M. A. Preston, 1975).

one dimension with appropriate boundary conditions and only a travelling wave function on the right of the barrier.

The penetrability of a parabolic barrier is given by the expression derived by Hill and Wheeler (1953)

$$P = \frac{1}{1 + \exp(2\pi\, \Delta E/\, \bar{h}\omega)} \tag{2-4}$$

where $\Delta E$ is the barrier height measured from the point of penetration and $\bar{h}\omega$ is the barrier curvature energy. For $\Delta E \geq \bar{h}\omega$, this becomes

$$P = \exp[-2\pi\, \Delta E/\, \bar{h}\omega] \tag{2-5}$$

Assuming parabolic inner and outer barriers, the penetrabilities $P_A$ and $P_B$ respectively are expressed as

$$P_A = \exp[\, -2\pi\, (E_A - E_i)/\, \bar{h}\omega_A\, ] \tag{2-6}$$

$$P_B = \exp[\, -2\pi\, (E_B - E_i)/\, \bar{h}\omega_B\, ] \tag{2-7}$$

where $E_A$ and $E_B$ are the height of the first and the second barrier and $E_i$ is the excitation energy of the shape isomeric state.

Several different penetrability calculations have been presented for the double-humped barriers. Pedersen *et al.* (1969) have used a nummerical integration method in a statistical model to describe the structure observed in fission probabilities obtained in (d,pf) experiments. Using the WKB approximation to calculate the quasi-classical penetration probability of the separate barriers ($P_A$ and $P_B$), Ignatyuk *et al.* showed that the approximate penetration probability of a double-humped barrier can be expressed by

$$P(E) = \frac{1}{4}\, P_A P_B[\, \frac{(P_A + P_B)^2}{16}\, \sin^2\phi + \cos^2\phi\, ]^{-1} \tag{2-8}$$

where $\phi$ is the phase associated with the second well at energies $E_n$ of the bound states of the second well

$$\phi(E_n) = (n + 1/2)\pi \tag{2-9}$$

So that at incident energies E coinciding with one of the bound states ($E_n$'s), the penetrability is maximum ($\cos\phi = 0$) [see fig. 2-10]. The ratio of $P_{max}/P_{min}$ is equal to $\frac{16}{(P_A + P_B)^2}$, which is always much larger than unity, thus explaining the structure in subbarrier penetration. The most important feature of the penetrability through a double-humped barrier, namely the resonance in the transmission function, as opposed to the monotonically rising transmission function of a singled peaked barrier is common in penetrabilities resulting from all of the calculations.

A double-humped barrier can be constructed by smoothly connecting parabolas to define two peaks with an intermediate well. In this case an exact numerical solution can be obtained for the penetrability. Such a barrier has been considered particularly by Cramer and Nix (1970) and Wong and Bang (1969). In their notation the expression for different portions of the potential are as follows

$$\begin{aligned} V(\epsilon) &= E_1 - 1/2\ \mu\omega_1^2(\epsilon - \epsilon_1)^2 \quad , \quad \epsilon < a \\ V(\epsilon) &= E_2 - 1/2\ \mu\omega_2^2(\epsilon - \epsilon_2)^2 \quad , \quad a \leq \epsilon \leq b \\ V(\epsilon) &= E_3 - 1/2\ \mu\omega_3^2(\epsilon - \epsilon_3)^2 \quad , \quad \epsilon > b \end{aligned} \tag{2-8}$$

where $\epsilon$ denotes the nuclear deformation coordinate in the fission degree of freedom, a and b are connecting points of the three parabolas. The energies $E_1$ and $E_3$ are the maximum values of the potential at deformations $\epsilon_1$ and $\epsilon_3$ respectively, and $E_2$ is the minimum value at deformation $\epsilon_2$. The effective mass of the system with respect to distortion in the $\epsilon$ direction is represented by $\mu$. The curvature of the parabolas are $\mu\omega_1^2$, and $\mu\omega_3^2$. There are nine parameters involved in the above definition of the barrier, of which three can be eliminated, two by the requirement of the

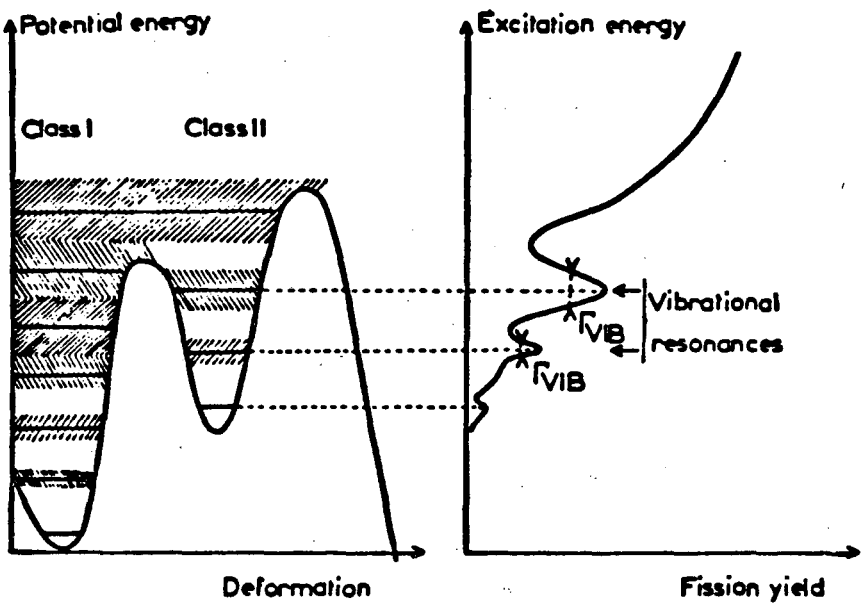


Fig. 2-10 Fission mechanism for the case of double-humped barrier. On the left the class-I and class-II vibrational levels are shown with horizental solid lines and their dampings into the compound nuclear levels are indicated by hatched areas. On the right the vibrational resonances in fission excitation function correspond to the class-II vibrational resonances (A. Michaudon, 1976).

segments joining smoothly at the intersections a and b, and the third one is eliminated by the translational invariance of the potential. Therefore, the barrier will be characterized by three energies ($E_1$, $E_2$ and $E_3$) and three frequencies ($\omega_1$, $\omega_2$ and $\omega_3$) and the remaining parameters can be expressed in terms of these six barrier parameters as follows

$$\epsilon_1 = (2E_1/mu\omega_1^2)^{1/2}$$

$$a = \epsilon_1 + [\, 2(E_1 - E_2)/\mu\omega_1^2 \,]^{1/2}(1 + \omega_1^2/\omega_2^2)^{-1/2}$$

$$\epsilon_2 = a + [\, 2(E_1 - E_2)/\mu\omega_2^2 \,]^{1/2}(1 + \omega_2^2/\omega_1^2)^{-1/2} \qquad (2\text{-}9)$$

$$b = \epsilon_2 + [\, 2(E_3 - E_2)/\mu\omega_2^2 \,]^{1/2}(1 + \omega_2^2/\omega_3^2)^{-1/2}$$

$$\epsilon_3 = b + [\, 2(E_3 - E_2)/\mu\omega_3^2 \,]^{1/2}(1 + \omega_3^2/\omega_2^2)^{-1/2}$$

The Schrodinger equation for these potentials are written as

$$\frac{d^2}{dt^2}\psi_i + \frac{2\mu}{\hbar^2}[\, E - E_i \pm \frac{1}{2}\mu\omega_i^2(\epsilon - \epsilon_i)^2]\psi_i = 0, \quad i=1,2,3 \qquad (2\text{-}10)$$

where the plus sign refers to the regions of first and second peaks, and minus sign is used when i refers to the second well region. Cramer and Nix showed that with appropriate change of variables, the Schrodinger equations (2-10) can be reduced to a general class of second order differential equations with Weber's parabolic-cylinder functions as their solutions. Then the penetrability is determined by the incident and transmitted amplitudes A and T respectively, and is given by

$$P = (\omega_3/\omega_1)^{1/2} \mid T/A \mid^2 \qquad (2\text{-}11)$$

The conservation of probability current is said to be implying the appearance of the curvature parameters $\omega_1$ and $\omega_3$ in the formula. An example of a computed penetrability by this method is shown in fig. 2-11. The shape of the barrier is shown with the connecting points a and b, and

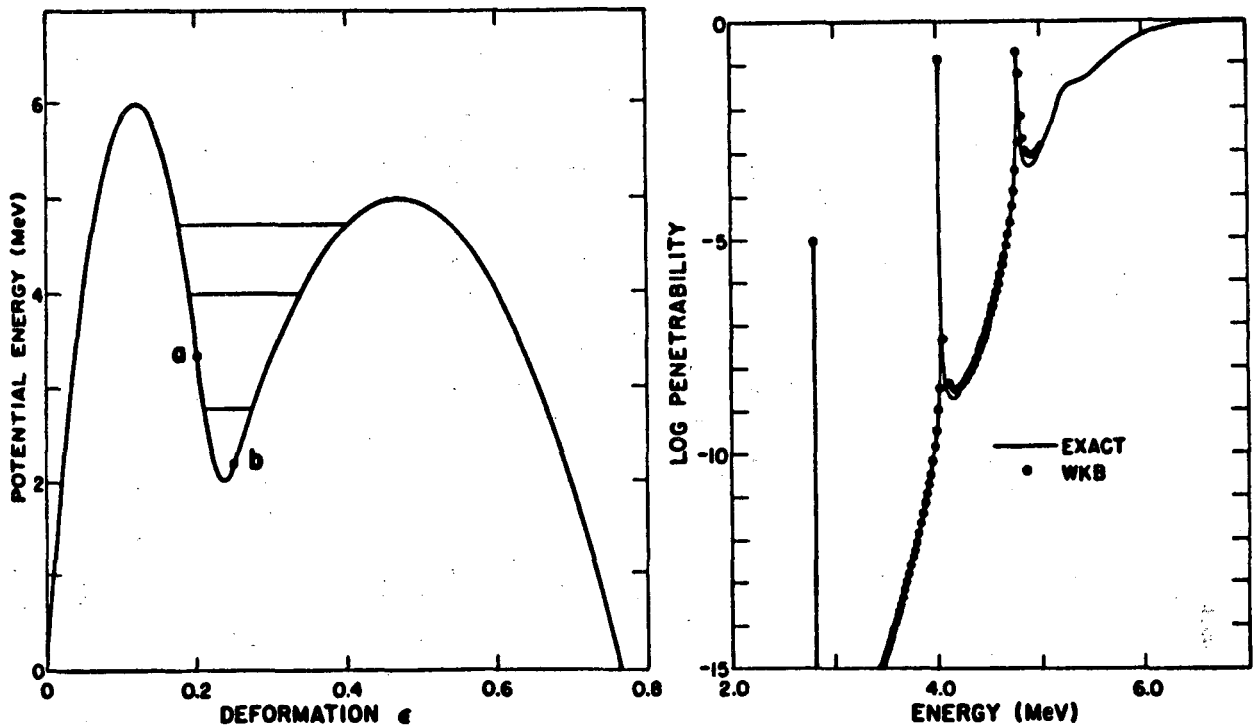


Fig. 2-11 Comparison of exact and WKB penetrabilities for an asymmetric barrier. On the left the barrier model is shown with the position of the bound levels. On the right the exact results (solid lines) and the WKB results (solid points) are compared (Cramer and Nix, 1970).

the position of virtual vibrational energy levels in the second well. A comparison is also made with the penetrability calculated with the WKB approximation formula of Ignatyuk *et al.* (1969). The WKB approximation of the penetrability is only valid over a limitd incident energy, between the bottom of the second well and the top of the lowest peak. The exact result differs by 20 kev from the WKB calculation at the 4.76 Mev energy level. The comparison indicates that the two methods are in good agreement for incident energies within WKB limitation.

### 2.5. Gamma Back Decay

Decay of the shape isomeric state of a bare nucleus (non-muonic) may take place by tunneling through the inner and outer barriers of the double humped fission barrier. The outer barrier penetration results in delayed isomeric fission. Whereas, the tunneling through the inner barrier is followed by gamma back-decay to the levels in the first well of the potential barrier. Calculations of double humped fission barrier (Tsang *et al.* ,1970; Moller *et al.* ,1973) indicate that the outer barrier is the higher of the two for the low Z actinides. This systematic trend is in part the consequence of the shift of the liquid-drop fission barrier toward a higher deformations as Z decreases. A parameterization of the double humped fission barrier based on the fit to the experimental results (Back *et al.* ,1973) also show that for the doubly-even actinides, the height of the inner barrier is systematically lower for lower-Z nuclei, and the reverse is true for the higher-Z actinides. The fitted parameters also include $\bar{h}\omega_A$ and $\bar{h}\omega_B$, the inner and the outer barrier curvature energies, respectively. A larger curvature energy corresponds to a narrower barrier. The inner barrier curvatures are consistently larger than the outer barrier curvatures. This trend has appeared in the theoretical calculation of Tsang *et al.* (1970). In spite of this systematic trend of barrier heights and curvatures which probably predicts a rather more penetrable inner barrier for lower Z actinides, gamma back-decay transitions have not been observed in most of the nuclei in this region. This can be attributed to some extent to the experimental difficulties in detection of gamma rays from such short lived and weakly populated shape

isomers. Search experiments have been performed using different reactions to observe gamma back-decay transitions from shape isomeric states in $^{236}U$, $^{238}U$, and $^{238}NP$. No such gamma transitions were observed from $^{238m}Np$ in the attempt made by Borggreen *et al.* (1974) using the $^{238}U(d,p)$ $^{238m}Np$ reaction. For $^{236m}U$ case there have been several attempts. Using the $^{235}U(d,p)$ $^{236m}U$ reaction at $E_d$=10Mev., Habs *et al.* (1975) have tentatively suggested the existence of a gamma transition ($E_\gamma$=2215kev) deexciting the shape isomeric state, with the ratio of gamma width to delayed fission width $\mu_\gamma/\mu_f \approx 5$. Bartsch *et al.* (1978) did not observe the transition observed by Habs *et al.* (1975) and placed an upper limit of $\mu_\gamma/\mu_f < 1.5$ at $E_\gamma \approx 2.5$ Mev., following population of the shape isomer by the $^{238}U(\gamma,2n\gamma')$ $^{236}U$ reaction. Recently Butler *et al.* (1980) reported their experimental upper limit for the branching ratio, ranging from $\mu_\gamma/\ \mu_f < 4.5$ at $E_d$=.5 Mev. to $\mu_\gamma/\mu_f < 1.5$ at $E_d$=2.5 Mev. for a single gamma cascade, following non-observation of the gamma back-decay in a $^{236m}U$ produced in the reaction $^{235}U(d,p)$ $^{236}U$ at $E_d$=11 Mev. The first observed back-decay gamma transition from deexcitation of a shape isomer was that of $^{238m}U$. Russo *et al.* (1974) succeeded in observing gamma transitions from the shape isomeric decay of $^{238m}U$ produced in the $^{238}U(d,pn)$ $^{238m}U$ reaction at $E_d$=18 Mev. They precisely determined the excitation energy of the isomeric state to be 2.559 Mev (see LHS of fig. 2-12). In all of these searches direct reactions have been employed to populate the shape isomeric state in the residual nucleus. As mentioned before, it had also been proposed that the negatively-charged muon could be used to produce the isomer by direct excitation by radiationless transition between lowest atomic levels during the atomic cascade. The search performed by a CERN group (Fromm *et al.* ,1976) for the gamma decay of the shape isomeric state in muonic $^{238}U$ has resulted in observation of several delayed gamma rays. Two transitions with $E_\gamma$=2215 and 3131 kev were attributed to the decay of the shape isomeric state into levels in the first well. Their proposed level scheme is shown in fig. 2-12 (RHS).

The muon probe has a peculiar feature that encourages its use for inducing shape isomer excitation when searching for back-decay gamma transitions. The double humped barrier for a

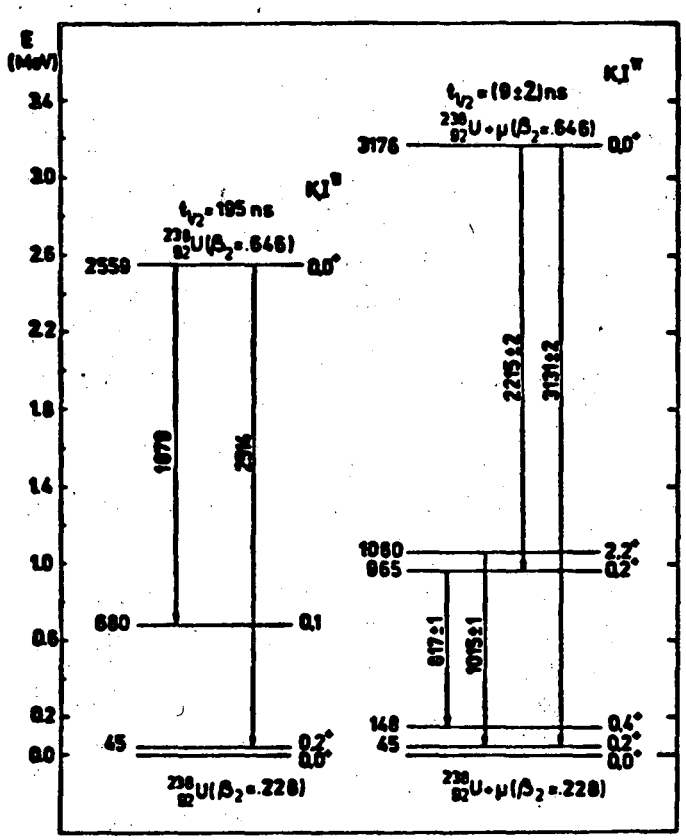


Fig. 2-12 Proposed decay schemes from the shape isomeric state in $^{236}$U without the muon (Russo et al. 1974) and with the muon in the 1s orbit. All transition energies are in kev, and β is the quadrupole deformation of the nucleus (Fromm et al. 1976).

muonic nucleus is different from that of a bare nucleus. In fact, the binding energy of a negative muon in the K shell of a shape isomer produced by a muonic radiationless transition induces some perturbation into the height of the barriers. The fission barrier in the presence of a muon $E_N^{\mu}(s)$ is $E_N^{\mu}(s)=E_N^{0}(s)+E_{\mu}(s)$ , where $E_N^{0}(s)$ is the fission barrier in the absence of the muon, $E_{\mu}(s)$ is the muon binding energy as a function of deformation and s is any nuclear deformation parameter. Zaretsky and Novikov (1961) have calculated $E_{\mu}$ by solving numerically the nonrelativistic Schrodinger equation for a charged particle in the coulomb field of a sharp, homogeneous charge distribution with a purely spheroidal shape. Leander *et al.* (1975) considered a more general case of an arbitrary, axially symmetric shape. Their results reveal that the augmentation of the barrier is relatively insensitive to the effects of multipole deformations higher than hexadecapole. However, both calculations show that the binding energy of the muon in the K-shell is sensitive to quadrupole deformation, and the quadrupole moment of the shape isomeric state should lower it by several hundreds of kev. The effect of the muon binding energy on the double humped barrier is shown in fig. 2-13 . The shift in the energy of the isomeric state and the relative change of the barrier heights due to the presence of the muon make it much easier for the isomeric state to penetrate the inner barrier, and this depresses the fission channel.

According to a theoretical model developed by Nix and Walker (1969), in order for the gamma branch to compete effectively with the fission branch in the process of shape isomeric deexcitation, the inner barrier penetrability , $P_A$, must be several orders of magnitude larger than that of the outer barrier. This arises from the relative slowness of the electromagnetic transition compared to fission. Once the nucleus has tunneled through the outer barrier it always fissions with a characteristic time of $10^{-21}$ seconds, the period of vibration in the second well which determines the frequency of barrier assaults. In the first well, however, the electromagnetic transition is slow, and the repenetration of the inner barrier to the second well competes with radiative process. The expression for the partial life time $T_{i,\gamma}$ of the gamma branch from the shape isomeric state to the normal ground state is in the form

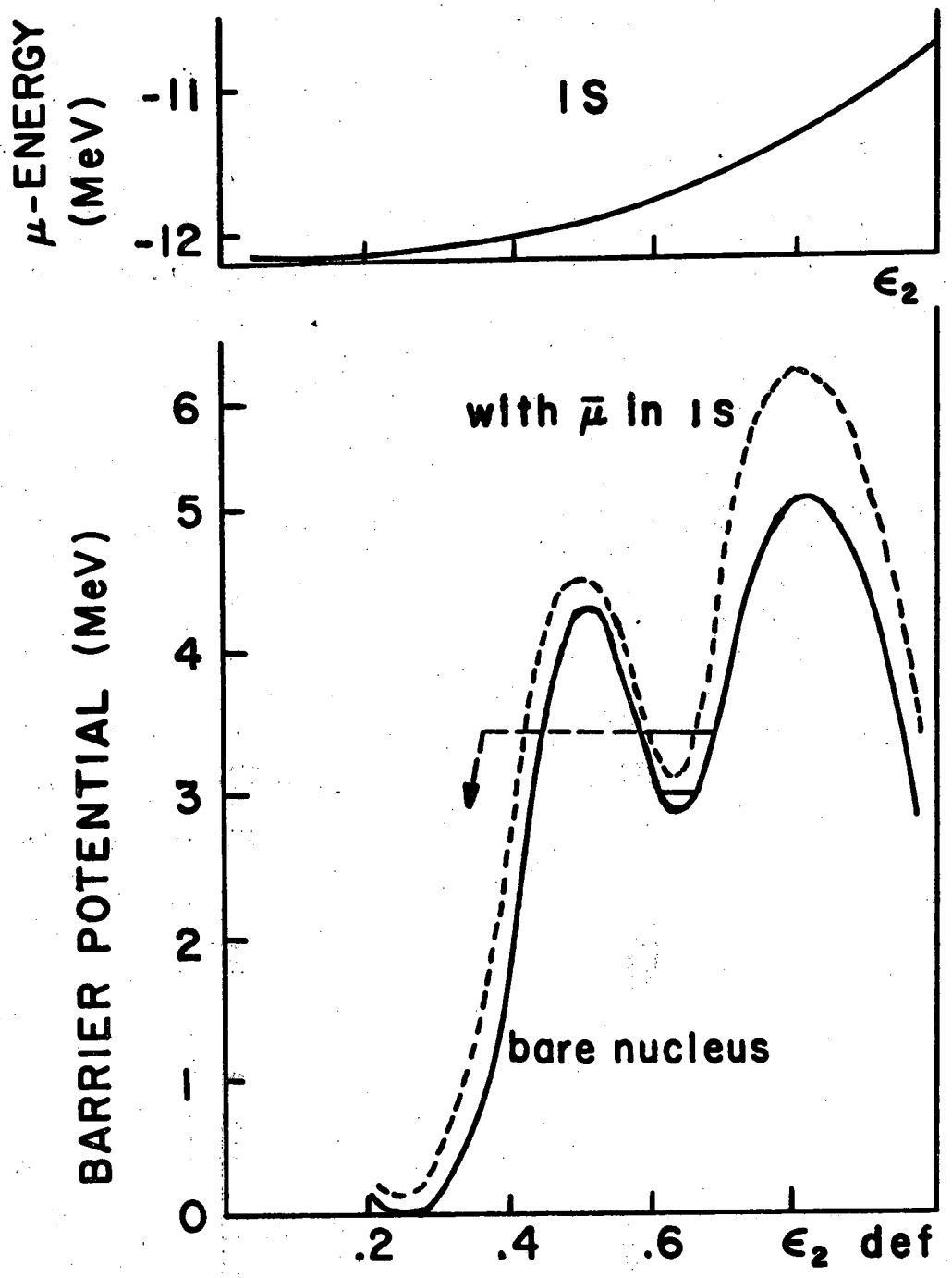


Fig. 2-13 The effect of the muon binding energy on the double-humped barrier.

$$\frac{1}{T_{i,\gamma}} = \sum_{f,\lambda,\gamma} C_\lambda E_\gamma^{2\lambda+1} \left| \langle f \mid O_{\lambda\mu}^{\sigma} \mid i \rangle \right|^2 \tag{2-12}$$

where $C_\lambda$ is a known coefficient that depends upon the angular momentum $\lambda\bar{h}$ of the emitted photon, $E_\gamma$ is the energy of the emitted photon and $O_{\lambda\mu}^{\sigma}$ is the operator for the emission of a photon of total angular momentum $\lambda\bar{h}$ and Z component $\mu\bar{h}$. The symbol $\sigma$ characterizes the transition as electric (E) or magnetic (M). The wave function for the initial state (isomeric) state $|i\rangle$ can be expressed as a linear combination of states in the first and second minimum

$$| i\rangle = \alpha \mid i_{II} \mid + \beta \mid i_I \mid \tag{2-13}$$

where $i_I$ and $i_{II}$ are components in the first and second well of the double humped barrier. Assuming that $| i_{II}\rangle$ and $| i_I\rangle$ are orthogonal and already normalized

$$| \alpha |^2 + | \beta |^2 = 1 \tag{2-14}$$

In general $| \beta |$ is substantially smaller than $| \alpha |$ except for the near coincidence in the energy levels of the first and second well. Since the overlap between the final state $|f\rangle$ in the first well with the component $| i_{II}\rangle$in the second well ($\langle f \mid i_{II}\rangle$) is negligible equation (2-12) reduces to

$$\frac{1}{T_{i,\gamma}} \approx | \alpha |^2 \left[ \sum_{f,\lambda,\gamma} C_\lambda E_\gamma^{2\lambda+1} \left| \langle f \mid O_{\lambda\mu}^{\sigma} \mid i_I \rangle \right|^2 \right] \tag{2-15}$$

the quantity $| \alpha |^2$ is simply the inner barrier penetrability, and the quantity in the brackets is approximately the electromagnetic transition rate in the first well. The expression then becomes

$$\frac{1}{T_{i,\gamma}} = P_A/T_\gamma \tag{2-16}$$

where $T_\gamma$ is the half life for electromagnetic transition to the first well. Using the experimentally known values of $10^{-14}$ sec ($10^{-21.5}$ yr.) for $T_\gamma$ and assuming a very small amplitude of the state $| i\rangle$ in the region of the first well, the partial half ife for the gamma branch is

$$T_{i,\gamma} = 10^{-14}/P_A \tag{2-17}$$

The partial half life for isomeric fission is

$$T_{i,f} = n/P_B \tag{2-18}$$

where $P_B$ is the penetrability of the outer barrier and n is the number of assults on the outer barrier from the isomeric state per second. Assuming a reasonable value of 1 Mev. for $\bar{h}\omega$ (the vibrational spacing in the second well) gives

$$T_{i,f} = 4\times10^{-21}/P_B \tag{2-19}$$

The ratio of partial width for these processes $\mu_{i,\gamma}/\mu_{i,f}$ which in inverse of $T_{i,\gamma}/\ T_{i,f}$ can be expressed as

$$\mu_{i,\gamma}/\mu_{i,f} = 4\times10^{-7}P_A/P_B \tag{2-20}$$

This suggests that for equal yield in the gamma and fission branch of the shape isomeric state, the inner barrier must be $2.5\times10^6$ time more penetrable than the outer one. For non-muonic $^{238}U$ for example, the values for parameters involved in calculations of the penetrabilities $P_A$ and $P_B$ (equations 2-6 and 2-7) are given (in Mev) to be:

$E_A = 5.90, E_B = 6.12, E_i = 2.56, \bar{h}\omega_A = 1.18, \text{and} \bar{h}\omega_B = .63$ (Russo *et al.* , 1975), which gives

$$P_A/P_B \approx 5\times10^7$$

which translates into a gamma back-decay partial width 20 times larger than the partial fission width for decay of the $^{238}U$ shape isomeric state. The effect of the muon binding energy on the ratio of the partial width can be be estimated by allowing for appropriate shifts in the isomeric state and the height of the barrier. These shifts are obtained (Fromm *et al.* ,1976) for muonic $^{238}U$ from calculation of the muon binding energy by solving the Dirac equation for a deformed Fermi-type charge distribution. The new values for the parameters of the fission barrier of the

muonic $^{238}U$ are given as: $E_A = 6.18, E_B = 7.18, E_i = 3.12$ Mev. The ratio of penetrabilities then becomes

$$P_A/P_B \approx 3\times10^{10}$$

which predicts ≈600 times enhancement of the muonic $^{238}U$ gamma back-decay compared to a bare $^{238}U$ nucleus. This favorable effect of muon binding energy, as well as the predicted high probability for population of the shape isomeric state in a muonic radiationless transition provides a strong incentive for use of the muon probe to induce the shape isomeric state, when the objective is to study its gamma branch of deexcitation.

### 2.6.1. Muonic Atom And Muon Induced Channels

Formation of a muonic atom is complete once a negatively charged muon having lost all of its kinetic energy through ionization and excitation processes is stopped and finally captured by an atom into high orbital momentum states.(C.S.Wu *et al.* 1969). Muon orbits are much smaller than electronic orbits. For example, a muon orbit of the same size as the K shell electronic orbit $n_e=1$ will have a principal quantum number

$$n_\mu \approx \left(\frac{m_\mu}{m_e}\right)^{1/2} \approx 14 \qquad (2\text{-}21)$$

Transitions from these high orbits to lower states involve low energies so that they can interact with outer electrons and yield a strong "Auger effect". However, at low n values the transition energy increases rapidly according to $n^{-3}$. Therefore, the radiative transitions dominate. The whole cascading process is very fast and ultimately, as the muon reaches the lowest state (K-shell) it can experience either of the two fates:

- Electron decay with a half life of $2.2\times10^{-6}$sec.

$$\bar{\mu} \rightarrow \bar{e} + \bar{\nu}_e + \nu_\mu \qquad (2\text{-}22)$$

- Capture by the nucleus

$$(A,Z) + \bar{\mu} \rightarrow (A,Z-1) + n + \nu_{\mu} \qquad (2\text{-}23)$$

The capture rate over a wide range of isotopes can be predicted by the well-known Goulard-Primakoff (1974) formalism. The characteristic lifetimes for muonic actinides are 70-80 nsec. and the muon capture excites the nucleus on the average to approximately 15 Mev., which is sufficient to open several channels including fission and gamma decay in the deexitation mode of the nucleus.

Over twenty years ago Zaretsky and Novikov (1961) postulated that a muon in the 2P orbit,instead of emitting an X-ray would have a finite probability to excite the nucleus via an E1 transition , a so called "radiationless" transition. Since in the case of the muonic actinides the energies of the transitions between low-lying atomic levels are larger than the neutron binding energies and the fission barrier, radiationless muonic cascade transitions may result in the neutron emission or fission in the presence of a bound muon. A sampling of the reaction histories possible after the muon had proceeded through the initial stages is shown in fig. 2-14. Most frequently muonic X-ray transitions will occur until the muon reaches its 1S ground state, where it can decay or be captured. The latter can cause nuclear fission and/or the emission of neutron and gamma rays. In addition, there is significant probability for radiationless muonic cascade transitions such as the 2p-1s or 3d-1s transitions (Zaretsky 1961; Lohs *et al.* 1974), leading to prompt neutron emission or fission followed by subsequent capture of $\bar{\mu}$ by the heavy fragment. Furthermore, radiationless transitions may result in a population of the shape isomeric state in the second well of the nuclear potential (Blocki *et al.* 1972; Bloom,1974). From the isomeric state the nucleus may undergo delayed isomeric fission, back-decay to the ground state or capture the muon. In the present work the back-decay mode of the isomeric state has been investigated and will be discussed.

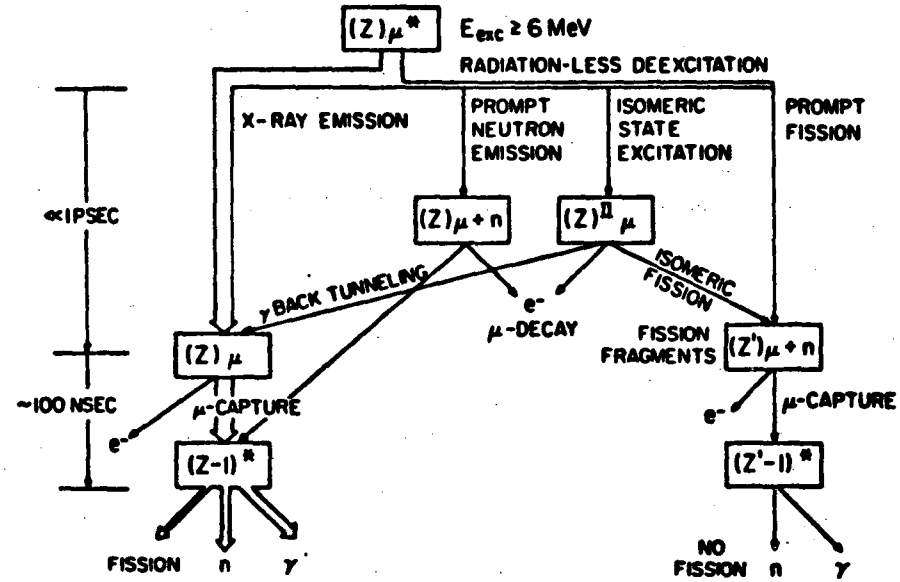


Fig. 2-14 Muon induced reaction channels for actinides (fig. from W. W. Wilke et al. 1978).

### 2.6.2. Radiationless Transition

The experimental evidence for the non-radiative mesic transition in actinide nuclei first came for the work of Diaz *et al.* (1959). They concluded that nearly 6% of their observed muon induced fissions which occurred promptly were due to radiationless transitions of the $\bar{\mu}$ mesons to the 1s state. Later the experimental results of Balatz *et al.* (1960) and Mukhin *et al.* (1960) showed that the intensity of the meson x-ray photon corresponding to the transition $2p \rightarrow 1s$ is smaller in $^{238}U$, $^{235}U$ and Th than in Pb, indicating the presence of radiationless transitions in heavy mesic atoms. The theory of nonradiative transition is discussed in the pioneering work of Zaretsky and Novikov (1961). It is known that in heavy elements the mean radius of the 2p states is comparable to the nuclear radius, so that in a 2p-1s transition the muon may transfer its quantum of energy to the nucleus.

A muon-nucleus system can be represented by a Hamiltonian H of the form

$$H = H_N + H_\mu + H_{\mu N} \tag{2-24}$$

where H is the Hamiltonian of the nucleus, $H_\mu$ operates only on muon variables, and $H_{\mu N}$ is the operator of the muon nucleus interaction. The muon-nucleus interaction operator is in fact responsible for radiationless transition and may be given by

$$H_{\mu N} = -e^2 \sum_{i=1}^{Z} \frac{1}{| \vec{r}_\mu - \vec{r}_i |} \tag{2-25}$$

where $\vec{r}_\mu$ and $\vec{r}_i$ are the radius vectors of a muon and a proton respectively. The summation is performed over all protons within the nucleus, and Ze represents the nuclear charge. Expanding equation (2-25) in a series of spherical harmonics for the dipole interaction ($l = 1$) we find

$$H_{\mu N} = \frac{-4}{3}\pi e^2 \sum_{i=1}^{Z} \sum_{m=-1}^{1} Y_{1m}(i)\, Y^{*}_{1m}(\mu) \times \begin{cases} \dfrac{r_i}{r_\mu^2} & \text{when } r_\mu > r_i \\ \dfrac{r_\mu}{r_i^2} & \text{when } r_\mu \leq r_i \end{cases}$$

For the initial state with muon in the 2p state the main function of the muon nucleus system is

$$\psi_i = \phi_0 R_{2p} Y_{lm}(\mu) \tag{2.27}$$

were $\phi_0$ is the wave function of the nucleus in the ground state and $R_{2p}Y_{lm}(\mu)$ is the muon wave function in the 2p state. The wave function for the final state is

$$\psi_f = \phi_{1M} \frac{1}{\sqrt{4\pi}} R_{1s} \tag{2-28}$$

where $\phi_{1M}$ is the wave function of the excited state of the nucleus with spin 1 and spin projection M, and $\frac{1}{\sqrt{4\pi}} R_{1s}$ is the wave function of the muon in the ls state. The width of the radiationless transition is then given by

$$\Gamma_{r.l.} = 2\pi\rho \left| < \psi_f \mid H_{\mu N} \mid \psi_i > \right|^2_{av.} \tag{2-29}$$

where $\rho$ is the nuclear level density. Taking the width of the radiative transition to be

$$\Gamma_{rad} = \frac{4e^2\omega^3}{9c^3} \left| \int_0^\infty r^3 R_{1s} R_{2p}\, dr \right|^2 \tag{2.30}$$

and after some substitutions and manipulations Zaretsky and Novikov (1961) obtained the following expression for the ratio of radiationless to radiative transitions

$$\frac{\Gamma_{r.l.}}{\Gamma_{rad}} = \frac{2\pi^2 m_\mu^2 \omega\, c^3}{Z^2 e^2}\rho \left| < \phi_1 \mid \Sigma q_i \frac{f(r_i)}{f(R)} \mid \phi_0 > \right|^2_{av.} \tag{2-31}$$

where $q_i = r_i . Y_1(i)$, R is the nuclear radius, and $f(r_i)$ is given as

$$f(r_i) = \frac{1}{r^3} \int_0^{r_i} r^3 R_{1s} R_{2p} \, dr + \int_{r_i}^{\infty} R_{1s} R_{2p} \, dr \qquad (2\text{-}32)$$

The dipole photoexcitation cross section $\sigma$ has the following form:

$$\sigma = \frac{16}{3} \pi^3 \frac{\omega}{c} e^2 \rho \left| < \phi_1 | \sum_i q_i | \phi_0 > \right|^2_{av.} \rho \qquad (2\text{-}33)$$

Using this, Zaretsky and Novikov (1961) reduced the expression in (2-31) to

$$\frac{\Gamma_{r.l.}}{\Gamma_{rad}} = \frac{3}{8\pi} \left( \frac{m_\mu c^2}{Ze^2} \right) \sigma B \qquad (2\text{-}34)$$

where

$$B = \frac{\left| < \phi_i | \sum_i q_i f(r_i) | \phi_0 > \right|^2_{av.}}{\left| < \phi_1 | \sum_i q_i f(R) | \phi_0 > \right|^2_{av.}} \qquad (2\text{-}35)$$

The form factor B takes account of the influence of the nuclear finite dimension.

Estimating a value of $B \approx 1.8$ and $\sigma \approx 50$mb, Zaretsky and Novikov (1961) obtained the ratio of radiationless to radiative transition for muonic $^{238}U$

$$\frac{\Gamma_{r.l.}}{\Gamma_{rad}} \approx 0.7 \qquad (2\text{-}36)$$

and so $\Gamma_{r.l.}/(\Gamma_{r.l.}+\Gamma_{rad}) \approx .41$ is obtained. This is larger than the calculated value of 0.24 by Teller and Weiss (1979) and the experimental result of 0.23 (Balatz *et al.* 1960, 1961), but in good agreement with the value of $\Gamma_{r.l.}/(\Gamma_{r.l.}+\Gamma_{rad}) \approx .4$ obtained by Khan and Knowles (1972).

### 2.6.3. Muon Induced Shape Isomer

The belief that the shape isomeric state may be appreciably populated in a radiationless muonic transition originated from Bloom's work (1974). His proposed model was intended to explain the discrepancy between the $\mu^- - ^{238}U$ decay characteristic when measured by electron

decay ($\tau_e$ = 87ns) and by fission fragment ($\tau_f$ = 75ns).

He hypothesized that a significant fraction of the 2p-1s muonic transitions excite, nonradiatively, the shape isomeric state in $^{238}U$ and that the apparently lower $\mu^-$ lifetime as measured from fission fragments is due to the combined effect of the alternative pathways to fission, $\mu^-$ capture and isomer decay. The simple model used by Bloom (1974) is applied to the situation when all prompt events following radiationless transition are settled. Then the muonic atom can exist in one of two states: a normal state, with the muon in a 1s state around the ground state nucleus; and an isomeric state, in which the muon orbits the shape isomer. Denoting the number of systems in these two states with $N_1$ and $N_2$ respectively, Bloom writes the rate equations

$$\dot{N}_1 \approx -\lambda_c N_1 + \lambda_{bt} N_2 \tag{2-37}$$

$$\dot{N}_2 \approx -\lambda_i N_2 \tag{2-38}$$

$$\lambda_i = \frac{1}{\tau_i} = \lambda_{ic} + \lambda_{if} + \lambda_{bt} \tag{2-39}$$

where $\lambda_c$ is the muon nuclear capture rate, $\tau_i$ is the shape isomer lifetime, $\lambda_{ic}$, $\lambda_{if}$, and $\lambda_{bt}$ are the capture rate, fission rate and the back-tunneling rate from the shape isomeric state, respectively. From these equations Bloom (1974) obtains the following results for the time dependence of the population $N_1(t)$ and $N_2(t)$

$$N_1(t) = N_{10} \exp(-\lambda_i t)\ (1+f\epsilon)\ \left\{1 - \frac{f\epsilon}{1+f\epsilon} \exp[-(\lambda_{if} + \lambda_{bt})]\right\} \tag{2-40}$$

$$N_2(t) = \epsilon\, N_{10} \exp(-\lambda_i t) \tag{2-41}$$

$$f = \frac{\lambda_{bt}}{\lambda_{if} + \lambda_{bt}} \tag{2-42}$$

then he finds the rate of electron emission $n_e$ and fission $n_f$

$$n_e' = \lambda_0 (N_1 + N_2) \tag{2-43}$$

$$n_f' = \alpha \lambda_c (N_1 + N_2) + \lambda_{if} N_2 \tag{2-44}$$

where $\lambda_0$ represents the "natural" electron-decay rate of the muon, $\alpha$ is the (fission/capture) probability, and $\epsilon$ is the initial population ratio $N_{20}/N_{10}$.

From equation (2-41) and (2-44) it is clear that $n_f'/n_c'$ will not be constant if the isomeric state is not zero ( $\epsilon \neq 0$). In other words, the presence of some initial population of the shape isomeric state can explain the different time dependence of the electronic and fission modes. For sufficiently small values of $\epsilon$ and $\lambda(\lambda_{if} + \lambda_{bt})$ the ratio $n_f'/n_e'$ can be translated into an approximate exponentially decaying function in time

$$n_f'/n_e' \approx \text{const} \cdot \exp(-\lambda_d t) \tag{2-45}$$

where $\lambda_d \mp \lambda_f - \lambda_e = \frac{1}{\tau_f} - \frac{1}{\tau_e}$ with $\lambda_f$ and $\lambda_e$ being the observed fission and electron decay probabilities per unit time respectively. Using the described model above with the assumption of pure exponential decay characteristic for $n_f'$ and $n_c'$, Bloom gives the following expression for $\lambda_d$

$$\lambda_d \approx \epsilon \lambda_{if} (\lambda_{if} + \lambda_{bt})/\alpha\lambda_c \tag{2-46}$$

then he calculates $\epsilon$ by substituting the experimental value available for probability difference $\lambda_d = (1.8 \pm .4) \times 10^6 \text{ sec}^{-1}$ and the available values for other parameters, for the case of $\mu^-$ capture in $^{238}U$

$$\epsilon \approx \alpha \lambda_c \lambda_d / \lambda_{if} (\lambda_{if} + \lambda_{bt}) \tag{2-47}$$

$$\epsilon(^{238}U) \approx 1.0$$

This optimistic value for $\epsilon$ suggests that the isomeric state and the normal ground state are about equally populated in a radiationless muonic $^{238}U$ decay, which means that the exponential

approximation should not have been used. The isomeric population ratio $\epsilon \approx 1.0$ differs by several orders of magnitude from the value obtained (Vandenbosch, 1973) in nucleon induced reactions. As pointed out by Bloom (1974), not much reliance should be placed on his number, because of unjustified approximations.

In contrast to Bloom's proposed model, Hadermann (1977) emphasized the importance of the sequential atomic muon capture by fragments resulting from prompt muon-induced fission. He argued that the possible differences in the experimental fission and electronic decay lifetimes may be indicative of the muon's history after a prompt fission event. Evidence in support of Haderman's proposal have been obtained by Ganzorig *et al.* (1978) by measuring muon-decay electrons in coincidence with prompt fission fragments in $^{232}$Th and $^{238}$U by Wilcke *et al.* (1981) and by Schroder *et al.* (1979) by observing long-lived components in the time spectra of neutrons emitted from the highly fissile muonic $^{237}$Np, $^{239}$Pu and $^{242}$Pu and measuring lifetimes of muons bound to fission fragments. Although there remains no question about the occurrence of muon capture by fission fragments, it has not been shown that this mechanism is the only one responsible for the difference between measured lifetimes (Schroder *et al.* 1979). However, the question of shape isomeric state population by radiationless transition in muonic actinides had to be resolved by measurements on the isomer decay products. Because of the lower height of the inner barrier for low $\dot{Z}$ actinides (Nilsson, 1970), together with the augmentation of the height of the second barrier due to the presence of the muon in 1s orbital (Leander et al. 1975), the back-decay gamma ray seemed to be the most feasible candidate for such a measurement. Some previous works (Russo *et al.* 1974, Kaplan *et al.* 1976, Fromm *et al.* 1976, Butler *et al.* 1980), as well as the present experiment, have concentrated on this measurement.

# CHAPTER 3

# EXPERIMENTAL ARRANGEMENT AND PROCEDURE

## 3.1. Introduction

The goal of the present experiment was to investigate the gamma back decay branch of the shape isomeric state deexcitation in muonic uranium isotopes. The lifetime and the energy spectra of the gamma rays following negative muon capture were measured. Delayed coincidence with a secondary gamma ray was required to suppress the background from the muon nuclear capture in the target. The muon beam was obtained from the M9 stopped $\mu$—$\pi$ channel (Al-Qazzaz *et al.* 1980) at the TRIUMF meson facility. Muon stops were identified by a conventional four- scintillator telescope. The time of flight technique was used to identify $\mu^-$ from $e^-$ and $\pi$ contaminations.

In the 1979 run, a large volume (15%) intrinsic Ge and seven NaI detectors (5 3″×3″ and 2 2″×2″ ) were used to record gamma radiation. The main target was $^{238}$U and some $^{235}$U data was also taken.

The 1980 run was in fact an improved version of the previous run, using larger detectors and implementing some changes in the logic design, which will be discussed in section 3.4 and 3.5 of this chapter. The set up consisted of one 20% (80 cm$^3$) Ge(Li), one 10% (40 cm$^3$) intrinsic Ge and three 5″×6″ NaI detectors.

For our 1981 run, the $^{236}$U target was used . This would be the first $^{236}$U gamma back-decay experiment using negative muon as a probe to excite the shape isomeric state, while direct reactions have been used in all previous experiments. The set up for this experiment was essentially similar to that of 1980 run.

### 3.2. Accelerator and Beam

At TRIUMF, pions are produced by a proton beam of up to 100 $\mu$A, from the 500 Mev cyclotron, impinging on an external target. To obtain the maximum available flux and lower electron contamination a 10 cm beryllium target was used. Pion decay near the production target resulted in the "cloud" muons used in the present experiments. Some contaminant electrons are also produced, mainly from $\pi$ decay and to some extend from the $\mu^-$ electron decay. Production of these particles at the beryllium target occurs in the form of 5 ns pulses separated 43 ns apart (cyclotron frequency of 23 MHZ).

The M9-channel (Al-Qazzaz *et al.* 1980) was designed to produce a high flux of stopping pions and cloud muons of both polarities over a momentum range of 30-150 Mev/c. A crossed-field velocity filter, 3 meters in length, was added to the M9 channel in 1979. After the installation of this extension to the channel ( Macdonald, 1980) it produced muon beam of momentum $\leq$ 80 Mev/c with a much reduced $\pi^-$, $e^-$ contaminations.

In our experiments the channel was tuned for negative polarity and a set momentum range ( nominally $\leq 100 \pm 10$ % Mev/c). The application of time-of-flight technique to separate negative muons from pions and electrons was based on the fact that these particles transmitted by the channel , having almost equal momenta, travel with different velocities and reach the experimental area with different flight times, which may be resolved experimentally . To increase the stop rate within the uranium target, the muon beam was slowed down by placing absorbers between the scintillators. The pion contamination in the stopping beam was completely eliminated by the proper choice of absorber thickness, using the fact that for the same momentum pions have shorter range than muons.

### 3.3. Experimental Geometry

The top views of the geometrical arrangements of the experimental set ups for 1979 and 1980 runs are shown in the schematic diagrams of figs. 3-1-a and 3-1-b respectively. The set up of the 1981 run was basically the same as that of 1980. The dimensions of the NaI detectors as

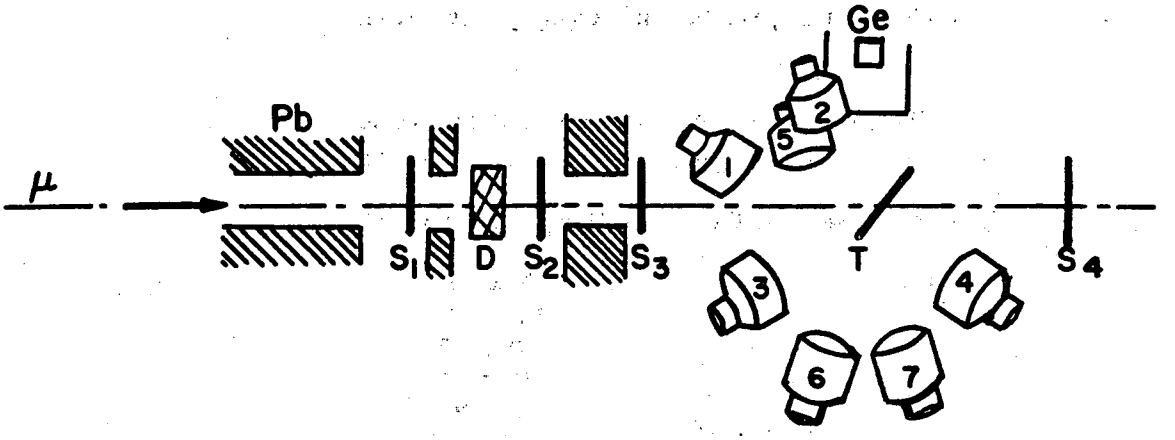


Fig. 3-1-a Experimental set up used in 1979 run

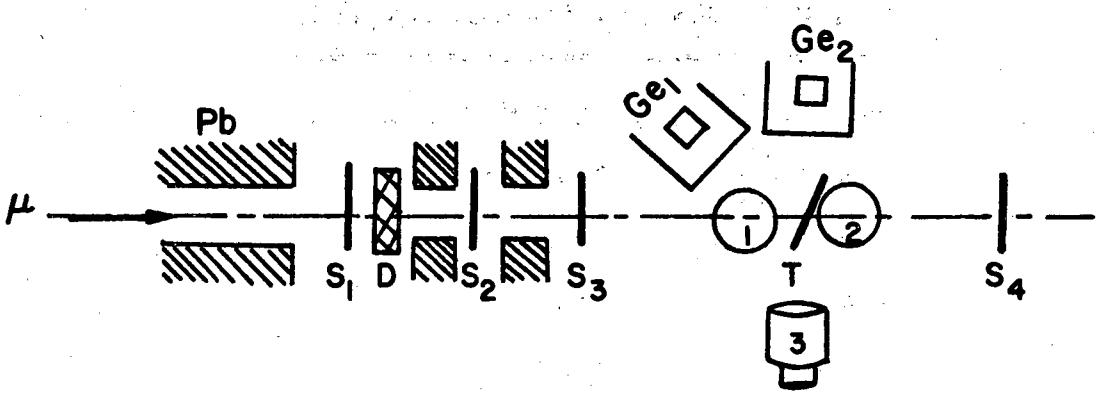


Fig. 3-1-b Experimental set up used in 1980 run

well as their locations with respect to the beam line are given in table III-1.

Table III-1 Dimensions and locations of NaI detectors used

| Detector | Dimension | Location w.r.t. beam line |
|---|---|---|
| NAI-1 | 3″x3″ | above-left |
| 2 | 2″x2″ | above-left |
| 3 | 3″x3″ | above-right |
| 4 | 3″x3″ | above-right |
| 5 | 3″x3″ | below-left |
| 6 | 2″x2″ | below-right |
| 7 | 3″x3″ | below-right |

To avoid direct beam impinging on the detectors, Ge and NaI detectors were placed at a distance of about 4-5 inches from the target center. The dimensions of the scintillator counters S1,....,S4 are specified in table III-2.

Table III-2 Dimensions of the telescope counters

| Counter | Dimension |
|---|---|
| S1 | 4″x4″x (1/16)″ |
| S2 | 4″x4″x (1/16)″ |
| S3 | 2″D x (1/32)″ |
| S4 | 10″D x (1/8)″ |

The scintillator telescope was used to identify the particles stopping in the vicinity of the target. The polyethylene degrader plate D was placed between S1 and S2 in order to slow down the beam and consequently increase the rate of muon stopping in the uranium target. Furthermore, the degrader served as an absorber of pions as it stopped the more massive pions completely and hence reduced the beam contamination. A polyethelene plate thickness of 3/4″ was found

to give the optimum $\pi^-/\mu^-$ ratio. Some information on the targets used in our experiments are given in table III-3.

Table III-3 Targets specifications

| | |
|---|---|
| $^{238}U$ | 1 g/cm$^2$ |
| $^{235}U$ | 25 gm. total |
| $^{236}U$ | 1 g/cm$^2$ and 50 gm. total |

The $\mu^-$ beam was collimated using lead shielding. This as well as some additional lead shielding which was placed around the beam line in between the scintillator counters (as shown in the figs.), were necessary to lower the background level arising from the beam halo and x-rays from various sources.

### 3.4. Muon Stopping Telescope

Scintillator telescopes are commonly used in most muon experiments, primarily to record muon stopping in the target and sometimes to discriminate against contaminant electrons. The muon stop signal is then used to trigger recording of necessary information about desired events following muon stopping. Since the activity resulting from the ordinarily low muon stopping rate is usually rather weak, this triggering is crucial to eliminate the background activities which are not related to actual muon stoppings.

In our experiments, signals from the telescope scintillators S1,...,S4 were sent to the counting room from the experimental area through 50 ohm, low capacity , 30 meter long cables. The signals, suitably delayed and in some cases shaped to minimize overshoot, were fed to discriminators where a threshold of about 50 mv was set to eliminate most of the photomultiplier and electronic noise. The stop logic design used in the 1981 run is shown in fig. 3-2. The standard telescope logic $1.2.3.\bar{4}$ was used to define a stop in the target. All incoming particles were detected by counters S1 and S2. The discriminator NIM outputs for S1, S2 and S3 were set to

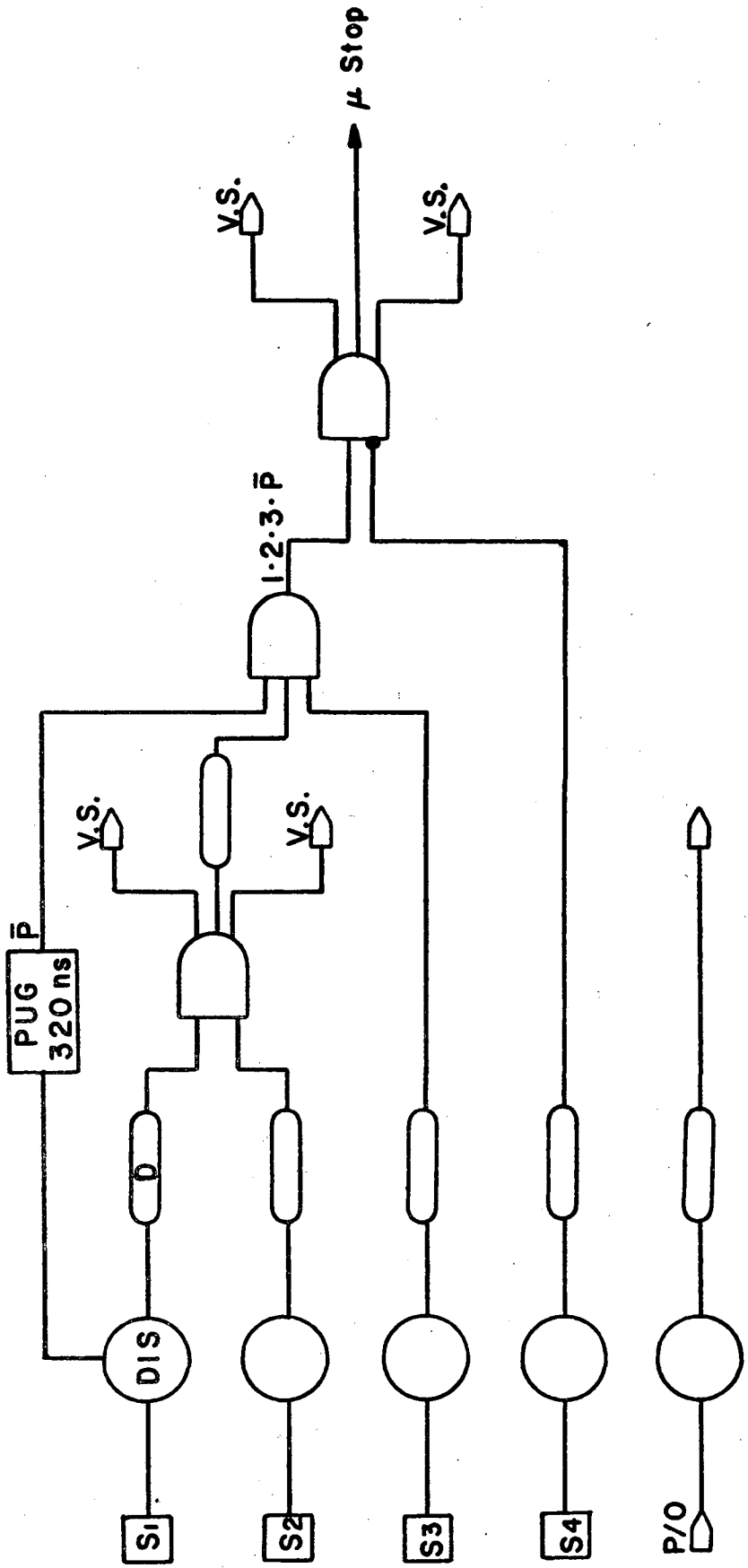


Fig. 3-2 Muon telescope used in 1981 run

5 to 20 ns width and a final S1.S2.S3 coincidence was formed. The output of this coincidence was placed in anticoincidence with the longer width S4 pulses to define the stop. Additional bias against electrons and the high energy muons was achieved by requiring large pulses in one of the scintillators. The pion and electron contaminants were further rejected by using a DC separator (1980-81 runs) and also applying the time-of-flight technique, which was implemented through feeding the beam pick-off signal, appropriately delayed, into the stop coincidence to form the $\mu^-$ stop signal. In the 1981 run , the beam pick-off signal was fed to a separate TDC, so that it could be used in the data reduction stage to eliminate events resulting from $\pi^-$ or $e^-$ stops by using appropriate time cuts. The timing of the beam pick-off signal is related to proton bursts striking the meson production target. Events for which two muon stops were registered within about 300 ns were rejected by a pile-up gate (PUG), the no pile-up output ($\bar{P}$) was placed in coincidence with the 1.2.3 or 1.2.3.$\bar{4}$ stop signal. Provision was made to allow all incoming particles to participate in triggering of the pile-up gate. This was achieved by not using as a pile-up monitor the scintillator counter of which the discriminator threshold was raised to reject electrons and high energy muons.

### 3.5. Data Acquisition System and Procedure

The main features of the data acquisition syatem used in the present experiment are shown in the block diagram of fig.3-3. The muon stop logic was discussed in the previous section, the Ge and NaI logics will be discussed in this section. A desired event was characterized by a Ge pulse immediately following a muon stop in the target and delayed coincidence with a signal from one of the NaI detectors. The output of the event trigger,formed from the SGN (stop.Ge.NaI) coincidence, used to gate all TDCs and ADCs, and to strobe the pattern module. The strobe signal, in fact, commands the computer to register the associated event, while the bit pattern set by signals taken from individual detectors informs the computer of the identification of the detector or detectors which fired in that event. In the 1979 run, only one ADC was used, which received the amplitude information from the Ge detector. The timing signals from the

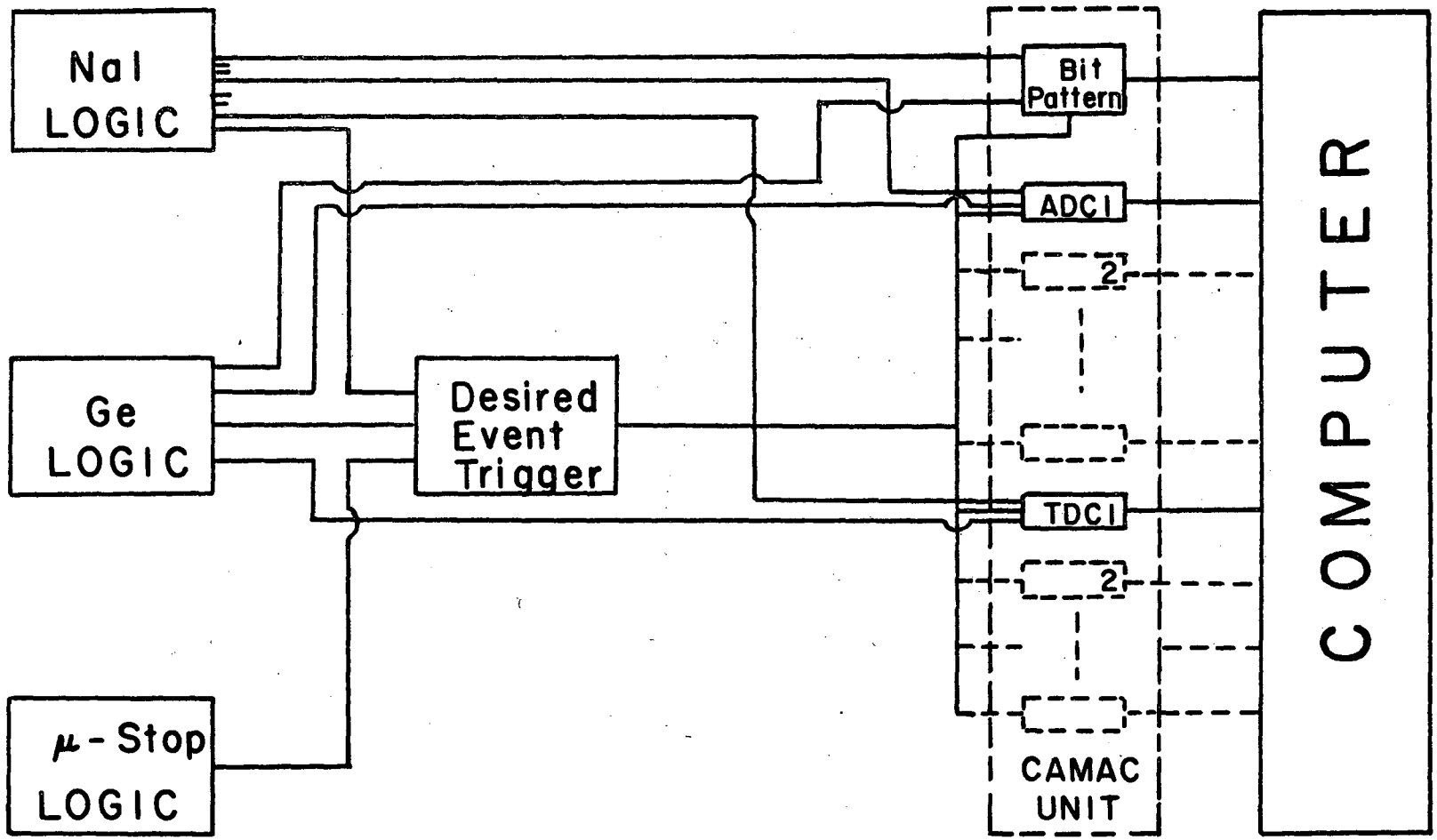


Fig. 3-3 Block diagram of the data aquisition system

Ge and the NaI-OR (any NaI) were registered by two TDCs. In addition each detector producing a signal set a bit in a coincidence buffer module (C212). The bit pattern was then used for identifying the firing detector. In the 1980 and 1981 runs, timing and energy informations from individual detectors went to separate TDC and ADC modules. All the data carrying timing and energy informations about the gamma rays processed in the CAMAC logic units were read by a Nova-computer (PDP11/60 in 1980,81 runs) and recorded event-by-event on magnetic tape. On line analysis was also performed, using the pulse height analysis (PHA) program (Multi in 1980,81 runs) in which some of the data were histogramed and checked at the time of accumulation.

The Ge logic configuration is shown in fig.3-4. The modules in the LHS of the broken lines were set up at the experimental area and their outputs were transmitted to the counting room by 30-meter-long coaxial cables. By the SGN coincidence logic design, the Ge detector is utilized, mainly to measure timing and energy of the muonic X-ray and back decay gamma rays. Energy and timing signals are obtained from the E and T outputs of a low noise charge-sensitive preamplifier. The energy signal amplified and shaped by an amplifier is sensed by the associated ADC. The ADC is gated with a long width SGN coincidence pulse to prevent undesired event from being registered. The timing signal was amplified using a fast timing filter amplifier (TFA). A differentiation time constant of about 100 ns was used to optimize the signal-to-noise ratio. The TFA was followed by a constant fraction discriminator (CFD) with slow rise time reject. The output of the CFD was fed into a multiple output QUAD discriminator with a set threshold to eliminate low energy noise. Four outputs were taken from this module, one was delayed through a LRS-222 module and sent to the Ge TDC stop, another one was used to set a bit in the C212 coincidence buffer, the third output was connected to a CAMAC scaler, and the last output pulse was passed (in 1980 and 1981 runs OR'ed with the output of the second Ge logic) to the desired-event-triggering logic (DET).

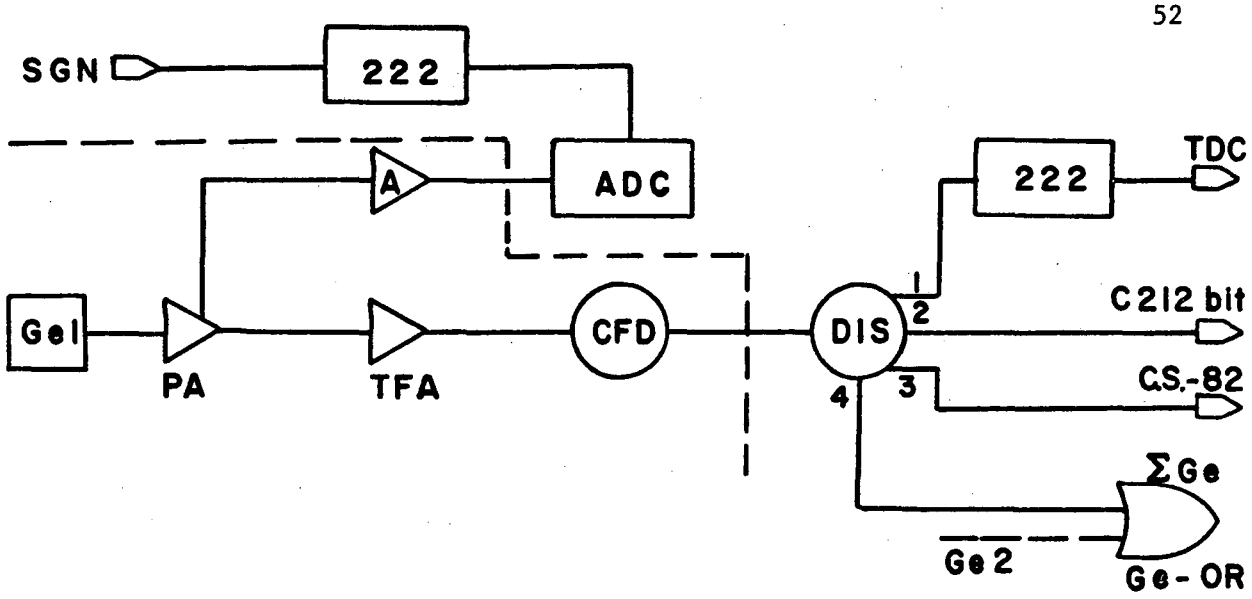


Fig. 3-4 Ge logic design (1980 and 1981 runs)

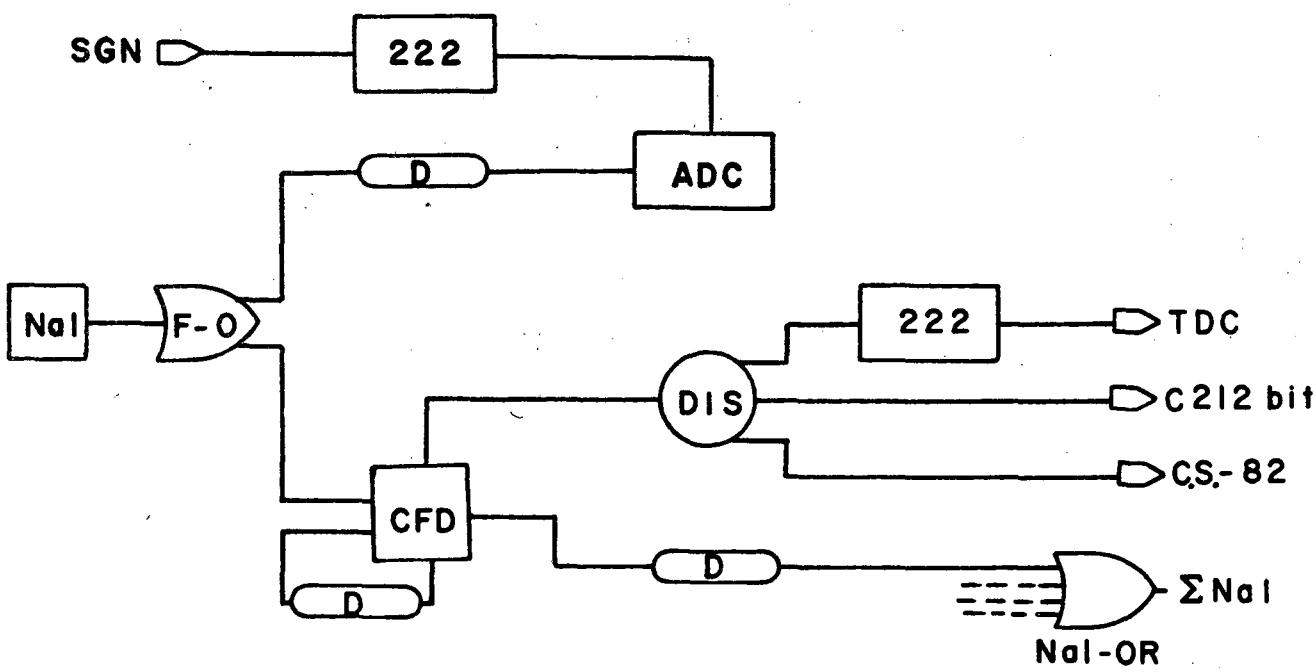


Fig. 3-5 NaI logic design (1980 and 1981 runs)

A typical NaI logic diagram is shown in fig.3-5. In the 1980 and 1981 runs, no amplification of the photomultiplier tubes was necessary and the timing and energy signals were obtained by using a fan-out (F-O) module and fed to the rest of the logic which was essentially similar to that of the Ge logic. The CFD shown in the fig. is a fast module which provides connectors for external shaping delay for the constant fraction signal.

Fig.3-6 gives the overall logic diagram of the 1979 run. The output of the $\mu^-$ stop, Ge and NaI logics are shown as inputs to the rest of the logic. To maximize the efficiency for detection of gamma rays, seven NaI detectors available were used. The logic used for each NaI was the same as the typical diagram shown in fig.3-5, except that in this run each NaI signal was amplified and shaped by a delay line amplifier before being sent to CFD. The NaI timing signals were OR'ed using two successive 4-input OR gates. To veto prompt NaI gamma rays and therefore reduce the chance of accidental coincidences, a prompt signal derived from the S2 scintillator counter and properly delayed was placed in anticoincidence with a $\sum$NaI output to form the d$\sum$NaI signal. Another $\sum$NaI output discriminated against low energy gamma rays was prompt vetoed in the same manner and used to set a certain bit in the C212 coincidence buffer to identify NaI events. A stretched Ge timing signal in coincidence with the d$\sum$NaI signal resulted in the Ge*d$\sum$NaI output. The 650 ns long $\mu^-$ stop timing pulse derived from a LRS-222 module was placed in coincidence with the Ge*d$\sum$NaI output and vetoed by a pile-up signal (P) from the PUG to form the desired event triggering (DET) signal. Common start pulse for TDCs was obtained from anticoincidence of DET with a computer busy signal. The busy signal was provided two LRS-222 modules connected to the computer output registers as shown as shown in fig.3-6. The Ge and $\sum$NaI TDC's are stopped by pulses derived from the respective timing signals stretched to 800 ns delayed by two LRS-222 modules and gated with a DET output. One of the DET*Ge outputs was fed into a gate and delay generator (GDG) to provide an appropriate gating pulse for the Ge ADC.

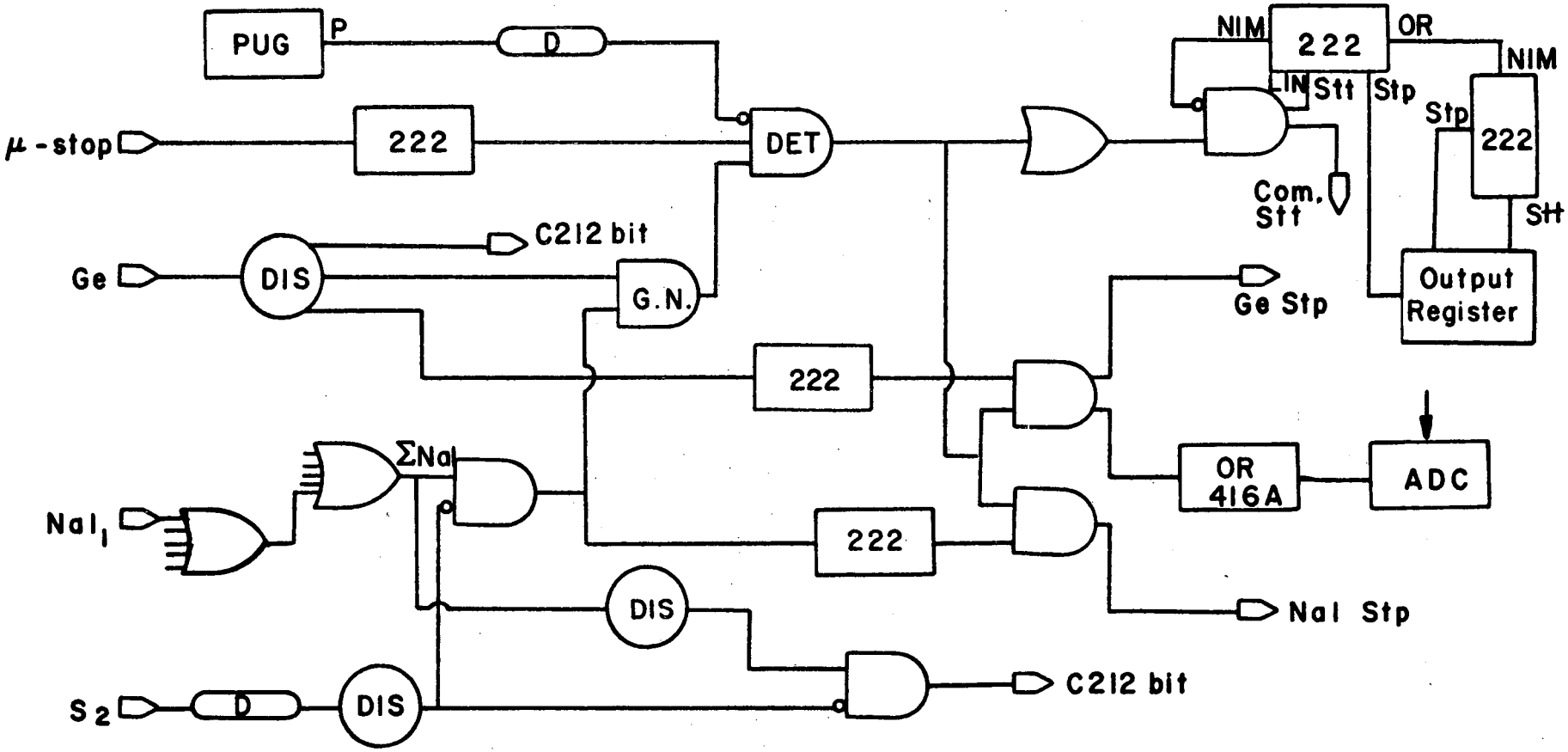


Fig. 3-6 Overal logic diagram of the electronics used in 1979 run

For the 1980 and 1981 run, in which we used two Ge and three NaI detectors, the logic diagram was as shown in fig.3-7. Inputs to the ∑NaI and ∑Ge gates were taken from the timing outputs of the respective NaI and Ge logics. The configuration of the stages used to form the DET pulse were somewhat different from the preceding run. The first stage consisted of the SGN ($\mu^-$ stop*∑Ge*∑NaI) coincidence which was vetoed by a 380$\mu$sec long computer busy signal obtained from a LRS-222 gate-and-delay generator module connected properly to the CAMAC and started by the fourth output of the DET coincidence module. The ∑Ge signal used in the coincidence was a 300 ns long pulse provided by a fast discriminator. The discriminator threshold was set to about 300 mv to eliminate low energy noise. In the final stage the 350 ns wide SGN coincidence output was placed in coincidence with 1.2.3.$\bar{P}$ pulse and anticoincidence with the pile-up signal (P) to provide the DET signal. The 1.2.3.$\bar{P}$ pulse was delayed to about 380 ns prior to connection to the DET coincidence. The use of the 1.2.3.$\bar{P}$ in this coincidence was necessary to synchronize the trigger timing to the stop pulse. All ADCs recording NaI signal amplitudes were gated with a 1000 ns long pulse obtained from a fast discriminator connected to one of the SGN coincidence outputs through a 64 ns delay line. All TDCs were started by a pulse taken from the output of the DET coincidence module. The second output of this module provided the strobe signal for the C212 coincidence buffer. The third DET output was fed into a multiple output discriminator. The Ge ADCs were gated using two of these outputs, and one of the outputs was placed in coincidence with the beam-pick-off signal, to obtain the stop pulse for the TDC recording beam RF timing. A simplified picture of typical timing and event definition logic pulses are shown in fig.3-8. This fig. clarifies the basic principles of the logic designs used in the present experiments.

### 3.6. Time and Energy Calibration Procedure

At the beginning of each run, timing and energy electronics were adjusted for optimum time resolution and appropriate energy gain.

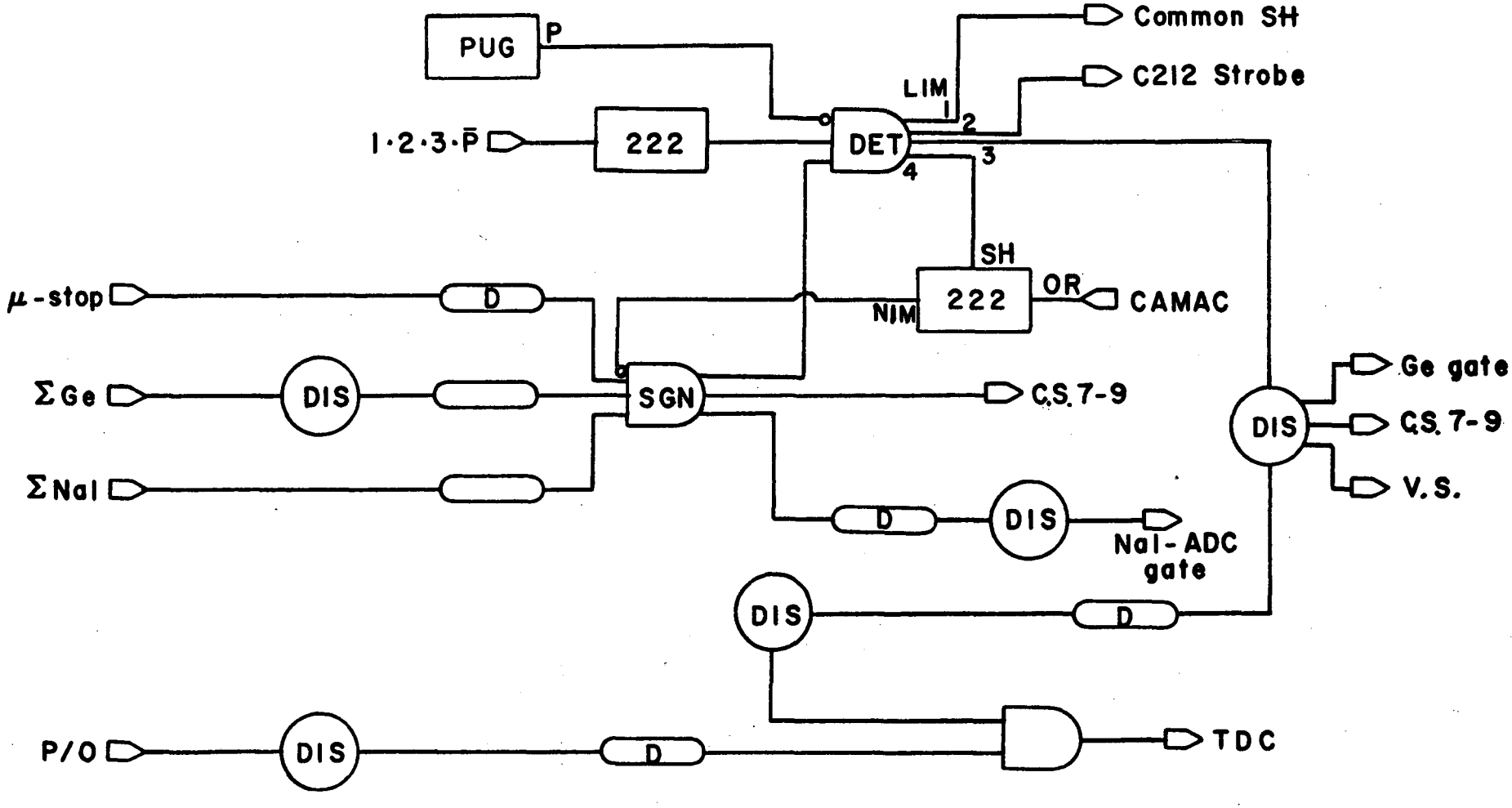


Fig. 3-7 Logic diagram of the electronics used in 1981 run

Adjustment of the timing filter amplifiers' differential time-constants and the constant fraction discriminators' external delay and time walks was performed using a $^{57}Co$ source and the arrangement shown in fig.3-9. NaI detectors are used against each other and the one which gives the best FWHM when used against the others is chosen as the standard. The timing resolution of all other detectors'electronic systems are then optimized as measured against the standard NaI. The timing system of the Ge detectors had a FWHM of about 8 ns. The time scale was calibrated with a Tc-462 time calibrator connected to the start and stop input terminals of TDCs.

Necessary adjustments of the energy system were made to achieve the desired energy gain (kev/chan) by pulse height analysis of the energy spectra of calibration sources. In the 1979 run, $^{60}Co$ and $^{137}Cs$ standard sources were used for energy calibration, in the 1980 and 1981 runs, we used $^{24}Na$ source.

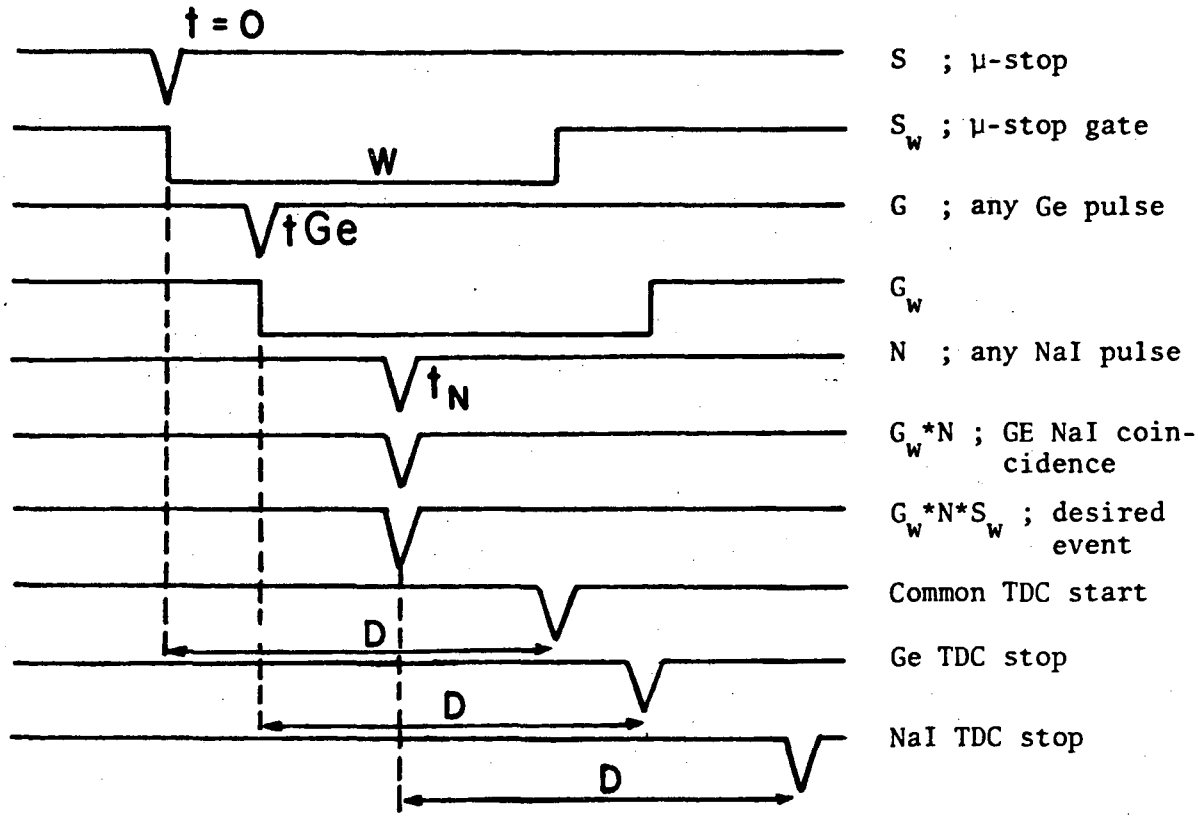


Fig.3-8 Basic timing and event definitions

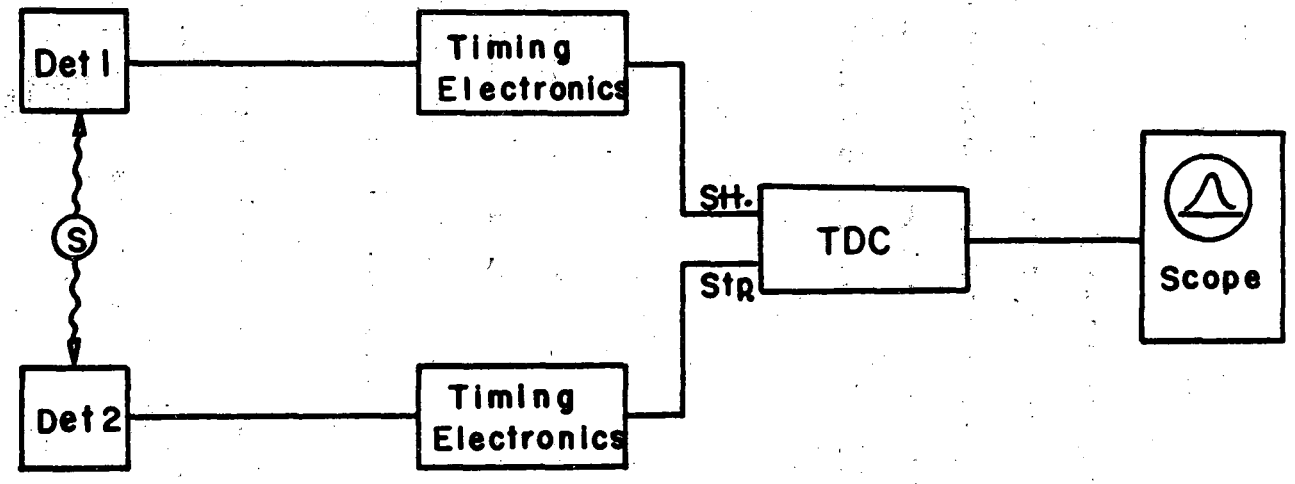


Fig. 3-9 Block-diagram of the arrangement used for adjustment of timing of the electronics

# CHAPTER 4

# DATA ANALYSIS AND RESULTS

## *4.1 Introduction*

The data stored on magnetic tape at the time of the experiment contained information about timing and energy of registered events. This data was histogramed using the pulse-height-analysis (PHA) program in order to generate gamma ray energy spectra with different time windows. The GAMANL (T. Inouye *et al.* 1969) Program was used to perform the peak analysis of the generated energy spectra. The histograming procedure and the peak analysis program will be discussed in sections 2 and 3 of this chapter.

## 4.2. Data Reduction

The event-by-event data was recorded on magnetic tape with a determined record structure. Each record contained a certain number of structural units, so-called "events." An event itself consisted of a group of "words," each carrying a specific piece of information about a physical event such as: event type, C-212 bit pattern identifying the firing detector, and the counts in different ADCs and TDCs.

The reduction stage was carried out by running the PHA program on a PDP11/45 computer. The PHA is an interactive program that reads the data from the tape and selects desired events on the basis of their type and C-212 bit pattern words if they match the specifications of different spectra. The definition of a spectrum could be made more sophisticated by imposing some time and energy "cuts" (constraints on timing and energy range pertaining to the desired events). Channels of an energy histogram space are then filled by incrementing the counts of each channel whenever the ADC counts of a qualified event matches the number of that channel.

The original PHA program used 32-k word space of core extended memory to store histograms. The modules implementing this feature could not be matched with our computer system. In addition, the tape read-write and control subroutines were written in assembly language and could not be used with our system. Therefore new subroutines were written so that histograms could be stored on and worked with on magnetic disk. The FORTRAN listing of the new subroutines are given in Appendix A.

The objective of the reduction stage was to histogram the energies of the Ge-detector gamma rays subject to a condition requiring each of them to be followed by a delayed NaI signal. The delayed Ge gamma spectra fulfilling this condition should show the back-decay gamma transitions which are followed by muon nuclear capture gamma rays, if they are populated at the sensitivity of our detection system. Considering the capture life time of around 80 nsec, the following condition was set

$$t_{Na} - t_{Ge} \geq 20 \text{ Nsec} \qquad (4\text{-}1)$$

where $t_{Na}$ and $t_{Ge}$ are the recorded times after the muon stop of the NaI and Ge detectors signals respectively. In order to reduce background arising from unwanted and/or accidental coincidences, it was later decided to set an upper bound of 120 nsec for the above relation. To facilitate future reference to these two cases, we call the first group of spectra produced earlier and without any upper bound "group-1" and refer to the latter as "group-2" spectra. The "group-1" contained prompt and delayed spectra with 5 nsec time windows covering a range of Ge time after muon stop of -2.5 nsec to 27.5 nsec. This group was generated for the search of back-decay transitions, assuming a 12 nsec life time (reported by Fromm *et al.* 1978) for the muonic $^{238}U$. The "group-2" spectra had wider time windows to suit the search for gamma rays with lifetimes ranging from 20 to 50 nsec.

### 4.3. Peak Analysis Program

The computer code GAMANL (T. Inouye *et al.* 1969) used for peak analysis of the spectra generated by PHA, automatically identifies the peaks of the complex Ge-spectra and determines their centers and areas. The principal feature of the method used in this program is a data smoothing technique employing Fourier transform. The transformation is from the energy space into inverse channel number space. The observed spectral data f(E) is in fact a function of energy, consisting of two components: the true spectral information; and the noise, which in this case is due principally to random fluctuations in the number of counts in a channel ($f(E) = S(E) + n(E)$). The noise component is removed by multiplying the Fourier transform of the data $F(\omega)$ by an appropriate filter function $P(\omega)$ and taking the inverse transform of the product.

In order to be able to accurately determine the peak centers and areas, the background should be subtracted from the smoothed data. The background is represented as a slowly varying function which connects all the minima in the smoothed data. In order to avoid minima resulting from partially resolved peaks, a maximum value for the slope of the connecting line is specified. We found that the code is not very sensitive to the slope parameter and values from 0.2 to 0.4 can be used. The peak selection is then accomplished by identifying each maximum in the smoothed background subtracted data. The peak center is obtained by finding the point of zero slope of a second order fit to the top of the peak. Writers of the code have checked the accuracy of this procedure by comparing the results for a number of peaks to those obtained by finding the centroid of a Gaussian fitted to the peak using a least squares method. The results are claimed to agree within $\pm 0.1$ channels on peaks with $\sigma = 1.5$ channels.

The areas of spectral peaks are determined by adding up all the counts between successive zeros in the smoothed background subtracted data. Cases of doublets and triplets were treated separately. For peaks with a small hump in their tails, the areas were determined from a Gaussian model. The areas of the Gaussians were calculated using an energy-dependent $\sigma$ as a function of energy. Where energy dependence was determined by fitting strong isolated peaks in the

spectrum.

In the application of the code we found that a careful selection of the filter function used in the smoothing of the data was essential. This filter function is usually a step function which falls off with a Gaussian shape. It passes frequencies below the break in the curve and eliminates those frequencies above the break where the noise component dominates. The break or so called cut-off frequency of the filter was determined by plotting the Fourier transform function $|F(\omega)|$ vs. $\omega$ (radian/chan) (see Fig. 4-1), and trying to approximate the shape of the components $N(\omega)$ and $S(\omega)$ of the Fourier transform function $F(\omega)$. The break point in this case is about 400 units of $\omega$.

### 4.4. System Efficiency

In the present work we are not interested in the absolute yield of gamma rays, but instead we will be dealing with the yield per muon stop of the individual gamma rays. This automatically eliminates the need for consideration of geometrical efficiency, because it will be canceled out from the expression of the $Y_{pms}$ (yield per muon stop). The yield $Y_{pms}(E)$ for a spectral peak at energy $E_\gamma$ observed in a time gate $(t_1 \rightarrow t_2)$ can be given as

$$Y_{pms}(E) = \frac{A(E_\gamma)}{\epsilon(E_\gamma).N_{\mu-stop}.W} \qquad (4\text{-}2)$$

where W is the gate width correction, $A(E_\gamma)$ gives the area under the peak, $(E_\gamma)$ is the detection efficiency at energy $E_\gamma$ and $N_{\mu-stop}$ represents the number of muons stopped in the target. The expression for the gate width correction W is

$$W = \int_{t_1}^{t_2} e^{-\lambda_m t} dt \qquad (4\text{-}3)$$

where

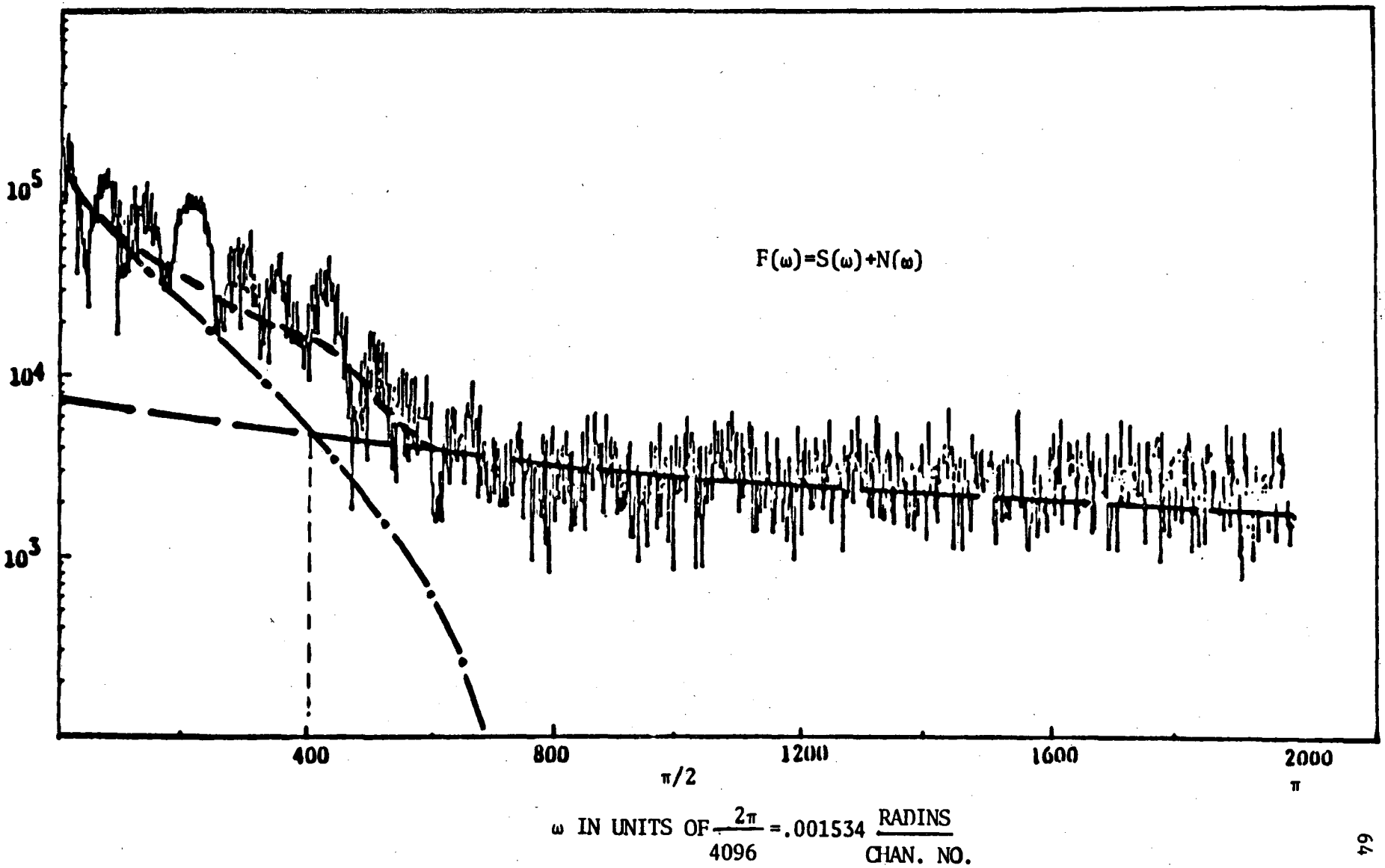




Fig. 4-1 Fourier trnsform of the raw data used to find the cut-off frequency

$\lambda_m$ = total muon disappearance rate in the target

$t_1$ = time after muon stop when the gate opens

$t_2$ = time after muon stop when the gate closes.

Since each muon stop is followed by a series of cascading x rays, the number of muon stops in the target can be correlated to the total number of transitions of a particular x-ray line by a "cascade correction factor". The selected transition should be between some higher circular orbits like 4f-3d transition, such that it does not include any non-radiative component. Hence the $N_{mu-stop}$ can be expressed as

$$N_{\mu-stop} = \frac{A(E_x)}{\epsilon(E_x).P_x} \tag{4-4}$$

where

$E_x$ = energy of the selected x-ray line

$A(E_x)$ = the measured total counts of the selected x-ray line

$\epsilon(E_x)$ = detection efficiency at $E_x$

$P_x$ = the cascade correction factor.

The cascade correction factor $P_x$ for each set of data was found by first calculating the intensity of the 4f-3d transitions (M x-rays) of a muonic uranium atom and then multiplying it by the relative intensity of the selected line among all M x-rays. The values calculated from different data sets were consistent and approximately equal to $P_x = 0.16$ . Incorporating the equation (4-4) into the expression (4-2) we find

$$Y_{pms}(E) = \frac{A(E_\gamma)}{A(E_x)} \cdot \frac{\epsilon(E_x)}{\epsilon(E_\gamma)} . P_x . W^{-1} \tag{4-5}$$

The ratio $\frac{(E_x)}{(E_\gamma)}$ is in fact the ratio of absolute efficiencies of the Ge detector at energies $E_x$ and $E_\gamma$. For the range of energies that we are interested in, namely $E_\gamma > 1$ Mev, the absolute

efficiency of the Ge detector as a function of gamma ray energy can be very closely approximated with a straight line in a log-log scale (Temple E., 1972).

$$(\log \epsilon) = \alpha\,(\log E) + \beta \tag{4-6}$$

which results in

$$\epsilon(E_1)/\epsilon(E_2) = (E_1/E_2)^{\alpha} \tag{4-7}$$

which indicates that only $\alpha$ the slope of the straight line is needed for our purpose. The value of $\alpha$ was calculated using the relation (4-7) and our measured intensities of the two lines of $^{24}Na$ calibration source. The energies of the two lines of $^{24}Na$ are: 1368.5 kev and 2754.1 kev which closely spans the energy range of our interest. Some quantitative results of the yield calculation for different sets of our data, as well as plots of $Y_{pm}$ vs. E for different time windows will be given in chapter 5.

### 4.5. Calibration Spectra

The energies and half lives of the standard sources used for energy calibration of our different gamma ray spectra are given in table IV-1.

Table IV-1

| Standard Source | Energy (kev) | Half life |
|---|---|---|
| $^{60}Co$ | 1173.23 ± .04<br>1332.49 ± .04 | 5.26y |
| $^{24}Na$ | 1368.526 ± .044<br>2753.92 ± .120 | 15.0h |

(From: Lederer and Shirley, 1978)

The $^{16}O^{*}$ source was used only for the 1981 experiment in which the gain was set to about 1 kev/chan, so that the measurement of the muonic $^{236}U$ k-x rays could be accomplished in 8 k channel spectra. Unfortunately the high energy lines of $^{16}O^{*}$ source were missing in the histogramed calibration data; as a result, another method was found to somehow include high energy points in the calibration curve parameterization. Apparently the only way was to try to recognize the single and double escape peaks (SEP, DEP) of the K and L muonic x rays and use the well-known energy differences between them and their respective full-energy peaks to extend the calibration into the high energy region. The energies of the $^{60}Co$ and $^{24}Na$ lines along with their single and double escape peaks and the $e^{+}$—$e^{-}$ (511. kev) were fitted into a 3th order polynomial of the form

$$E = ax^3 + bx^2 + cx + d \tag{4-8}$$

where x stands for channel number attributed to the energy E. The energy differences of the x-ray lines and their SEP and DEP were fitted to the equation

$$\Delta E = a(x^3 - x'^3) + b(x^2 - x'^2) + c(x - x') \tag{4-9}$$

where x and x' were channel numbers attributed to the full-energy peaks and their escape peaks respectively. The least squares fit method was set up in a special form to facilitate dealing with two different sets of points and their associated fitting functions simultaneously. Some more details of the method as well as the FORTRAN listing of the program that carried out the method are provided in Appendix B.

The values of the parameters a, b, c and d of the fitted polynomials are given in Table IV-2.

For the 1979 run no independent calibration spectra were taken. The measured values of the L, M, and N lines of the muonic $^{238}U$ x rays reported by Cote *et al.* (1969) were used for energy calibration. A typical calibration energy spectrum taken in a later run is shown in Fig.

4-2. The $^{24}$Na lines and their escape peaks as well as some background gamma rays are marked. The background gamma rays were identified as originating from the interactions of neutrons and gamma rays with the ever-present lead (Pb) shieldings in the experimental area.

Table IV-2

| Parameters | Values | |
|---|---|---|
| | 1980 data | 1981 data |
| a | $-.1512\times10^{-8}$ | $-.3421\times10^{-9}$ |
| b | $.7949\times10^{-5}$ | $.2435\times10^{-5}$ |
| c | $.1151\times10^{1}$ | $.1113\times10^{1}$ |
| d | $-.1049\times10^{3}$ | $-.3181\times10^{2}$ |

### 4.6. Prompt Spectra

The prompt spectra of gamma rays resulting from muon stopping in uranium isotopes were carefully investigated. The peak analysis is basically performed by the GAMANL program. Only some very small peaks not located by the program were hand analyzed and their centers were determined directly from the raw data and their energies were calculated using the pertinent calibration polynomial.

For all three cases of uranium isotopes the prompt spectra exhibited the features of muon interaction with a deformed heavy nucleus. Prompt spectra of the 1979 and 1980 muonic mesonic $^{238}$U data are shown in Figs. 4-3 and 4-4 respectively. From these figures it appears that the muonic transitions or their related single escape and double escape peaks are forming these prompt spectra, and no other gamma rays are observed. Our measured energies and relative intensities from the major group of the L, M and N x-rays of the muonic $^{238}$U are given in Table IV-3. Three other sets of experimental results as well as a set of calculated values are

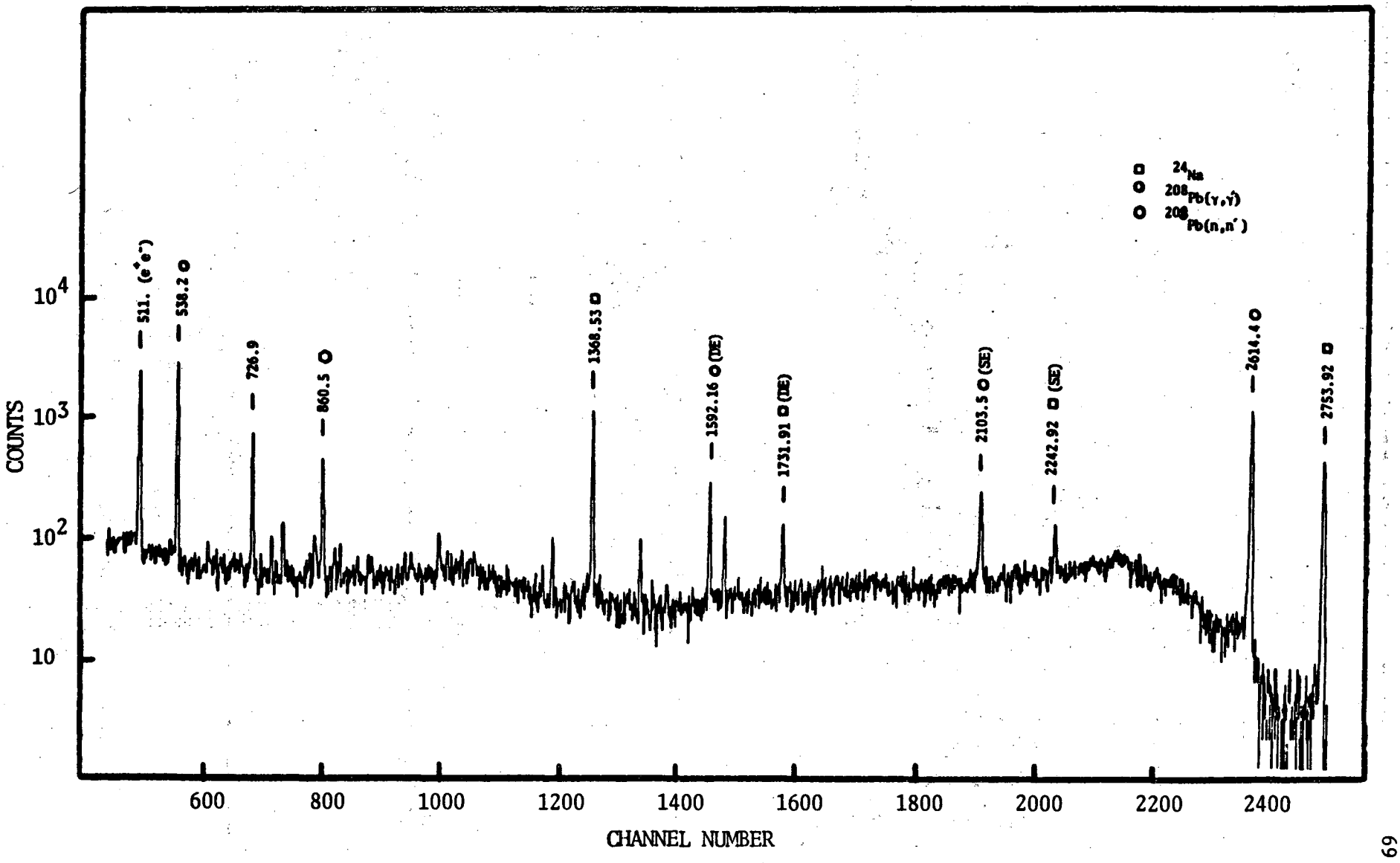


Fig. 4-2 Ge2 calibration spectra ($\mu$-$^{236}$U run, 1981)

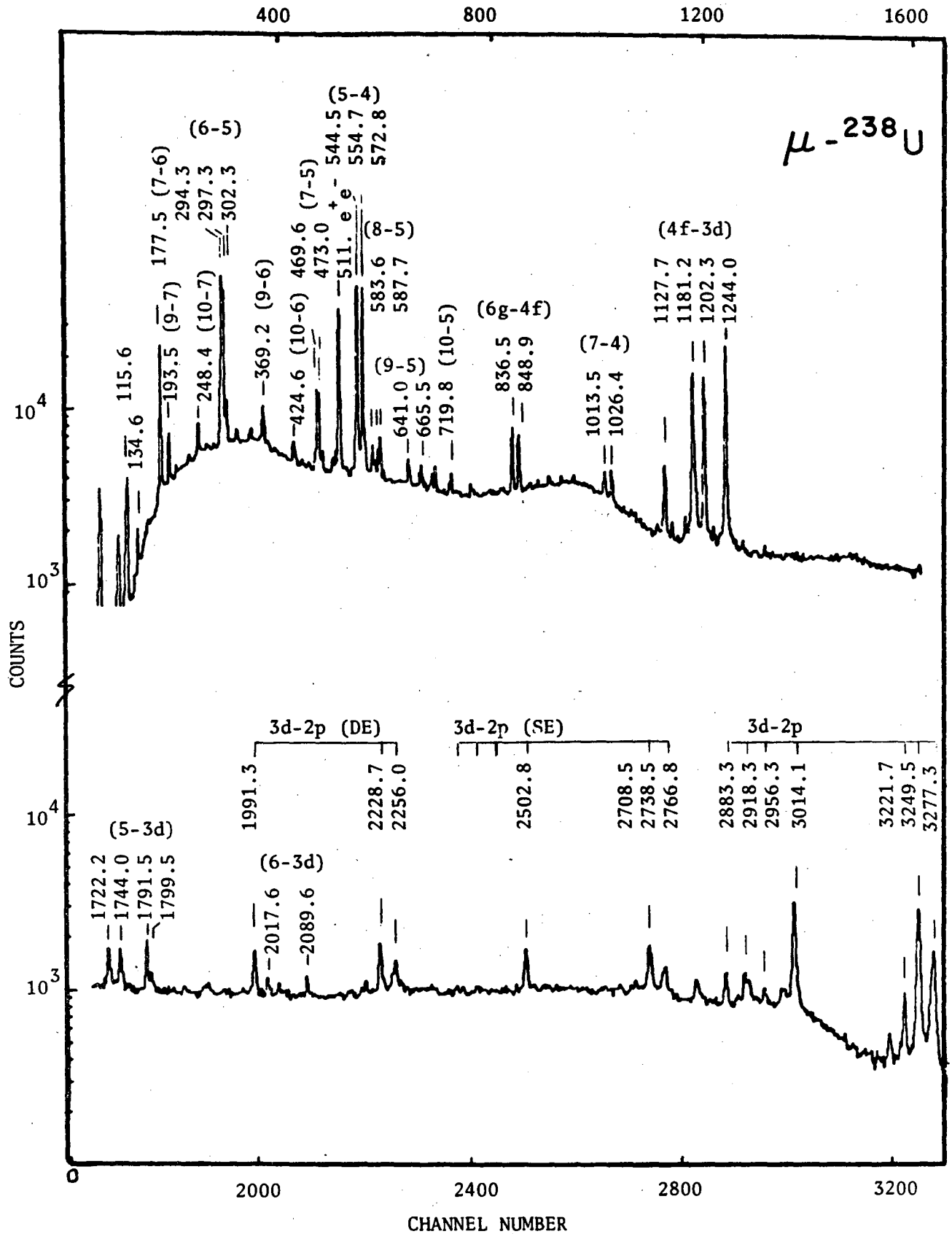


Fig. 4-3 Prompt spectrum of μ-$^{238}$U (1979 run)

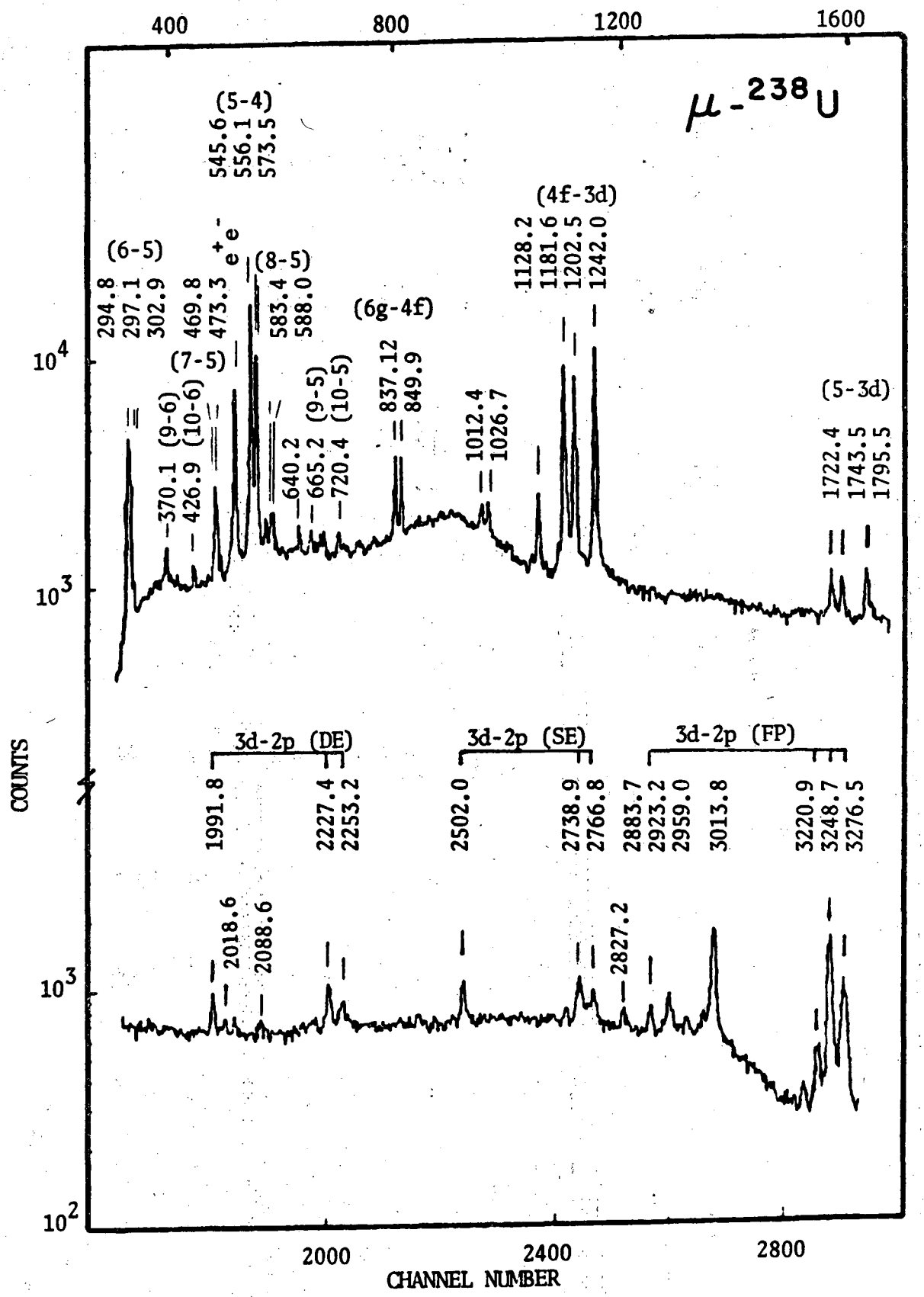


Fig. 4-4 Prompt spectrum of $\mu^{-238}U$ (1980 run)

Table IV-3 MUONIC $^{238}U$ X-RAYS

| Transitions | exp. (1980) | | exp. (1979) | | exp. (1978)[a] | | calc. (1978)[a] | | exp. (1976)[b] | exp. (1969)[c] |
|---|---|---|---|---|---|---|---|---|---|---|
| | Energy (keV) | Rel. Int. | Energy (keV) | Rel. Int. | Energy (keV) | Rel. Int. | Energy (keV) | Rel. Int. | Energy (keV) | Energy (keV) |
| 3d-2p | -- | -- | -- | -- | 2826.6 | .021 | 2826.4 | .020 | -- | -- |
| | 2883.7 | .054 | 2883.3 | .049 | 2882.8 | .044 | 2883.0 | .036 | 2883.6 | -- |
| | 2923.2 | .073 | 2918.3 | .050 | 2919.5 | .046 | 2919.2 | .031 | 2917.3 | -- |
| | -- | -- | -- | -- | 2927.1 | .030 | 2927.2 | .023 | -- | -- |
| | 2959.0 | .018 | 2956.3 | .011 | 2956.9 | .018 | 2957.3 | .016 | 2956.9 | -- |
| | -- | -- | -- | -- | 2994.8 | .023 | -- | -- | -- | -- |
| | 3013.8 | .272 | 3014.1 | .289 | 3013.0 | .286 | 3012.8 | .201 | 3013.4 | 3012.8 |
| | -- | -- | -- | -- | 3191.5 | .021 | 3192.3 | .013 | -- | -- |
| | 3220.9 | .049 | 3221.7 | .059 | 3221.9 | .039 | 3222.0 | .062 | 3221.8 | 3220.8 |
| | 3248.7 | .328 | 3249.5 | .328 | 3249.1 | .306 | 3248.8 | .274 | 3249.3 | 3249.7 |
| | -- | -- | -- | -- | -- | -- | 3252.2 | .046 | -- | -- |
| | -- | -- | -- | -- | -- | -- | 3273.2 | .055 | -- | 3272.6 |
| | 3276.5 | .206 | 3277.3 | .213 | 3277.4 | .166 | 3278.6 | .121 | 3277.8 | 3279.7 |
| | -- | -- | -- | -- | -- | -- | 3281.3 | .015 | -- | -- |
| 4f-3d | 1128.2 | .052 | 1127.7 | .060 | 1127.9 | .053 | 1127.3 | .031 | 1128.9 | -- |
| | 1181.6 | .301 | 1181.2 | .337 | 1181.1 | .319 | 1180.7 | .274 | 1181.1 | 1181.1 |
| | -- | -- | -- | -- | -- | -- | 1184.2 | .030 | -- | -- |
| | -- | -- | -- | -- | -- | -- | 1186.9 | .015 | -- | -- |
| | 1202.5 | .240 | 1202.3 | .243 | 1202.3 | .245 | 1201.6 | .245 | 1202.8 | 1202.3 |
| | 1242.0 | .407 | 1244.0 | .360 | 1243.9 | .382 | 1243.5 | .381 | 1244.5 | 1244.0 |
| 5g-4f | -- | -- | -- | -- | -- | -- | 540.2 | .015 | -- | -- |
| | 545.6 | .563 | 544.5 | .553 | 544.4 | .549 | 544.6 | .548 | 544.5 | 544.6 |
| | 556.1 | .437 | 554.7 | .447 | 554.7 | .451 | 554.9 | .432 | 554.6 | 554.5 |

a) Close et al. 1978

b) Fromm et al. 1976

c) Cote et al. 1969

Table IV-4 MUONIC URANIUM K X-RAYS (2P-1S)

| $^{236}U$ a | | $^{238}U$ b | | $^{238}U$ c | | $^{235}U$ c | |
|---|---|---|---|---|---|---|---|
| Energy kev. | Rel. Int. | Energy kev. | Rel. Int. | Energy kev. | Rel. Int. | Energy kev. | Rel. Int. |
| — | — | — | — | 6047.4 | .024 | 6112.4 | .009 |
| 6118.9 | .064 | 6093.5 | .066 | 6096.6 | .056 | 6119.9 | .020 |
| 6144.9 | .207 | 6119.2 | .187 | 6121.1 | .163 | 6150.1 | .035 |
| 6154.9 | .271 | 6136.5 | .198 | 6140.5 | .220 | 6158.1 | .078 |
| — | — | 6145.0 | .138 | 6149.0 | .089 | 6165.2 | .211 |
| — | — | 6162.1 | .035 | 6167.4 | .031 | 6169.8 | .118 |
| — | — | — | — | 6379.3 | .015 | 6205.8 | .029 |
| 6426.8 | .154 | 6407.3 | .124 | 6409.4 | .112 | 6397.9 | .023 |
| — | — | — | — | 6416.5 | .029 | 6414.6 | .048 |
| 6470.9 | .160 | 6451.0 | .118 | 6454.1 | .113 | 6453.1 | .042 |
| — | — | 6476.8 | .021 | 6462.6 | .021 | 6460.4 | .215 |
| 6501.1 | .048 | — | — | 6480.9 | .033 | 6501.6 | .033 |
| 6533.2 | .069 | 6514.3 | .068 | 6518.4 | .064 | 6544.3 | .024 |
| 6581.2 | .026 | 6561.1 | .045 | 6563.7 | .032 | 6757.4 | .098 |
| — | — | — | — | — | — | 6587.4 | .018 |

a) This experiment

b) Cote et al. 1968

c) Close et al. 1978

also listed in that table. The 1979 x-ray energies should not be counted on as an independent result, because that data was calibrated using the experimental results of Cote *et al.* (1969).

The $^{236}U$ data covered an energy range of up to ≈8 Mev in 8192 channels. Due to limitations of GAMANL, not more than 4096 channel could be analyzed at a time. So, for the analysis of K x rays, the channel pairs were summed. But for investigation of lower energy transition only the first 4096 channels were analyzed in order to preserve the measured energy resolution of about 1 kev/ch. The muonic $^{236}U$ x-ray data are shown in Figs. 4-5 and 4-6. There is no report of any experimental or calculated values for $^{236}U$ muonic x-ray in the literature.

Our K x-ray energies and relative intensities are shown along with the $^{238}U$ and $^{235}U$ results of Close *et al.* (1978) and the $^{238}U$ results of Cote *et al.* (1969) in Table IV-4. An isotope shift of around 20 KeV for the K x-ray lines of the two even-even isotopes ( $^{236}U$ and $^{238}U$) is observed. Both $^{236}U$ and $^{238}U$ are even-even nuclei showing almost the same deformations and have very similar ground state rotational bands and wave functions; but, in contrast, the $^{235}U$ is an odd-even nucleus showing completely different nuclear level structure which results in a change of hyperfine splitting of the levels. The $^{235}U$ spectrum bears little detailed relationship two the other two.

The prompt spectrum of muonic $^{235}U$ is shown in Fig. 4-7, and the experimental energies and relative intensities of the principle low-energy x-ray lines of all three isotopes are listed in Table IV-5. Isotope shifts for the muonic transitions at these lower x-ray energies shown are, as expected, not noticeable in the case of heavy nuclei. In addition to the groups of x-ray lines which correspond to those of the $^{236}U$ and $^{238}U$ muonic atoms, there are three rather strong isolated peaks in the prompt spectrum of muonic $^{235}U$, as seen in Fig. 4-7. The energies and relative intensities of these lines are given in Table IV-6. The energies of the first two lines, 333.7 and 1511.6 kev, are within experimental error equal to the measured values of L and K muonic x-ray transition energies in $^{nat}Cu$ (Engfer *et al.* 1974). The copper x-rays were presumably

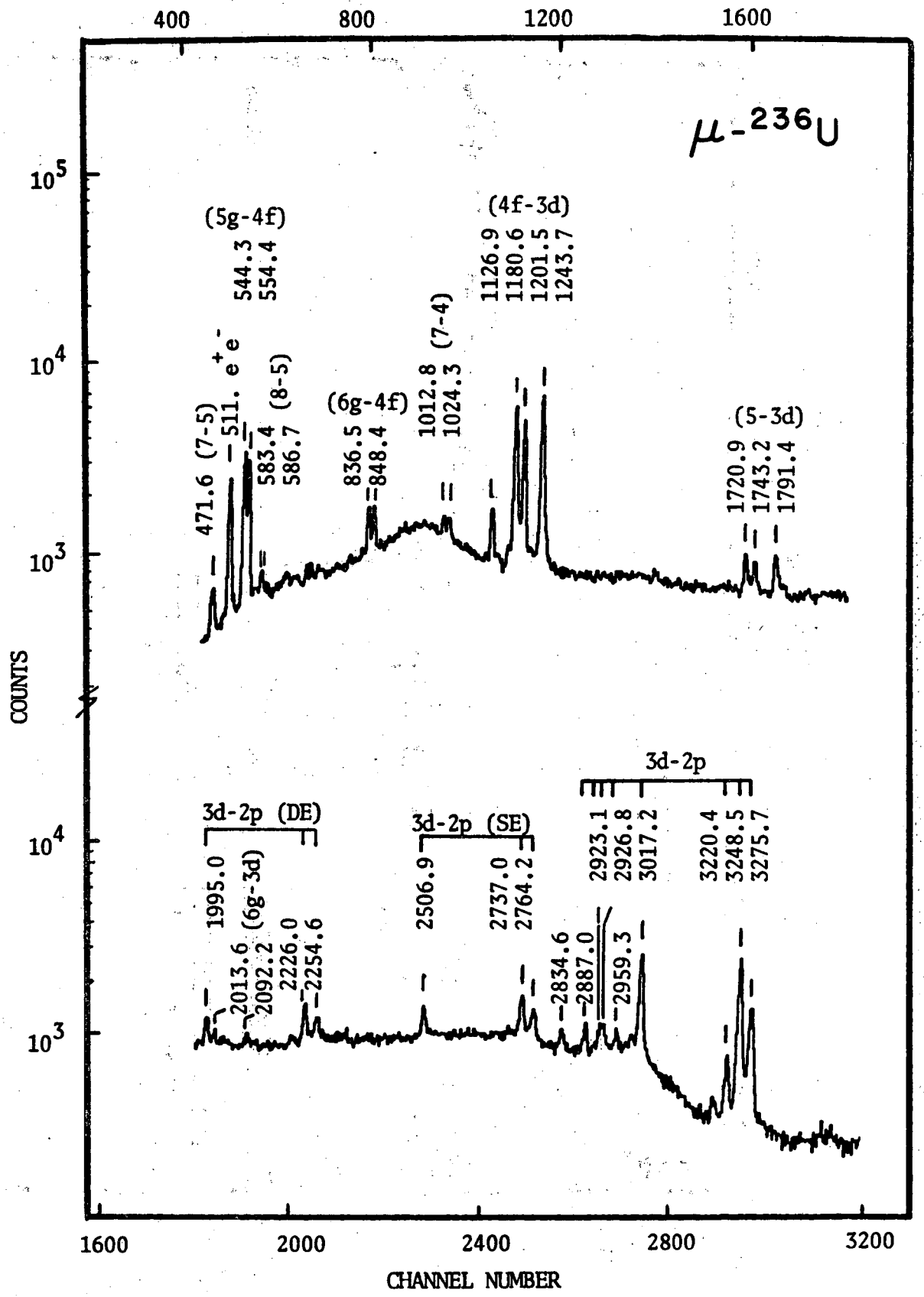


Fig. 4-5 Prompt spectrum of μ-$^{236}$U (1981 run )

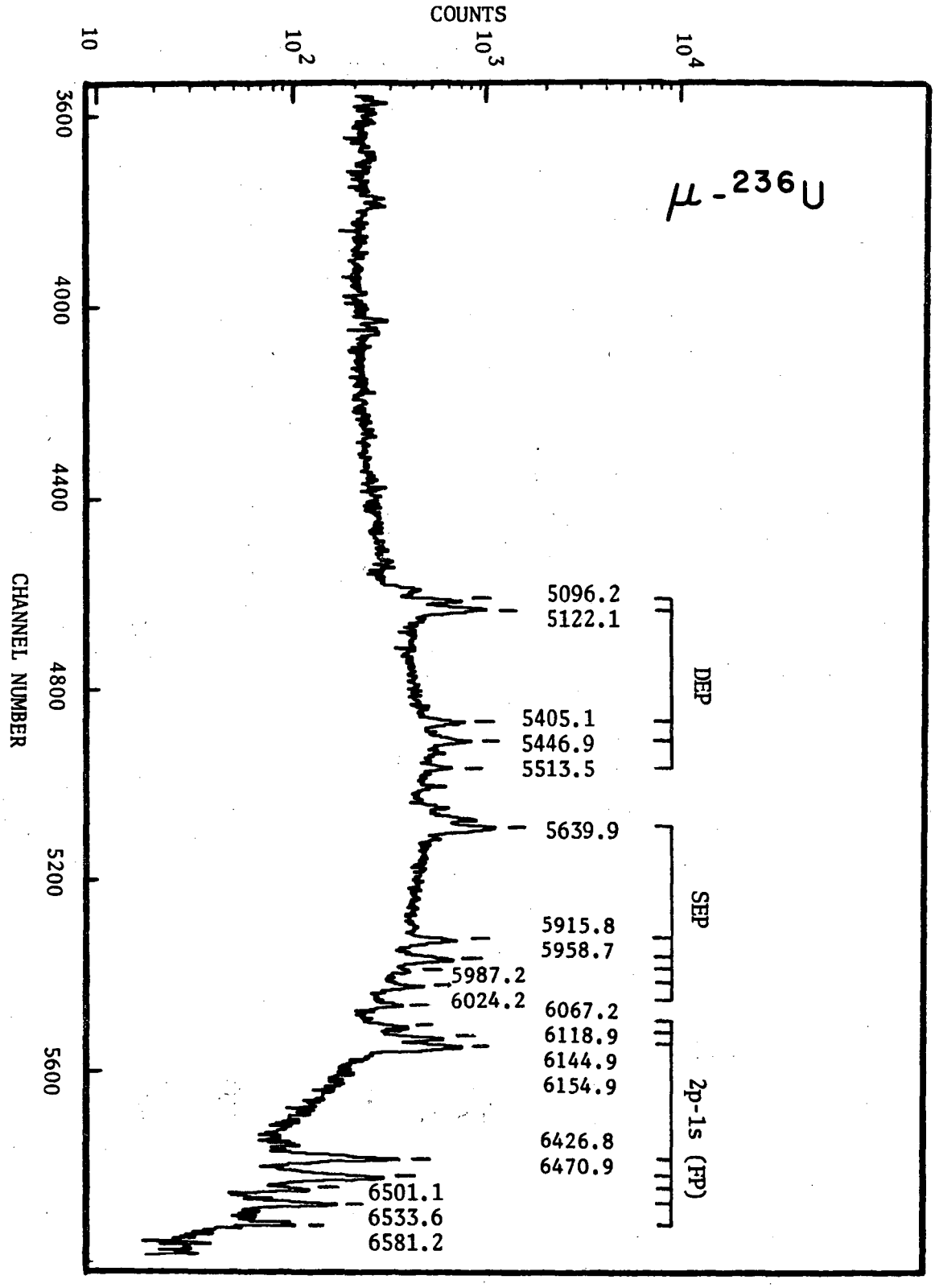


Fig. 4-6 Muonic $^{236}U$ K x-rays and their single and double escape peaks

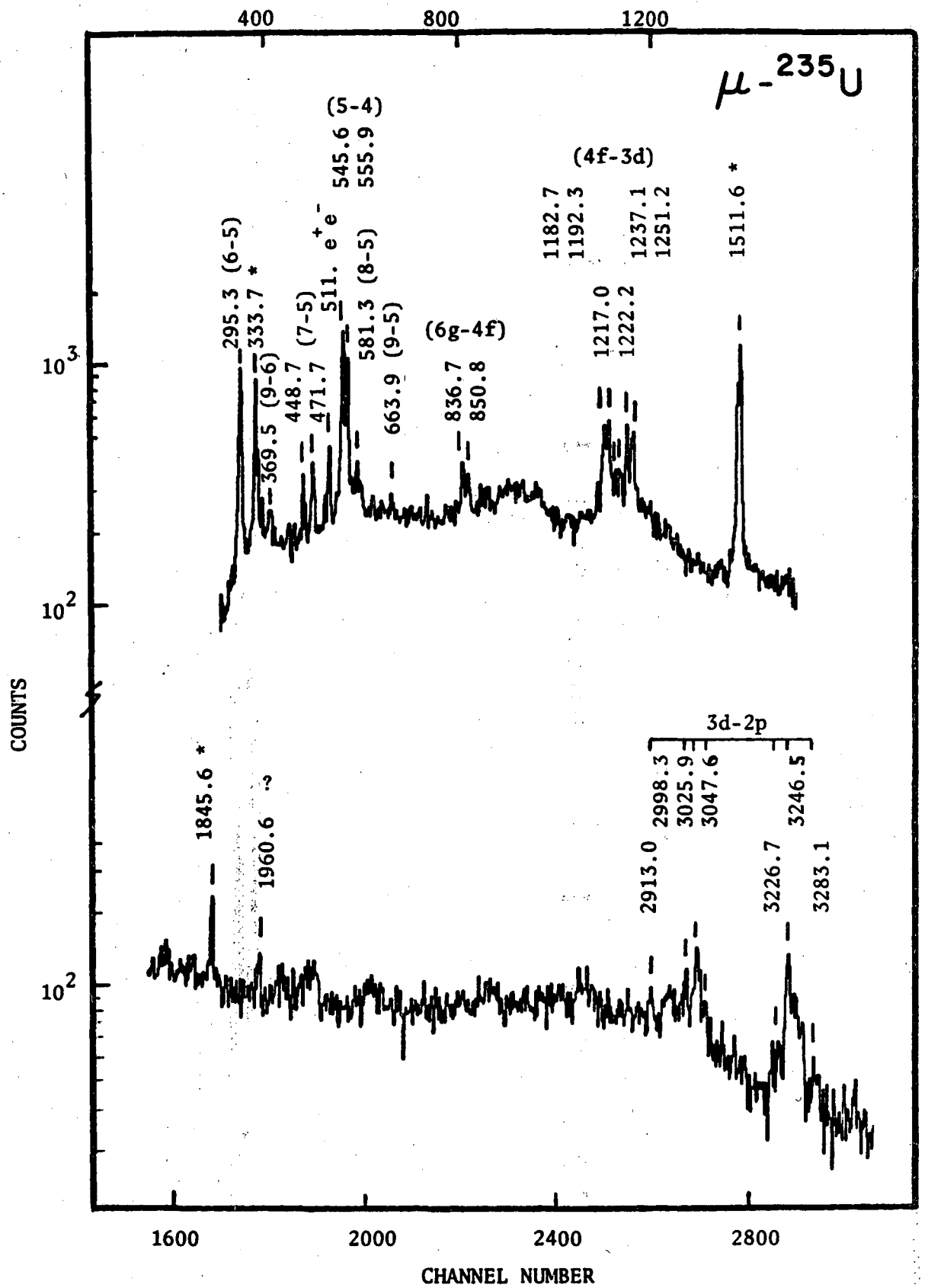


Fig. 4-7 Prompt spectrum of μ-$^{235}$U (1980 run)

Table IV-5 COMPARISON OF MUONIC X-RAYS OF URANIUM ISOTOPES

| Transitions | $^{238}U$ [a] | | $^{236}U$ [a] | | $^{235}U$ [a] | | $^{235}U$ [b] | |
|---|---|---|---|---|---|---|---|---|
| | Energy (keV) | Rel. Int. | Energy (keV) | Rel. Int. | Energy (keV) | Rel. Int. | Energy (keV) | Rel. Int. |
| 3d-2p | 2883.7 | .054 | 2887.0 | .043 | -- | -- | -- | -- |
| | 2923.2 | .073 | 2923.1 | .048 | 2913.0 | .108 | 2910.8 | .022 |
| | -- | -- | 2926.8 | .012 | -- | -- | 2946.5 | .036 |
| | 2959.0 | .018 | 2959.3 | .023 | -- | -- | 2959.5 | .044 |
| | -- | -- | -- | -- | -- | -- | 2984.9 | .028 |
| | -- | -- | -- | -- | 2998.3 | .142 | 2997.4 | .062 |
| | 3014.2 | .272 | 3017.2 | .288 | -- | -- | 3016.5 | .022 |
| | -- | -- | -- | -- | 3025.9 | .327 | 3023.5 | .171 |
| | -- | -- | -- | -- | -- | -- | 3032.2 | .051 |
| | -- | -- | -- | -- | 3047.6 | .053 | 3043.7 | .041 |
| | -- | -- | -- | -- | -- | -- | 3211.4 | .018 |
| | 3220.9 | .049 | 3220.4 | .052 | 3226.7 | .051 | 3224.9 | .022 |
| | -- | -- | -- | -- | -- | -- | 3242.1 | .096 |
| | 3248.7 | .328 | 3248.5 | .359 | 3246.5 | .264 | 3246.7 | .124 |
| | -- | -- | -- | -- | -- | -- | 3252.6 | .070 |
| | -- | -- | -- | -- | -- | -- | 3260.5 | .090 |
| | -- | -- | -- | -- | -- | -- | 3267.6 | .035 |
| | 3276.5 | .206 | 3275.7 | .175 | 3283.1 | .055 | 3281.2 | .050 |
| | | | | | -- | -- | 3317.9 | .015 |
| 4f-3d | 1128.2 | .052 | 1126.9 | .048 | -- | -- | -- | -- |
| | 1181.6 | .301 | 1180.9 | .318 | 1182.7 | .241 | 1181.2 | .241 |
| | 1202.5 | .240 | 1201.5 | .245 | 1192.3 | .238 | 1191.6 | .270 |
| | 1242.0 | .407 | 1243.7 | .389 | 1221.2 | .062 | 1219.4 | .069 |
| | | | | | 1237.1 | .202 | 1236.3 | .155 |
| | | | | | 1251.2 | .258 | 1250.8 | .265 |
| 5g-4f | 545.1 | .563 | 544.3 | .535 | 545.6 | .546 | 544.7 | .557 |
| | 556.1 | .437 | 554.4 | .465 | 555.9 | .454 | 555.1 | .443 |

a) This experiment.
b) Close et al. 1978.

due to the interaction of the muons deflecting from the beam and interacting with a small amount of copper that was in the target assembly (we first looked for, and discovered the presence of the Cu in the assembly as a result of the observation of the mysterious lines). The peak at 1845.6 kev is obviously the summation of the above two x-ray transitions or the $K_\beta$ x-ray. The 1960.6 kev gamma ray which has the lowest intensity among the lines listed in table IV-6 could not be identified from references but has an energy consistent with the value we would expect from the muonic $K_\gamma$ x-ray of Cu.

Table IV-6

| Energies (kev) | 333.7 | 1511.6 | 1845.6 | 1960.6 |
|---|---|---|---|---|
| Rel.Int.* | 1.59 | 4.66 | .344 | .166 |

* compared with the 1182. kev line of the U235 M x-ray

**4.7. Delayed Spectra**

The delayed gamma-ray activity following the radiationless transition in the muonic cascade may result from processes such as, nuclear muon capture, deexcitation of spin isomers excited in fragments produced by prompt fission or in the target nucleus, and the decay of the shape isomeric state populated by the radiationless muonic transition. The search for the gamma branch of the last decay process is the main interest in the present investigation. A muon can be captured by the ground state in the first well or by the shape isomeric state of the target nucleus. It may also be captured by one of the fragments produced in fission. In addition to gamma transitions directly following nuclear muon capture, gamma rays may be emitted by capture of neutrons emitted in the $\mu^-$-capture process or by inelastic scattering of these neutrons. Among the mentioned delayed gamma rays only the back-decay from the shape isomeric state is always followed by other gamma rays, thus fulfilling the requirement made in the data acquisition and reduction stages. The contribution of other gamma rays is expected to be from their delayed coincidence with background and therefore not that significant. If the observed

lines are due to coincidences with a time-dependent background they would not be seen with their real lifetimes. The experimental lifetime $\tau_e$ is related to the real lifetime $\tau_1$ and the life time of the background ($\tau_2$) by the following relation

$$\frac{1}{\tau_e} = \frac{1}{\tau_1} + \frac{1}{\tau_2} \tag{4-10}$$

Meaning that the experimental lifetime is always smaller than or equal to the real one. This effect is discussed in more detail in appendix C.

As mentioned before, for both $^{238}U$ and $^{236}U$, two sets of spectra with the features of "group 1" and "group 2"--described before--were generated. The investigation of the delayed spectra was carried out by two procedures. For the preliminary search the GAMANL program was used for the full analysis of the delayed spectra. The energies of the gamma rays found in successive time windows were compared. In the analysis of the "group 2" spectra, three peaks at energies of about 708, 817 and 1015 kev respectively were found in three different time windows. For "group 1" spectra, only one peak at the energy of 2693 kev showed up, and only in two distinct time windows. A technique was developed to measure the detection sensitivity of individual time windows. The discussion of this technique and its detailed results are the topic of the next chapter. Different combinations of successive 5-nsec-wide windows of the "group 1" spectra were summed to produce new delayed time windows covering different time ranges, and their respective detection sensitivities were found. Even the most sensitive time window did not reveal any of the peaks reported by a CERN group (Fromm *et al.* 1976) to be observed at 3131 kev and 2215 kev. A full analysis of the detection sensitivity as a function of energy and confidence level will be discussed in chapter 5. After the failure of this method to detect any candidate for the gamma branch of the shape isomeric state deexcitation, a second more elaborate procedure was tried. This time the GAMANL program was utilized only for the purpose of smoothing the spectra by filtering out the random noise and subtracting the background. The peak analysis part was not used. For both "group 1" and "group 2" sets of spectra, the

smoothed background subtracted data and the background were printed out. Also, different frames of plots showing the counts in the four or five successive time windows of the smoothed background subtracted data corresponding to the same channel number range were produced. The plots were carefully examined by eye over the entire energy range of up to 4 Mev. Any apparent occurrence of peaks in at least three independent time windows was attributed to a delayed gamma line if the area of each peak was greater than twice the statistical fluctuation of its underlying background. In case of doublets, a hand analysis was used to find the area under each peak from the printout. Applying this analysis method to the "group 1" spectra only helped to find a third time window in which the 2693 kev line was observable and no other peak was found to meet the required conditions for being attributed to a real delayed transition. The "group 2" spectra with delayed time windows of 10 to 20 nsec, 20 to 35 nsec, 35 to 55 nsec, 55 to 90 nsec and 90 to 180 nsec after Ge prompt time showed the existence of a few delayed gamma rays. The appearance of the observed lines in different time windows are shown in Figs. 4-8 and 4-9. A preliminary least-squares fit of the decay characteristics of the individual lines showed different lifetimes which could be divided into two groups. The lines of the first group could be fitted by a common lifetime of about 75 nsec, which is typical of $\mu^-$-capture connected processes in uranium nuclei. The energies of three of these lines, namely the 685, 817 and 1015 kev are in good agreement with the transitions observed in $^{238}U(n,\gamma)$ reaction (L.V. Grosher *et al.* 1969) and $^{238}U$ $(n,n'\gamma)$ reactions ( Mc Murray *et al.* 1972). The energies and intensities of these lines are presented in table IV-7. Figs. 4-10-a and 4-10-b show the decay curves for these transitions. The second group can be fitted to a common lifetime of about 28 nsec. None of the observed lines are compatible with the level scheme of $\mu^-$—$^{238}U$ proposed by Fromm *et al.* (1976). Even with considering the possible transitions from their proposed shape isomeric level to some other levels of the various rotational or $\gamma$-vibrational band in $^{238}U$.

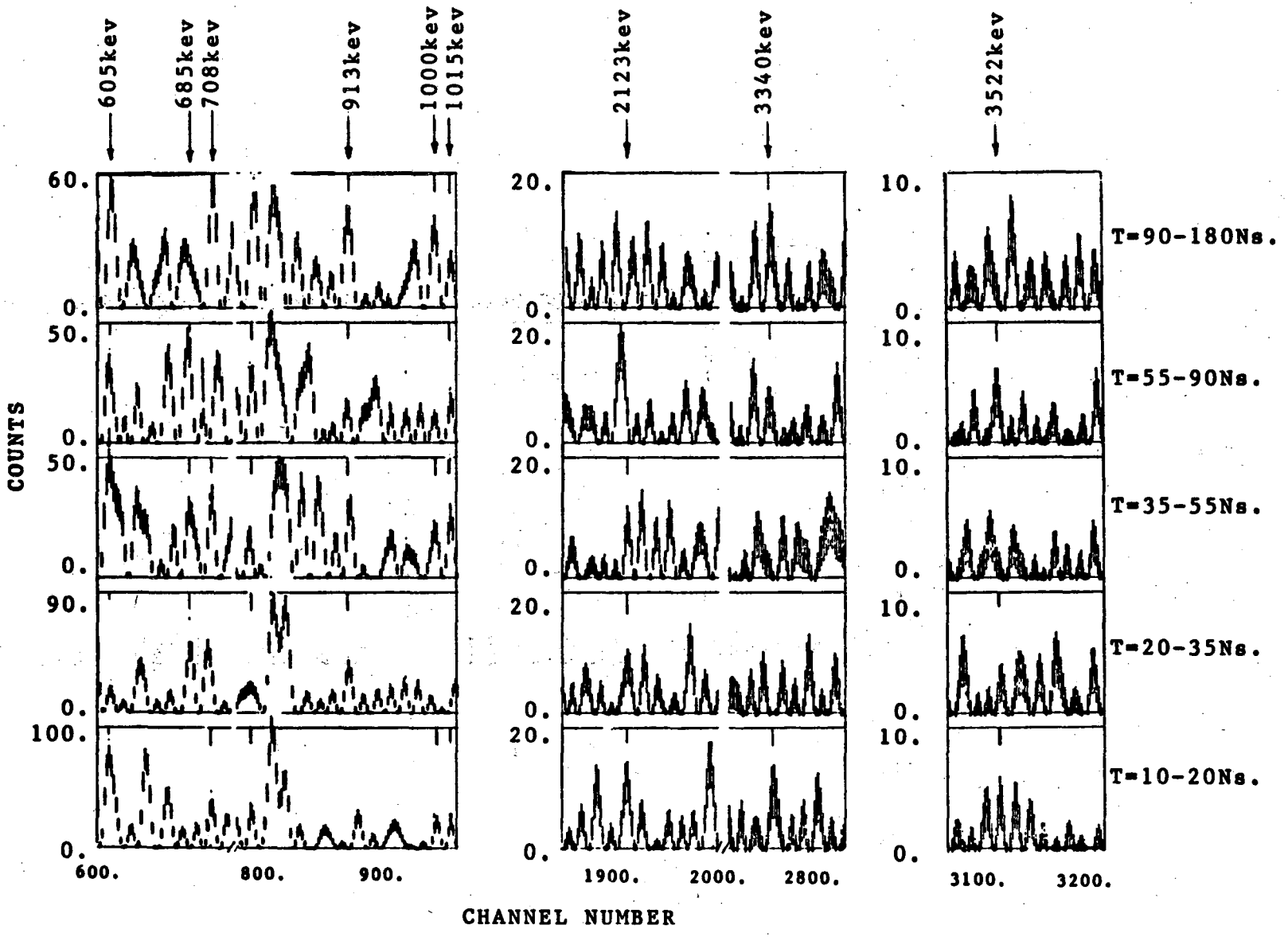


Fig. 4-8 Muonic $^{238}U$ delayed spectra (1980 run)

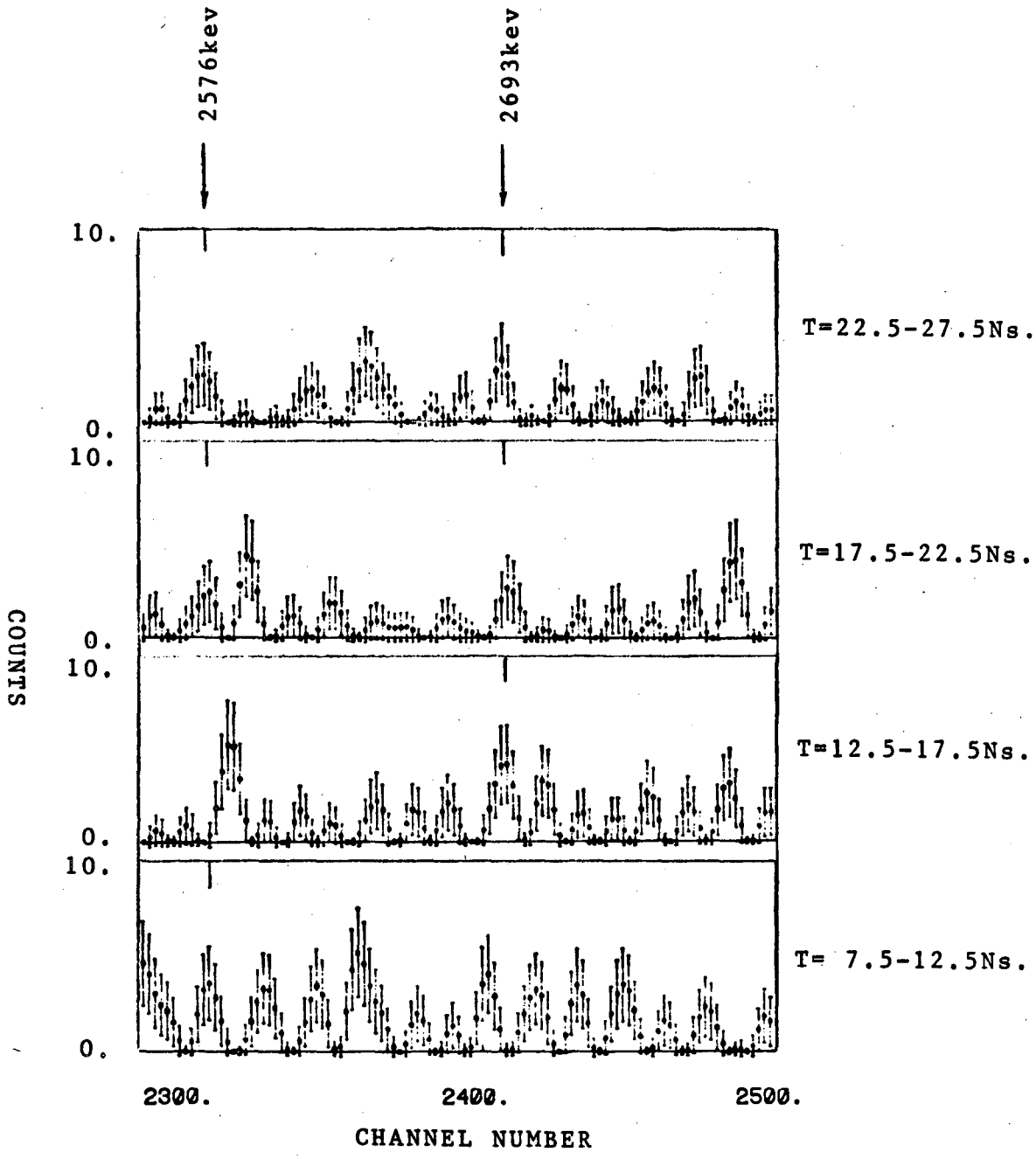


Fig. 4-9 Muonic $^{238}U$ delayed spectra

(1980 run)

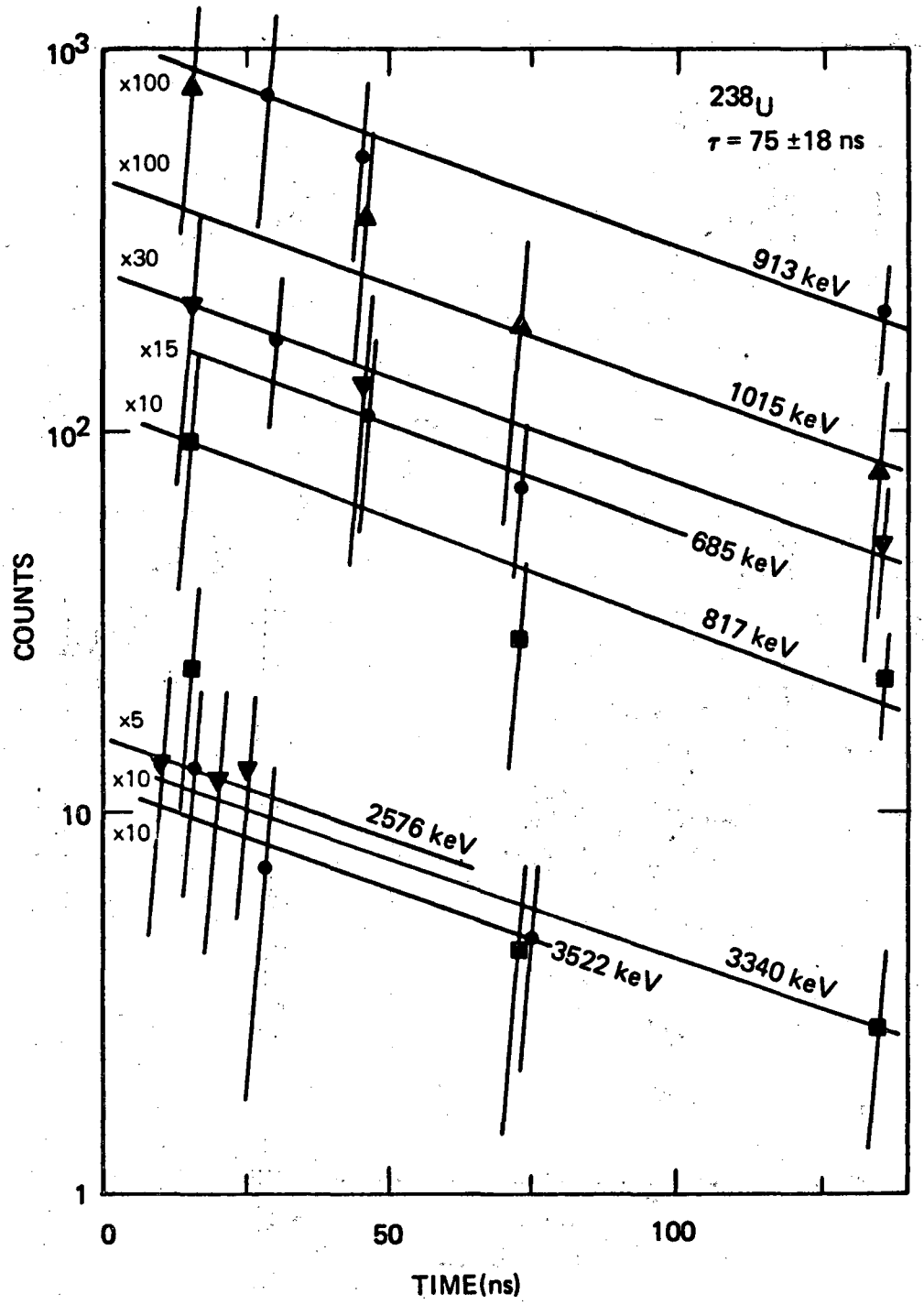


Fig. 4-10-a. Decay curves for the observed $\bar{\mu}^{238}$U delayed gamma rays.

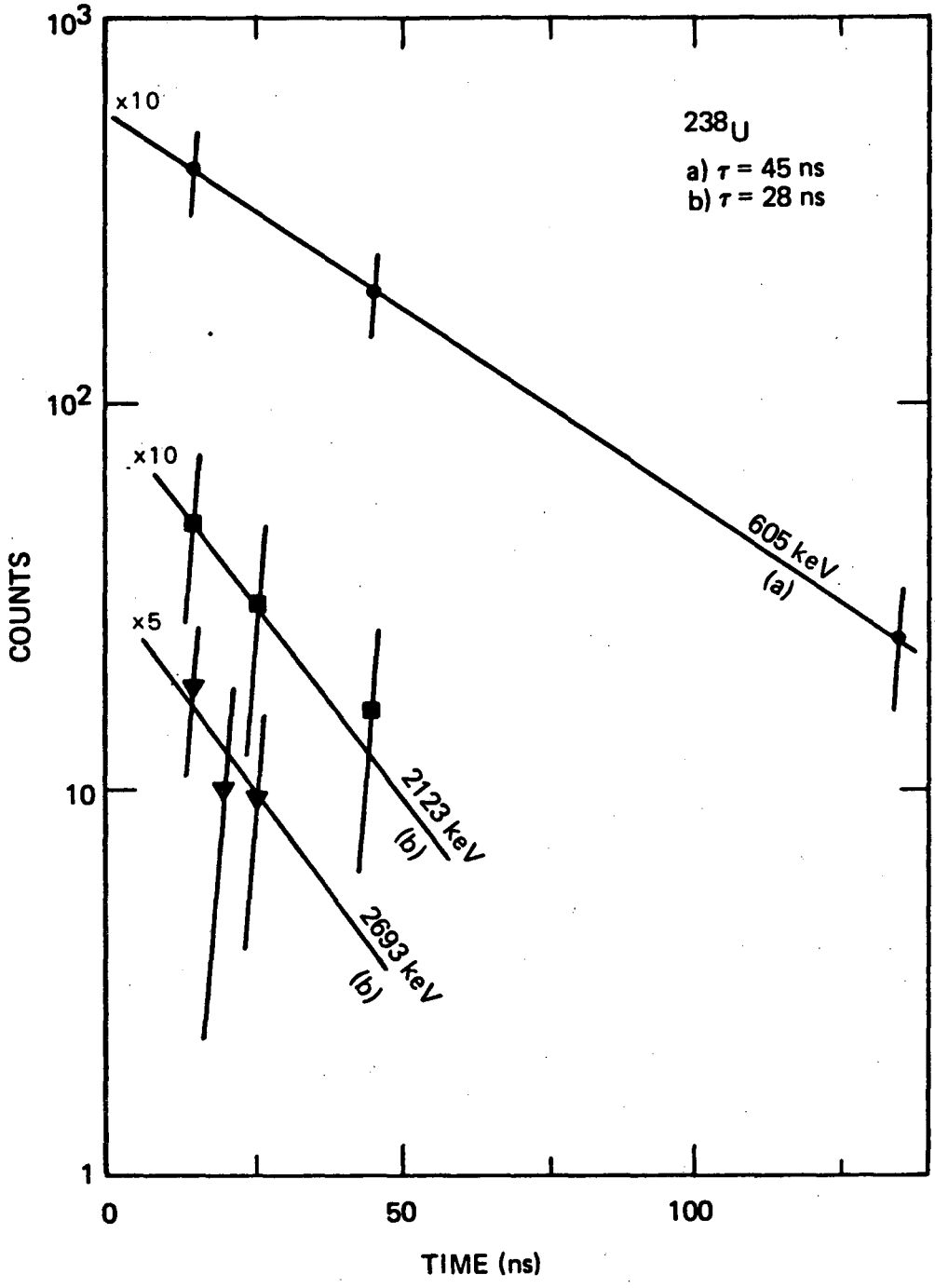


Fig. 4-10-b. Decay curves for the observed delayed transitions in $\bar{\mu}$ $^{238}$U.

Table IV-7 Intensities of delayed gamma rays with $\tau_1 = 75 \pm 18$ nsec

| Energy (kev) | 685 | 817 | 1015 |
|---|---|---|---|
| Intensity (%) per $\mu^-$-stop | 0.18 | 0.17 | 0.16 |

An attempt to fit at least two of our lines into a new level scheme with a different value for isomer shift also failed to produce any result. The half lives and intensities of the second group of gamma rays are given in table IV-8. The high energy neutrons emitted in muon capture by the target nuclei may escape from the target and hit the Ge detector.

Table IV-8 Intensities of delayed gamma rays with $\tau_2 = 28$ ns

| Energy (kev) | 2123 | 2693 |
|---|---|---|
| Intensity (%) per $\mu^-$-stop | 0.19 | 0.15 |

The energy spectra of gamma rays following Ge(n,n'$\gamma$) and Ge ($\gamma,\gamma'$) were studied (Lederer and Shirley, 1978). The 913 kev line was found to match a transition from a $^{76}_{32}$Ge level excited by a (n,n'$\gamma$) reaction. The remaining high energy peaks of the 25 nsec life-time group may have been produced in one of the following processes:

- Inelastic scattering of the energetic neutrons resulting from $\mu^-$-capture in the uranium target may excite high energy levels in $^{238}$U nucleus. The highest of such excited states listed (Lederer and Shirley, 1978) is about 1.2 Mev.
- Emission of gamma rays directly from the $\mu^-$-capture reaction.

These gamma rays could not be attributed to spin isomers produced in $^{238}$U target, since there is a limited possibility of excitation of states with significant spin difference to the ground state by muons. Also, a complex gamma ray spectrum resulting from deexcitation of spin isomeric states in a variety of fission fragments produced by spontaneously fissioning of $^{252}$Cf

(W. John *et al.* 1970) was carefully studied. No isomer with an excitation energy higher than 1.5 Mev was found in fission fragments. The isomeric states populated by prompt fission in the fragments would appear with their real lifetimes and ones excited in delayed fission would be recorded with enlarged lifetime. The $\mu^-$-capture by fission fragments has a characteristic lifetime of $\approx$120 nsec for the heavier and $\approx$200 nsec for the lighter fragment (W. U. Schroder *et al.* 1979). The shorter lifetime group of our gamma rays could not be explained by any reaction connected to $\mu^-$-capture. The energies, the intensities, and the half lives of the remaining unaccounted for gamma rays are given in table IV-9.

Table IV-9

| Energy (kev) | 605. | 708. | 913. | 1000. | 3340 | 3522. |
|---|---|---|---|---|---|---|
| Lifetime (nsec) | 45 | 75 | 75 | 75 | 75 | 75 |
| Intensity (%) per $\bar{\mu}$-stop | .42 | .15 | .19 | .12 | .11 | .07 |

A similar procedure was followed for analysis of the delayed spectra of $^{236}$U data and was applied for both "group 1" and "group 2" sets of spectra. For "group 1" spectra the GAMANL program did not locate any peak appearing in more than one time window, whereas for the "group 2" spectra, two peaks at energies of 2615 kev and 1808 kev were found to appear in three or more time windows. Two other peaks at energies of 845 kev and 1555 kev were only observed in two independent time windows. Again the search through the smoothed background subtracted data succeeded in detecting the appearance of these lines in a third time window, as well as finding some other lines complying with our requirements for being accepted as a delayed gamma ray. Parts of the $^{236}$U spectra exhibiting the appearance of the observed gamma rays in different time windows are shown in Fig. 4-11. A first estimate of the lifetime of each gamma line was found using the least squares method to fit the respective counts in at least three independent time windows.

Table IV-10 Intensities of the delayed gamma rays with $\tau = 66 \pm 8$Ns.

| Energy (kev) | 845. | 1278. | 1555. | 1627. | 2615. |
|---|---|---|---|---|---|
| Intensity (%) per $\mu^-$-stop | .15 | .10 | .13 | .10 | .66 |
| **Energy (kev)** | **3188.** | **3220.** | **3596.** | **3725.** | |
| Intensity (%) per $\mu^-$-stop | .07 | .16 | .11 | .14 | |

The results indicated three categories of lifetimes. A group of the gamma rays could be fit to a common lifetime of about 66 nsec. Table IV-10 gives the energies and intensities of these lines. Also their decay curves are shown in Fig. 4-12-a. Two of the gamma lines showed a shorter lifetime of about 35 nsec and a single one at an energy of 1808 kev was best fitted to 88 ns lifetime. The energies and intensities of these lines are listed in Table IV-11, and the least squares fit to the decay curves are seen in Fig. 4-12-b. The only high energy gamma ray observed with a significant intensity is 2615 kev which within the experimental precision is equal to the well known first excited state in $^{208}$Pb (2614.5 kev). The decay curve for this line could not be fitted to a single lifetime; therefore it is likely that this peak is due to $(\gamma,\gamma')$ reaction in everpresent Pb shielding induced by gamma rays from different sources such as $\mu^-$-capture in uranium nuclei or fission fragments.

Table IV-11 Intensities and lifetimes of miscellaneous gamma rays

| Energy (kev) | 1808 | 1591 | 3787 |
|---|---|---|---|
| Lifetime (nsec) | 88 | 35 | 35 |
| Intensity (%) per $\mu^-$-stop | 0.11 | 0.23 | 0.19 |

The shape isomeric state in $^{236}$U has an excitation energy of 2.35 Mev (Sood and Sarma, 1970) above the normal ground state. Considering 640 kev value for the energy shift due to the

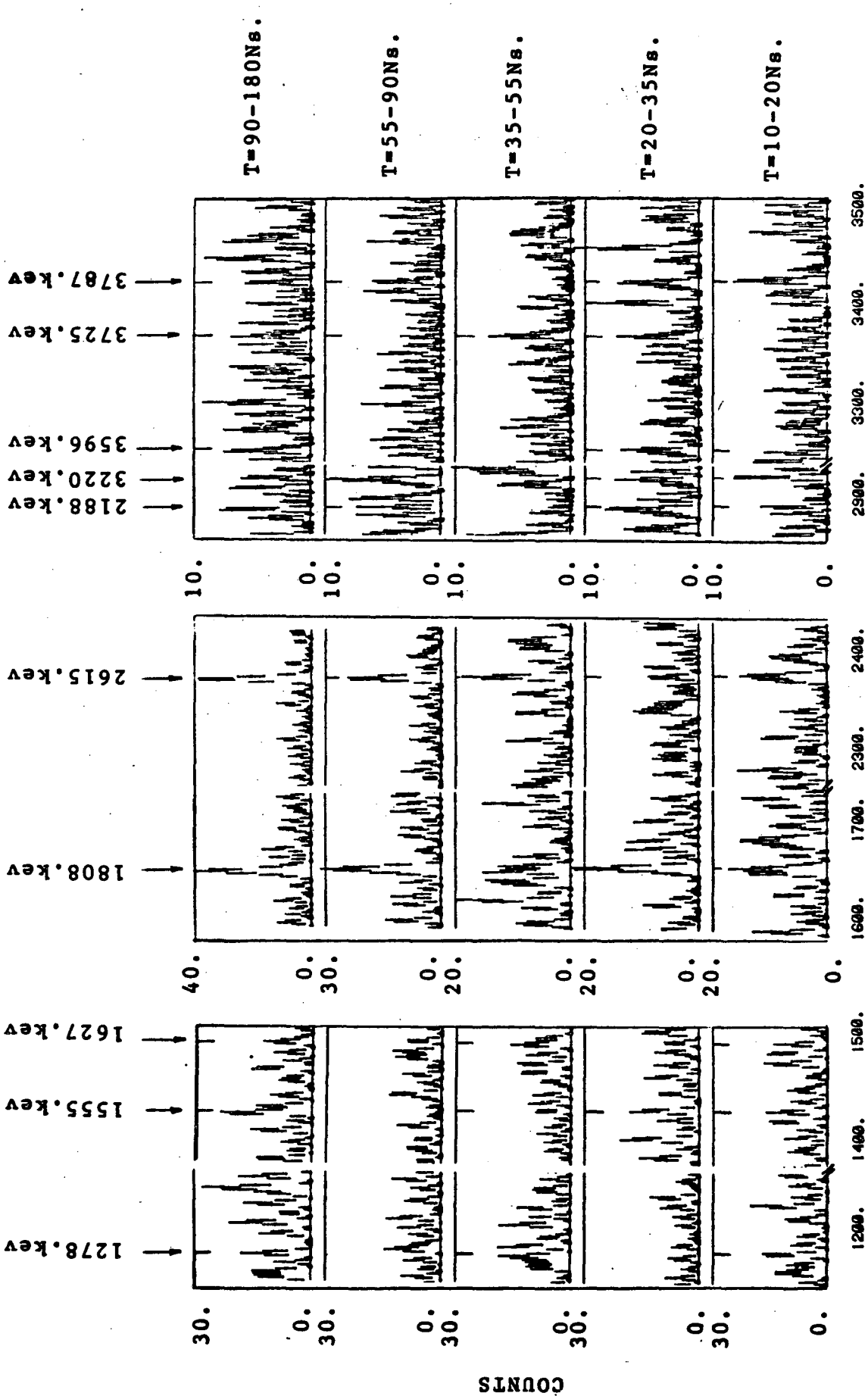


Fig. 4-11 Muonic $^{236}U$ delayed spectra (1981 run)

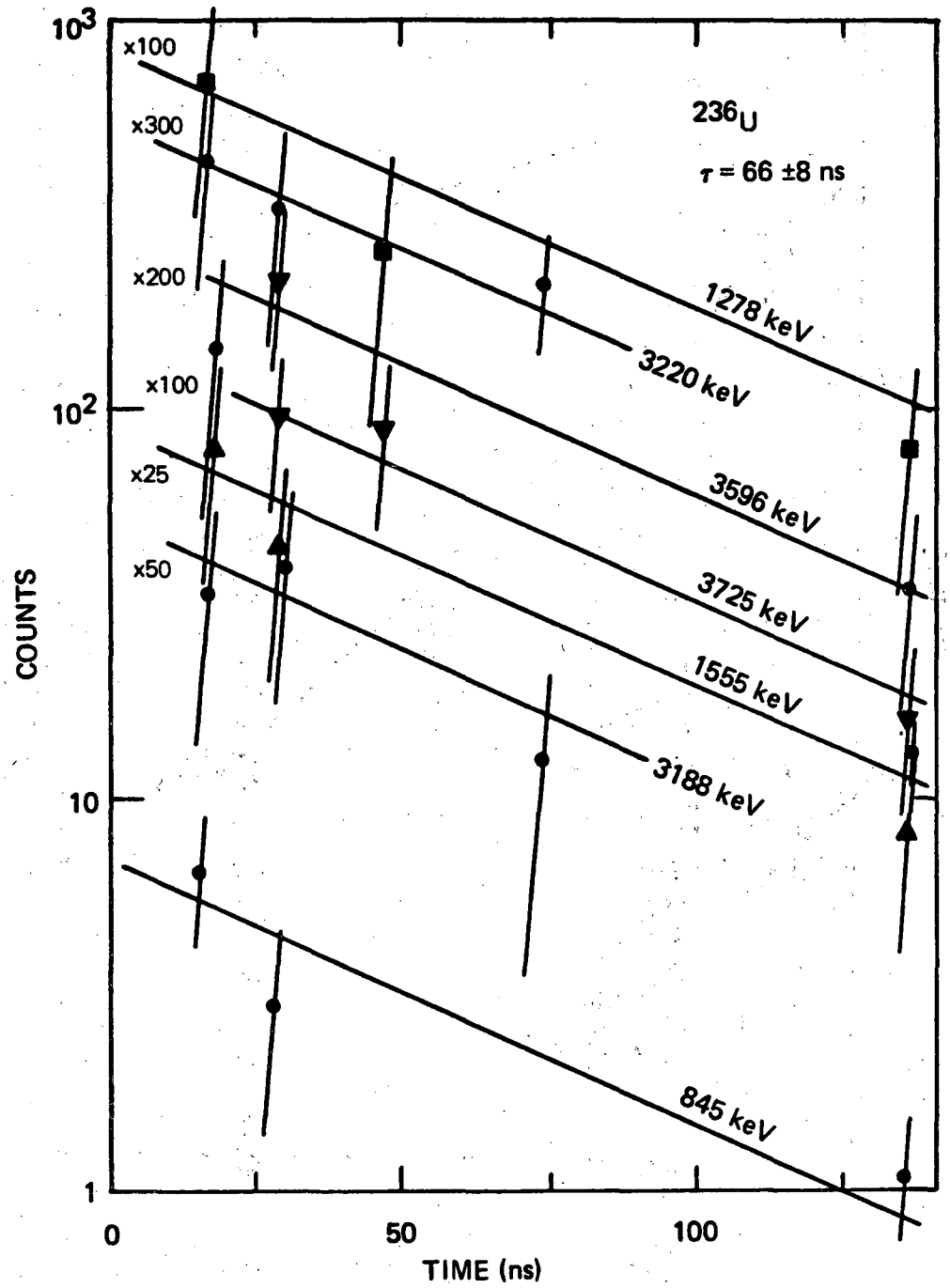


Fig. 4-12-a. Decay curves for observed $\bar{\mu}^{236}$U delayed gamma rays.

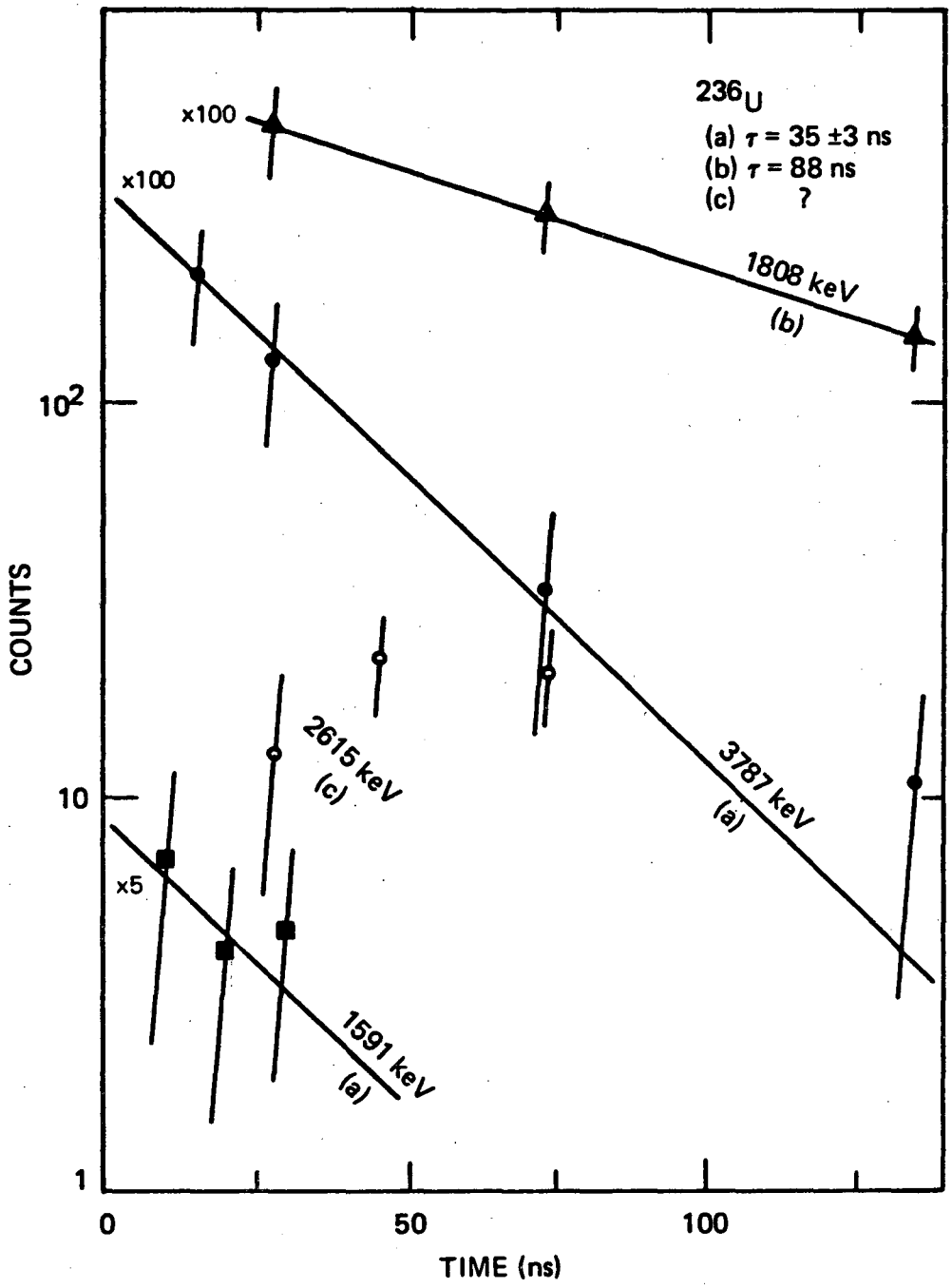


Fig. 4-12-b. Decay curves for observed $\bar{\mu}$ $^{236}$U delayed gamma rays.

presence of $\mu^-$ in the 1s state of the muonic $^{238}$U, calculated by solving the Dirac equation (Fromm *et al.* 1976) and comparing it with the ≈500 kev shift resulting from a non-relativistic calculation for muonic $^{236}$U (Leander and Moller, 1975), it is reasonable to assume a value of about 600 kev for this shift in $^{236}$U. Therefore a transition from the isomeric state to the first excited state in the first well should have an energy in the neighborhood of 2.9 Mev. We did not observe any line at or close to this energy at a sensitivity of about 0.1 percent per muon stop. This sensitivity level was estimated by considering the yield of the 3188 kev line (.07 %) detected using our more careful method of analysis, namely using the plots of the background subtracted data to find the delayed lines. The level scheme of the $^{236}$U nucleus along with the perceived shifted shape isomeric state and the possible transitions form this state to the levels in the first well are shown in Fig. 4-13. None of the supposed transition energies is in close agreement with the energies of the peaks found in our delayed spectra. The processes involved in producing delayed gamma activities in this case are similar to those described for the $^{238}$U case. Within the precision of the fit, the 66 nsec lifetime of some of the observed lines is close to the 70 nsec characteristic lifetime of the $\mu^-$-capture in uranium isotopes. Therefore, it is likely that these gamma rays are somehow connected to the interaction of neutrons emitted during the capture or to the deexcitation of the residual nuclei produced in that process. The 1278 kev is equal to the energy of a known transition in $_{91}^{235}$Pa. Also the 845 kev and the 1627 kev are in agreement with the 845.5 and 1628 kev values for two known transitions in $_{91}^{235}$Pa. The excited states of these nuclei are expected to be populated in a $\mu^-$ capture of the $^{236}$U nucleus followed by emission of one or two neutrons. The peak at 1808 kev has the second largest intensity in our spectra of delayed gamma rays. Its energy is equal to the excitation energy of one of the levels in $^{236}$U known to be populated in the $\bar{\beta}$ decay of the $_{91}^{235}$Pa. But the $_{91}^{235}$Pa has a half life of 9.1 m and therefore it can not be used to explain the existence of the 1808 kev line in our delayed gamma spectrum. The 88 ns lifetime measured for this line may be attributed to a $\mu^-$-capture related reaction. This reaction can be assumed to be an inelastic scattering of neutrons on target nuclei.

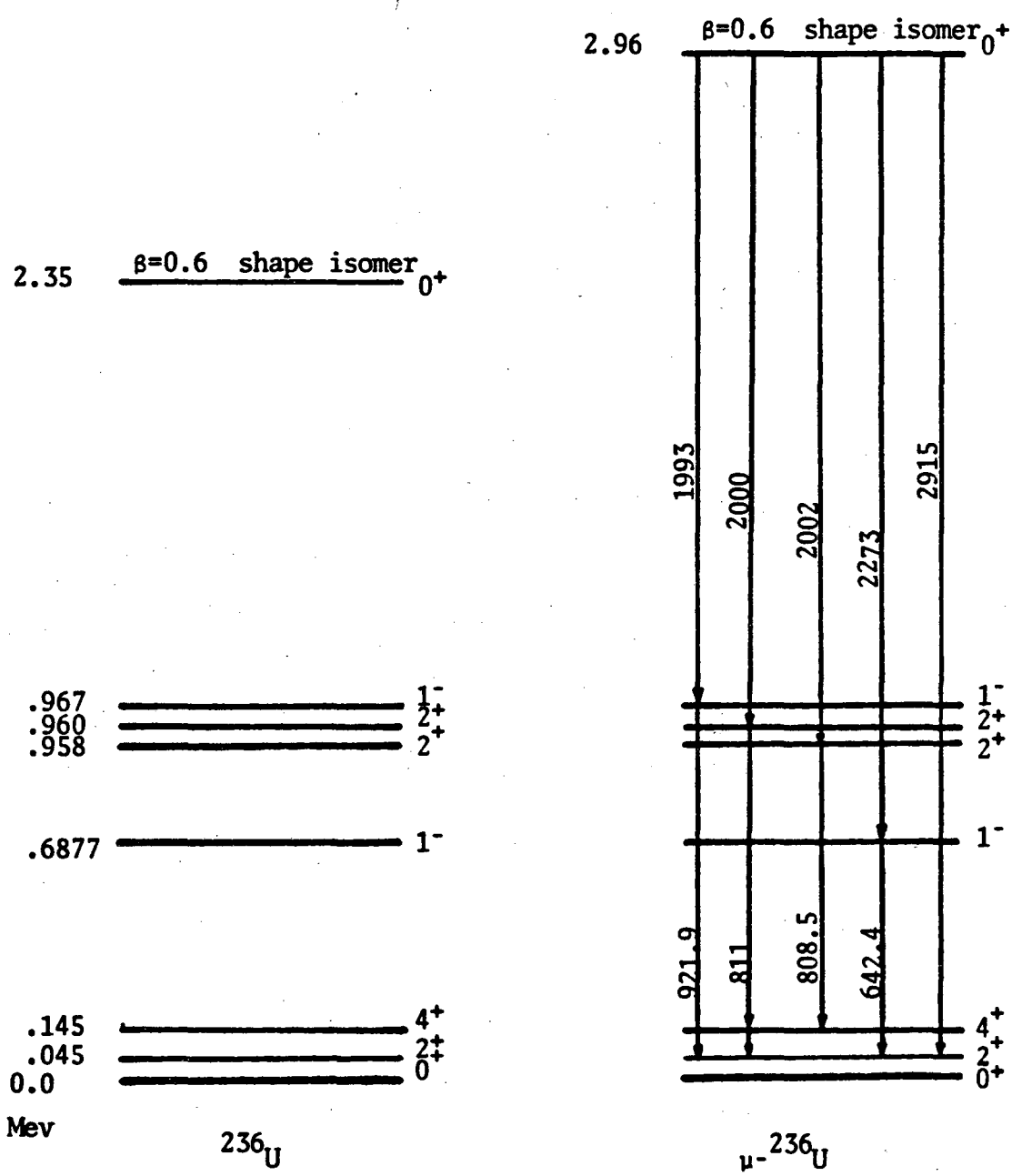


Fig. 4-13 Level schemes of $^{236}U$, on the left are the levels of the bare nucleus, on the right possible transitions from the the shape isomeric state in $\mu$-$^{236}U$ are shown.

# CHAPTER 5

# GAMMA RAY DETECTION SENSITIVITY

## 5.1. Introduction

In dealing with weak and hard-to-detect activities, it is essential to try to determine the sensitivity threshold by establishing a lower limit of detection of an activity. In other words, one wants to know how effectively the detector system can distinguish between a measurement made when the true activity is zero and a measurement when the true activity is nonzero. In this chapter a statistical method developed to evaluate the gamma ray detection sensitivity of our experiments will be discussed. As explained in the previous chapter, in analysis of our experimental data we used two independent procedures. It is to be understood that the detection limits established by this statistical method are applied only to the first analysis procedure, which was more systematic and used the GAMANL program to locate and identify the peaks. It is true that the second procedure turned out to be more sensitive in detecting delayed gamma rays, but, because of many repetitions necessary to accomplish a reliable result from the statistical technique, it was not suitable for application to this procedure. For that case we can simply say that the lower detection limit was equal to the smallest yield found for detected gamma rays in the energy range of interest.

There are two important questions to be answered in this chapter:

(1) If the program could not identify a candidate gamma ray at a certain energy, what would be the upper limit of its yield and at what confidence level? In other words, how confident are we that it could have detected the gamma ray if its yield was equal to that set upper limit?

(2) For a peak identified by the program, how confident are we that it represents a real gamma ray rather than being a statistical artifact, a "fake peak"?

The method developed to deal with these questions is in fact a new standard method. The significance of the technique used is that it provides the peak identifying program with a universal curve which can be used for any Ge $\gamma$-ray spectral analysis with that program. Namely, to determine the detection lower limit for any spectrum at an arbitrary energy, one just needs to find out the background count at that energy and refer to the universal curve provided to figure out the answer at the desired confidence level. The description of the method and the required curve for the user of the GAMANL program is given in the following sections. The results are used to study some other interesting aspects of the problem, like the variation of detection sensitivity vs. energy and time after muon stop of the gamma event, at fixed confidence levels as well as the confidence level as a function of yield limit.

### 5.2. Statistical Approach to Detection Sensitivity Determination

Due to the random nature of the background count-rate and the background-plus-true activity count-rate, it is not possible to claim a certain detectable lower limit $Y_{ll}$ for a gamma ray yield without attributing to it a confidence level $C_L$. This confidence level in fact tells us that the probability for an existing gamma ray in the spectrum with a measured yield of $Y_{ll}$ to be located by the analyzing program is equal to $C_L$. From this definition one can always practicably measure the probability without using any actual sample counting. This can be accomplished by taking the following steps:

1) Artificially generating a spectrum consisting of a single gamma ray with an intensity equivalent to the yield under consideration and a background resembling the actual one at the desired energy.

2) Randomizing it N times and applying the spectral peak analyzing program each time and counting the number of times that the peak is located, P.

Then the confidence level would be equal to P/N. The method which is used in this work has essentially the same statistical framework, except for a feature that makes it more practical to use. Instead of making one peak at a certain energy and using the analyzing program repeatedly, a range of energy of interest is chosen, and N number of peaks are generated over the real background in that range and the result is randomized. However, the areas under these N peaks should not be the same, since the backgrounds are not the same. In other words, in order to make this situation resemble a case with N times repetition of a single peak, the background should be kept constant over the entire range. This means that the procedure should be repeated for each energy point if the limit yield at a certain confidence level as a function of energy is needed. This complication was avoided by just using the actual background and generating the N peaks with areas varying with background (or energy) in a consistent manner, such that the confidence level be almost independent of energy in the range of interest and can be taken as the average value for that range. Using a trial and error method with the help of some intuition it was discovered that the relative statistical error of the peak area, $\frac{\sigma_A}{A}$ is a good figure of merit to be kept constant over the entire energy range. It can easily be shown that the above ratio is equal to $\sqrt{A+2B}/A$, in which A is a peak area, B is the background under that peak.

### 5.2.1. Background Simulation

One major obstacle in recovering weak peaks from a Ge detector gamma ray spectrum is the random fluctuation of the background. The effect of these fluctuations on the spectrum appears in two ways. One is the introduction of fake peaks, or so-called frauds, into the spectrum, which may be taken as real peaks by the analysis program. The other effect is to distort small real peaks in a way that they can no longer be identified by the program. The strength of these effects, being characterized by the background count rate statistical error, is in fact very background dependent. Therefore, in order to analyze these effects in a more realistic situation it is necessary to use the real background underlying the spectrum, rather than implying any kind of averaging. Using the GAMANL program and the flexibilities in its smoothing feature,

we could reduce the actual spectrum into its background envelope. The filter function which was used to eliminate the high frequency variations from the spectrum can be chosen narrow enough to wash out all peaks by smoothing the spectrum down to its background envelope. A typical actual spectrum and its background envelope are shown in Figs. 5-1 and 5-2. The cut-off frequency of the filter function used was about 20 times smaller than that of the one used for normal smoothing of the data.

### 5.2.2. Random Peak Generation

The generated peaks were centered at known channels and at equal distance from each other. Each peak had a Gaussian shape with a FWHM varying with energy. The variation was according to a second order polynomial of which the parameters were found by a least-squares-fit of the actual FWHM of our x-ray spectra. The area A of each peak was found based on a constant value for the ratio $\sqrt{A+2B}/A$, where B was the background counts under that peak. Since the spectrum was finally randomized, it was not expected that all peaks identified in the analysis of the generated spectrum be found with the same value of $\sigma_A/A$ as used in the calculation of their areas. In fact the probability of finding located peaks with $\sigma_A/A$ between value of $S_1$ and $S_1 + \Delta S$ showed a quasi-Gaussian distribution. It was discovered that the mean of this distribution could be moved around if the base width of the construction peaks were changed. This change was to be expected, because the base width of each peak determined the portion of the background allocated to that peak. A proper value for the base width was then found to be 1.4 times the peak FWHM, which resulted in a value for the mean of the distribution of $\sqrt{A+2B}/A$ of located peaks to be equal to the value used originally in generating the simulated spectrum.

The spectrum constructed by superimposing the peaks on the background envelope was to be randomized in order to simulate an actual spectrum. The Monte Carlo randomization process was performed channel by channel and based on a Poisson or Normal distribution depending on the number of counts in that channel. The number of counts in fact defined the mean of the

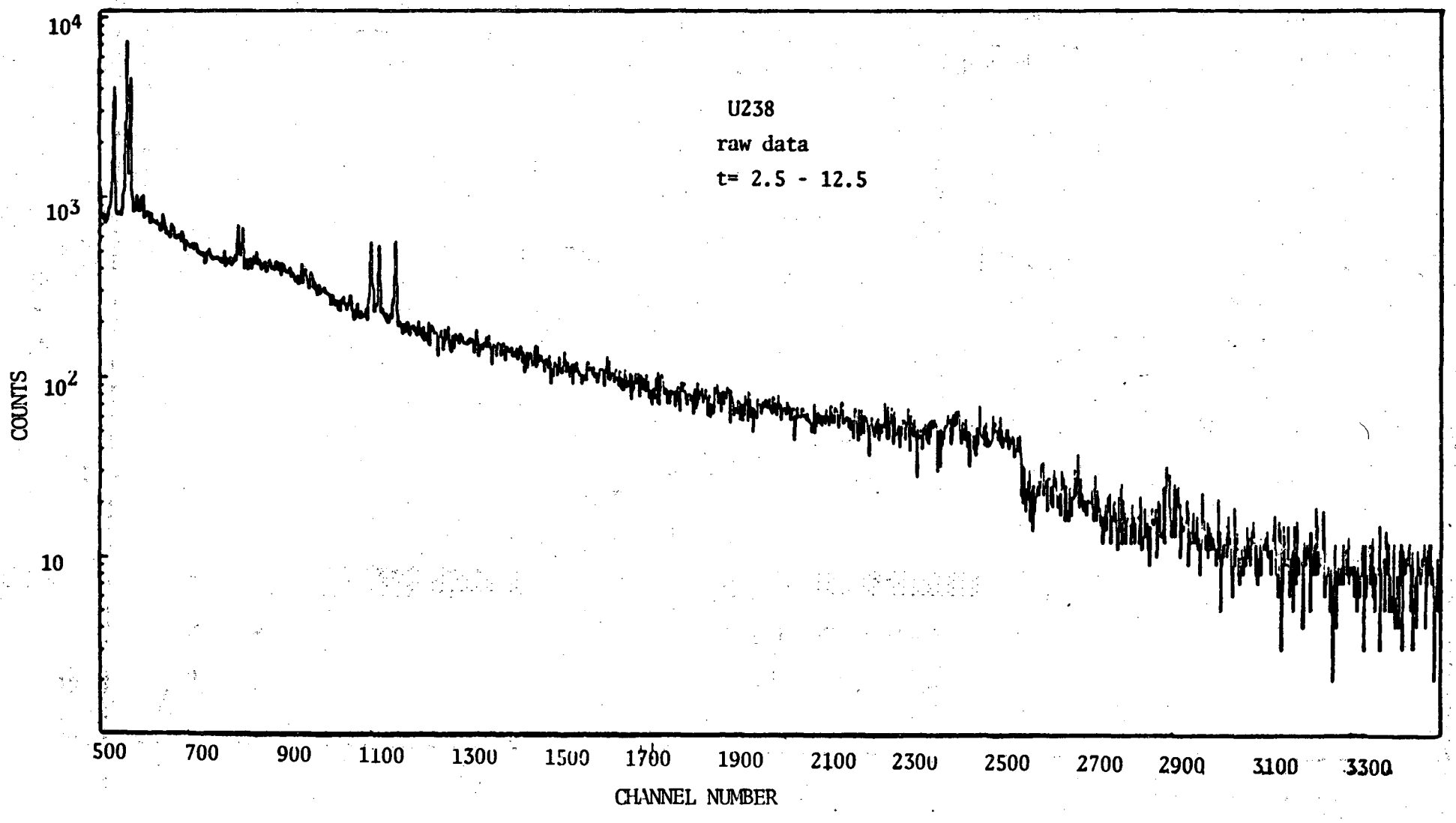


Fig. 5-1 A typical raw data spectrum, the background envelope of this spectrum is shown in fig. 5-2

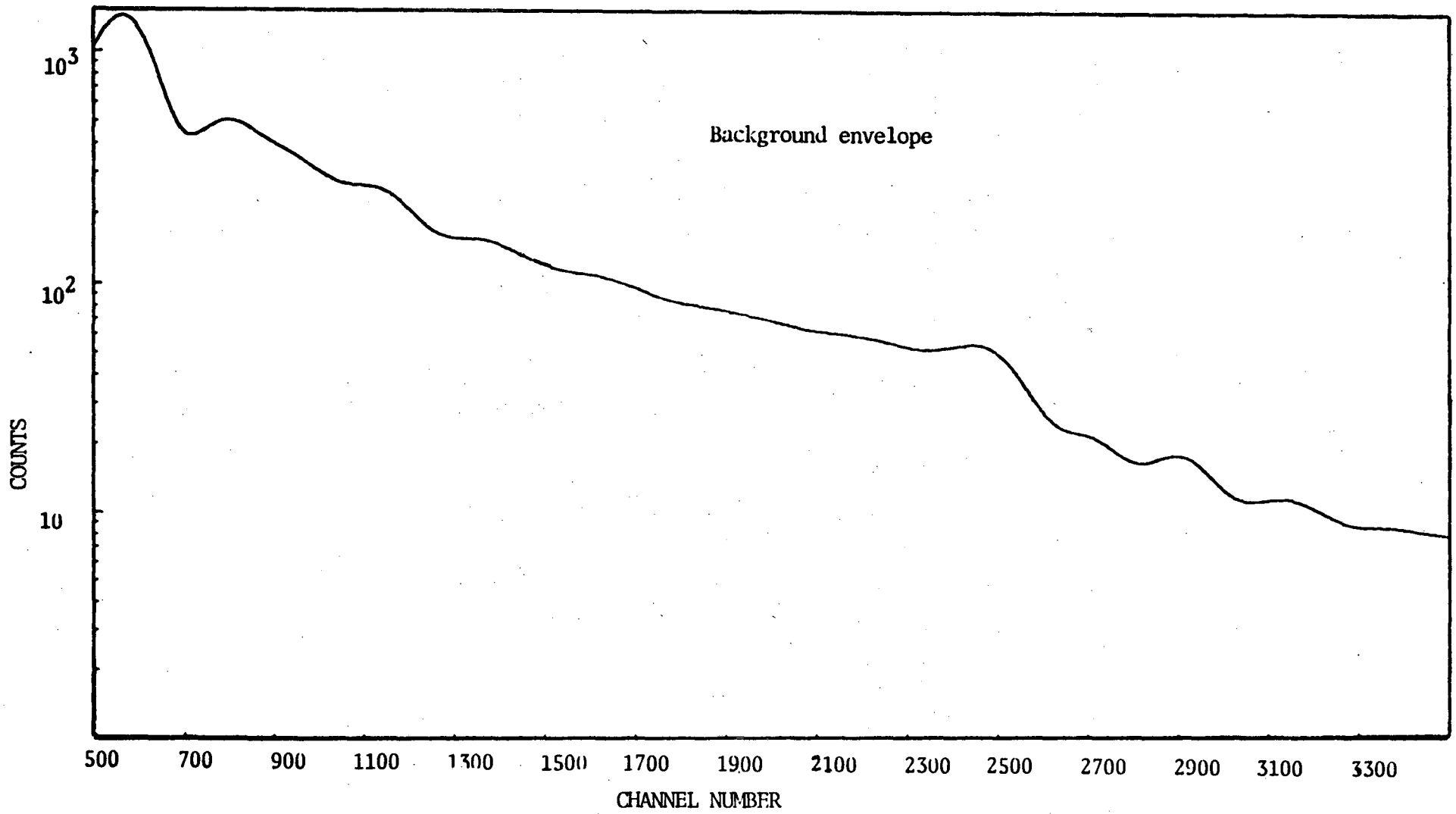


Fig. 5-2 Background envelope of the raw data spectrum shown in fig. 5-1

distribution. If the mean was less than 50 the Poisson distribution was used. The randomized value $n_{ri}$ for the number of counts $n_i$ of ith channel of the spectrum was calculated as follows: Suppose the value of $N_i$ implied use of a Poisson distribution as shown in fig. 5-3. Also suppose the random number generated by the computer was $\alpha$ ($0<\alpha<1$), then the randomized value $n_{ri}$ was chosen such that the Poisson distribution predicted a probability of $\alpha$ for n to be less than $n_{ri}$. For channels with a large number of counts in them the Normal distribution was used in a similar manner. In order to assure the random nature of the generated spectra, for sensitivity test of each spectrum and at any yield level ($\Delta A/A$) a new random number seed was used. A typical generated spectrum on the background of fig. 5.2 is shown in fig. 5-4.

### 5.3. Analysis of the Generated Spectra

Although all the constructed peaks were actually centered at known channels (energies), due to the randomization process their centers should not be expected to remain at the same channels. This implies that, when analyzing the generated spectrum, it is necessary to allow an acceptance window of a few channels around the known peak centers depending on the channel number, when the search for the located peaks is conducted. The acceptance window at each energy is recommended to be a fraction of the peak FWHM at that energy. The universal curve depicting the variation of the confidence level vs. the values of $\sigma_A/A$ for two different acceptance windows (A.W.) are shown in fig. 5-5. The confidence level at each value of $\sigma_A/A$ is independent of the form of the spectral background, and its values for different spectra should follow a Normal distribution due to their random nature. This fact was confirmed by determining the confidence levels for several spectra at different values of $\sigma_A/A$. The measured points in fig. 5-4 are the mean values of these confidence levels, and the error bars show the standard deviations. The form of the curve may be different for different spectral peak analyzing codes, depending on the details of their peak identification methods. However, it will be a characteristic of the program and needs to be found once for all times. The obtained confidence level curve in fact ascribes to any gamma ray yield a certain confidence level. The

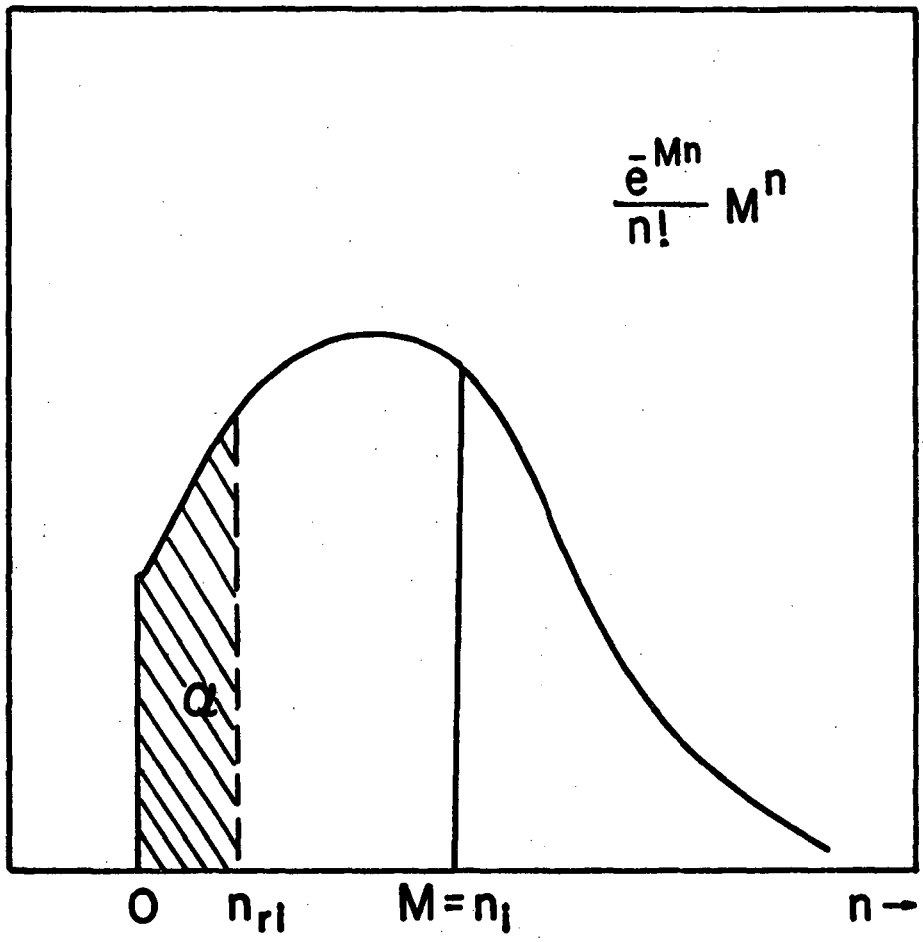


Fig. 5-3 Poisson distribution used for randomization of the generated spectra, in channels with number of counts less than 50.

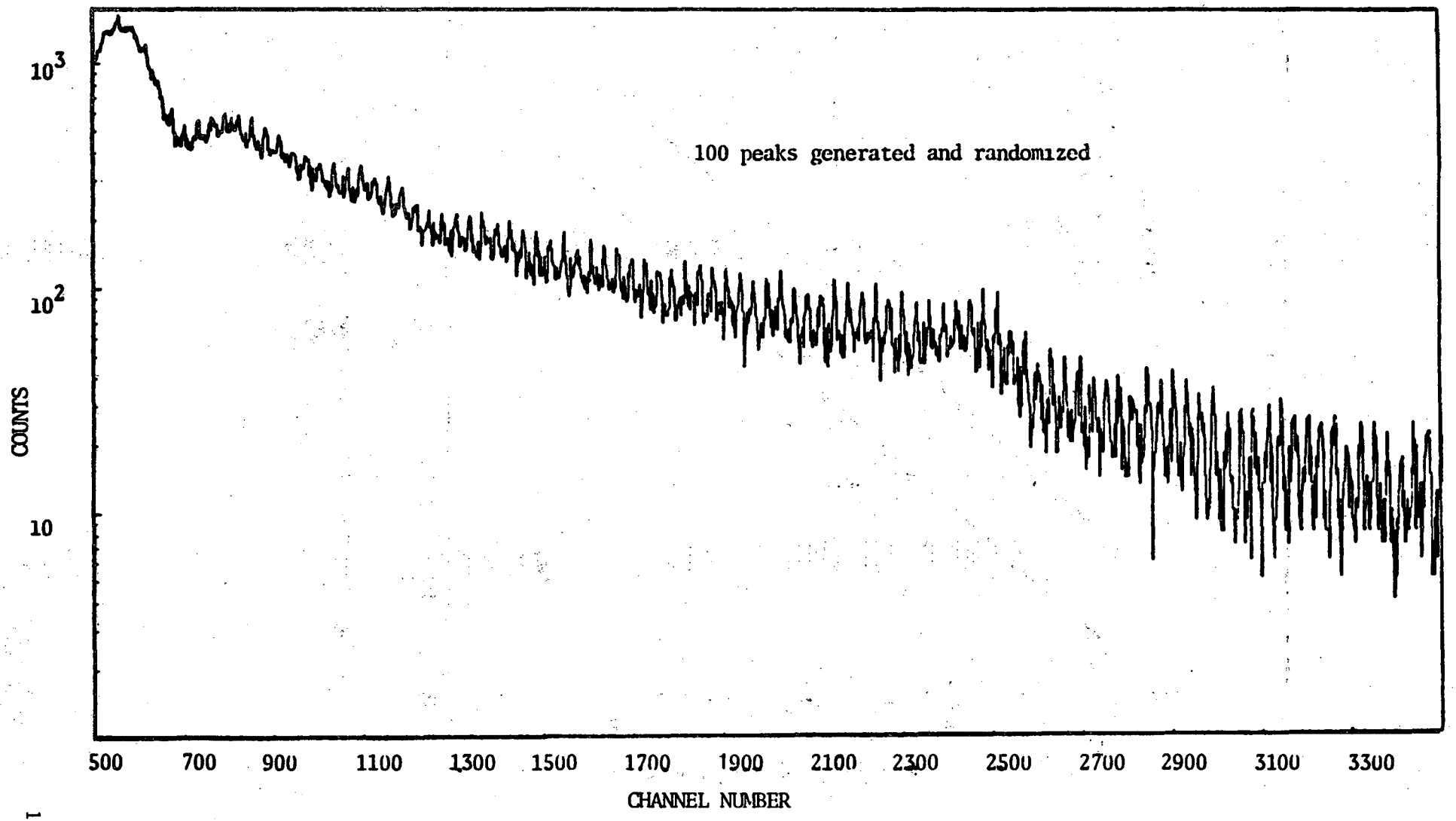


Fig. 5-4 Genertated and then randomized spectrum with 100 constructed peaks

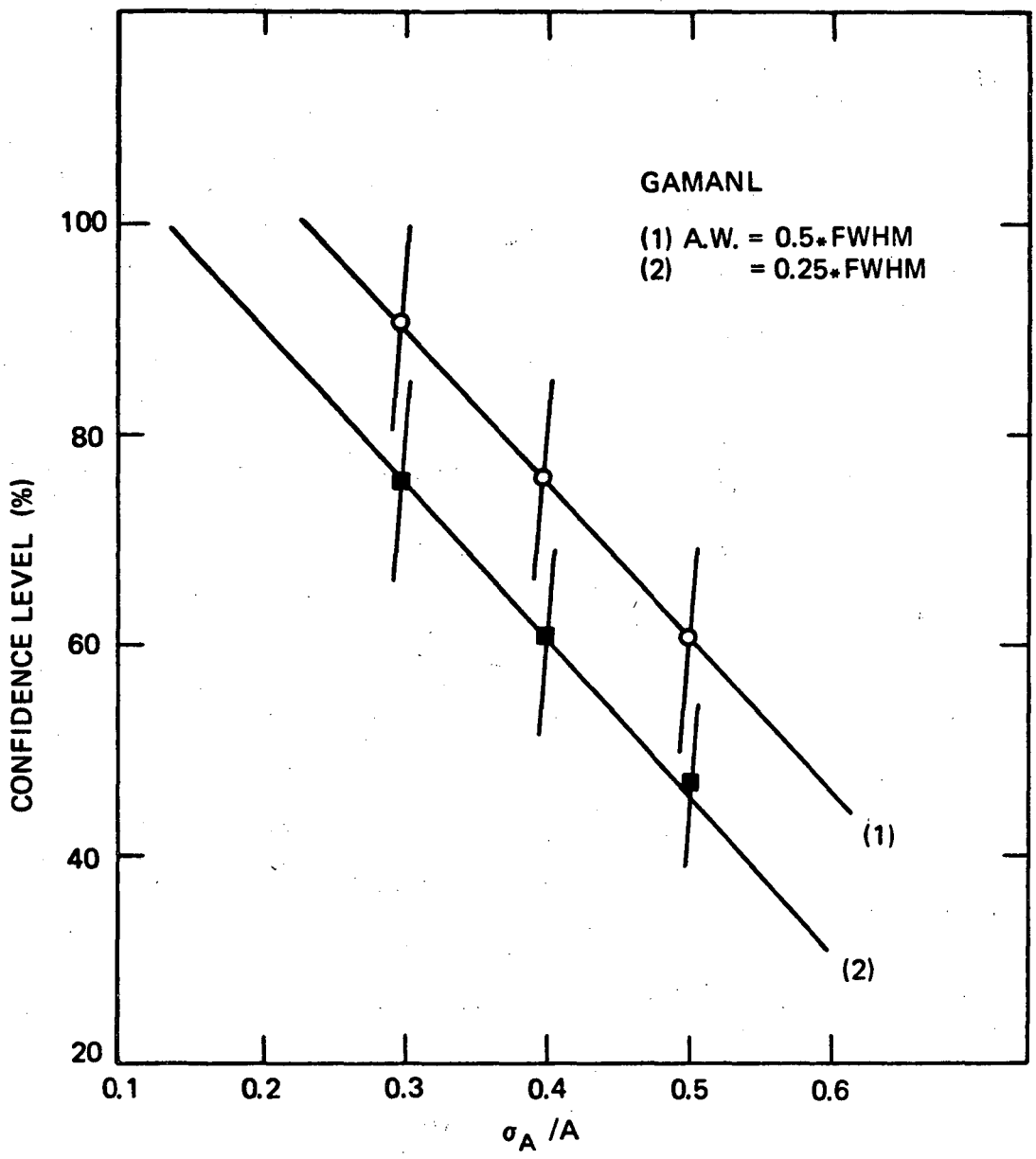


Fig. 5-5. Universal confidence level curve for GAMANL program.

$\sigma_A/A = \sqrt{A+2B}/A$ for a specified yield of a gamma ray can be obtained by substituting for A and B, where A is the respective spectral peak area and B is the estimated background area under that peak found from the spectrum. The curve may also be used to measure the detection sensitivity for a sought gamma ray at a certain confidence level. For this application one can find from the curve the value of $\sigma_A/A$ corresponding to that confidence level. Knowing the background (B) from the spectrum and using the expression for $\sigma_A/A$, the peak area A is calculated. The area is then translated to the proper yield in which the detection sensitivity is to be expressed.

### 5.4. Results and Discussion

The sensitivity test results presented in this section are based on a value of $\sigma_A/A = 0.4$ which corresponds to a 75% confidence level. The sensitivity for detecting a back-decay gamma ray in $^{236}U$, for assumed experimental mean lives of 12, 25, 40 and 70 nsec are shown in figs. 5-6 to 5-9 respectively. For each assumed life time the detection sensitivity of a few time windows after muon stopping are shown. The yields are calculated from the expression (4-4), and their values at the energy of any nonobserved transition are interpreted as the upper limit for yield of that transition at a 75% confidence level. The yields above each curve should be observed in the respective time window with confidence levels higher than 75%. The fall of the curves with increasing energy starts at about 2000 to 2500 kev. The rising and falling parts of the curves, in fact, are due to the predominant effects of either the absolute Ge detection efficiency or the variation of the background with energy respectively. The first factor tends to increase the yield as the energy increases, while the background decreasing with energy at a fixed $\sigma_A/A$ (.4) translates into a decreasing A and therefore decreases the yield with energy increasing. It is seen from these figs. that for gamma rays with an assumed measured mean life less than 25 nsec, in most of the energy range we can have a sensitivity limit lower than .2% $\gamma$'s per $\bar{\mu}$ stop in the target nucleus, and for assumed life times of 25 to 70 nsec this limit is less than .3% gammas per $\bar{\mu}$ stop over the entire energy range.

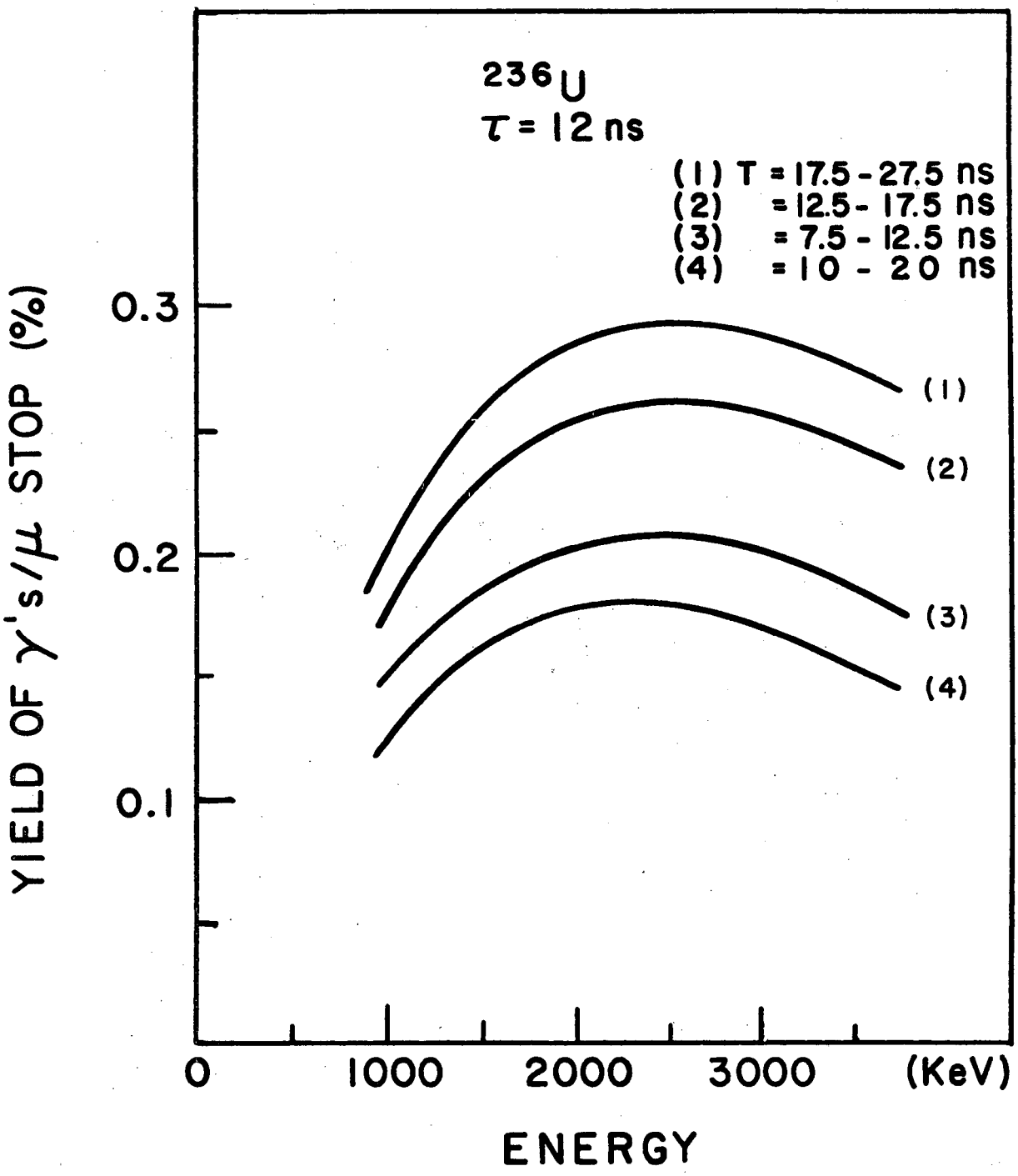


Fig. 5-6 Sensitivity of 4 different time windows for detecting a gamma back-decay of 12 ns mean-life.

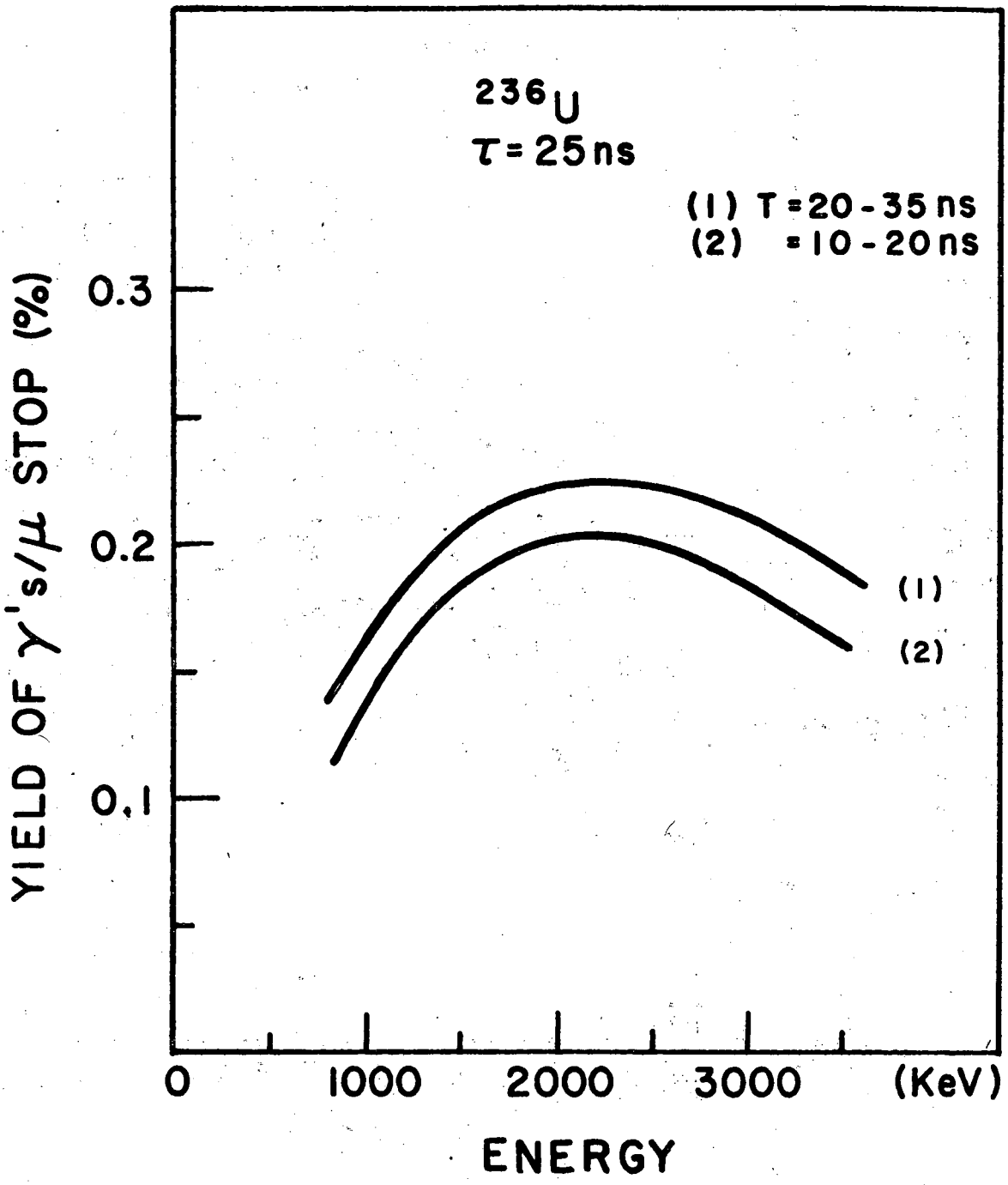


Fig. 5-7 Sensitivity of 2 different time windows for detecting a gamma back-decay of 25 ns mean-life.

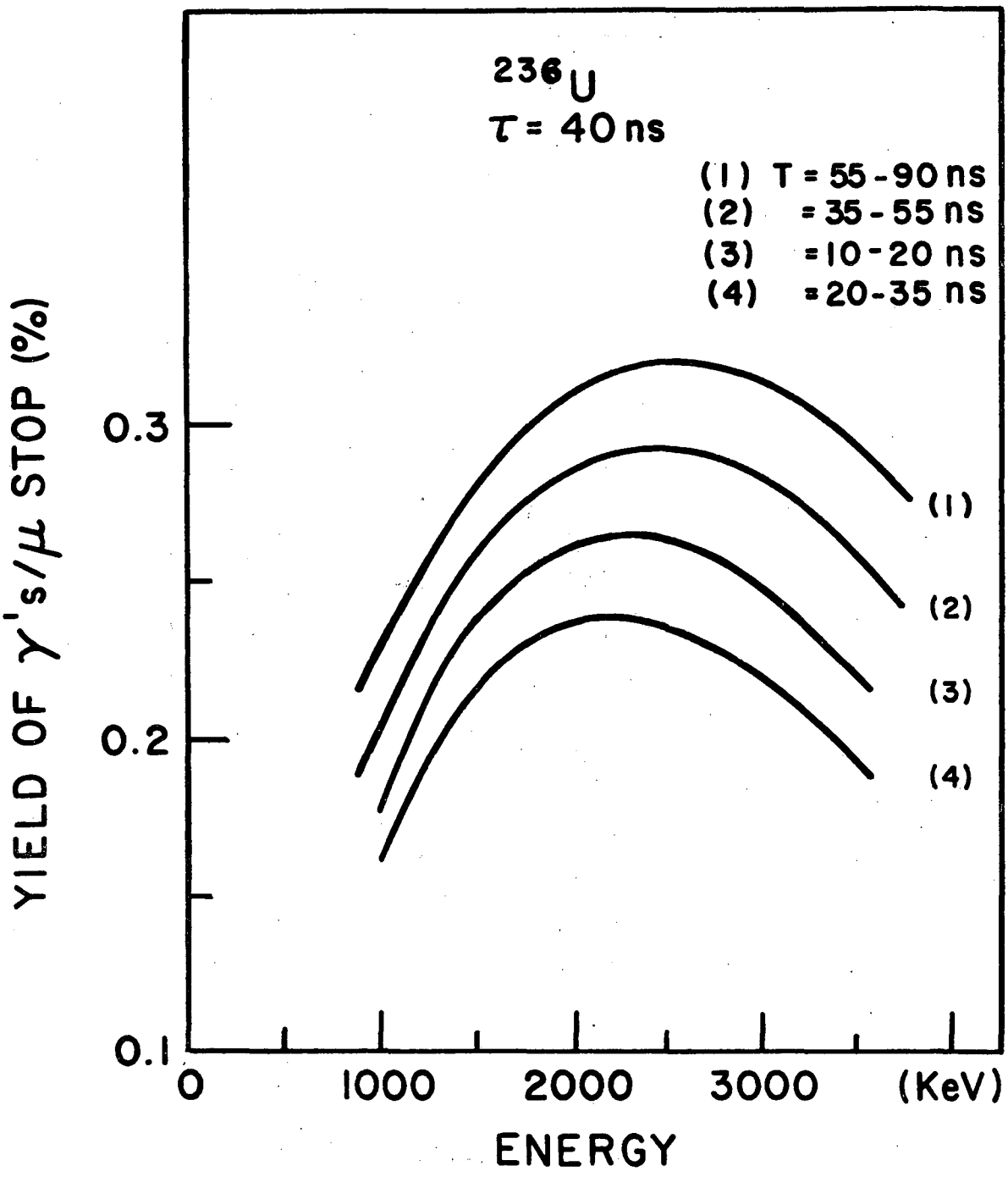


Fig. 5-8 Sensitivity of 4 different time windows for detecting a back-decay gamma ray of 40 ns mean-life.

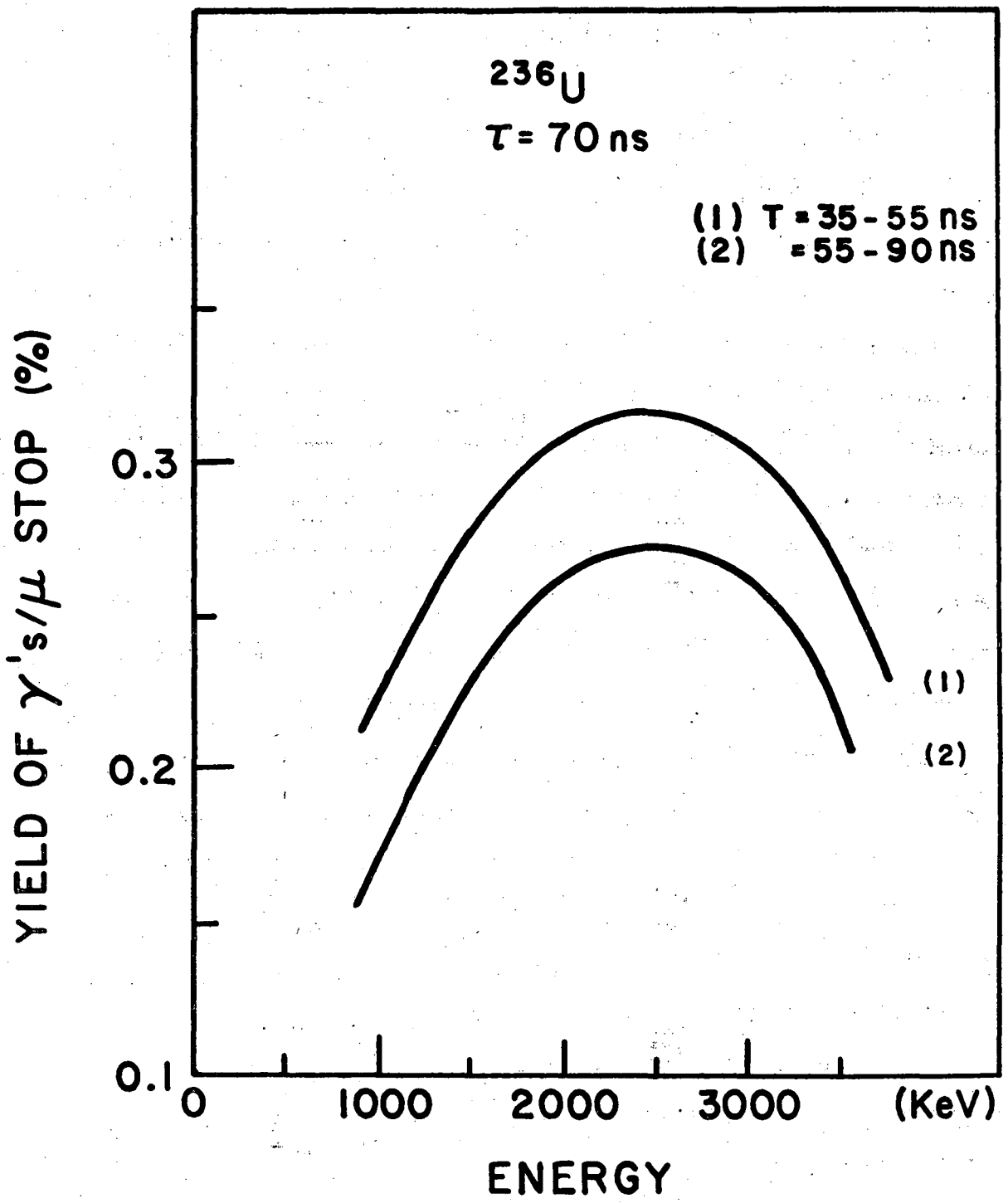


Fig. 5-9 Sensitivity of 2 different time windows for detecting a gamma back-decay of 70 ns mean-life.

The detection sensitivity for detecting shape isomeric back-decay in $^{238}U$, for the same assumed measured transition life times in different time windows is shown in Figs. 5-10 to 5-13. The factors involved in determining the form ofthe curves are similar to those described for $^{236}U$ results. The difference observed in the behavior of the sensitivity vs. energy, namely the disappearance of a rising part indicate that for $^{238}U$ spectra the background should fall much faster as energy increases. The respective background data were compared and the result confirmed the explanation. In fact, the $^{236}U$ background spectra fall about five times faster than those of the $^{238}$. The detection sensitivity limits of the most sensitive time windows are about .15% per $\bar{\mu}$ stop for the assumed lifetimes of 12 and 25 nsec and are less than .2% for assumed life times of 40 and 70 nsec, in the energy range of the two muonic $^{238}U$ shape isomeric back-decay candidate gamma rays (Fromm *et al.* 1976). Since we did not observe these transitions in any time window, the above results imply that, if such transitions with experimental lifetime of around 12 nsec did exist, they should have a production yield of less than .15% per $\bar{\mu}$ stop in the target nucleus. In Figs. 5-14 and 5-15 the detection sensitivities for several assumed life times over the energy range of interest in two different time windows are compared.

So far we have studied the variation of detection sensitivity as a function of energy, one can also use the same information to see what the detection probability of a certain gamma transition at a specified yield would be in a certain time window. The result of a typical study of this sort is shown in Fig. 5-16.

This figure shows the behavior of the confidence level for detection of a 25 nsec mean life transition at a yield of .2% per $\bar{\mu}$ stop in a 20→30 nsec time window. As expected from the results of our detection sensitivity studies, for the same yield the higher energy transition had a better chance of being detected in our $^{238}U$ experiment. The confidence level values found in this way, at a specified yield $Y_\gamma$ for a non-observed candidate transition, can be interpreted as being "the chance of that transition's having an actual yield lower than $Y_\gamma$, i.e. the $Y_\gamma$ being its upper limit yield." It is obvious that this chance should be enhanced if we find some other time

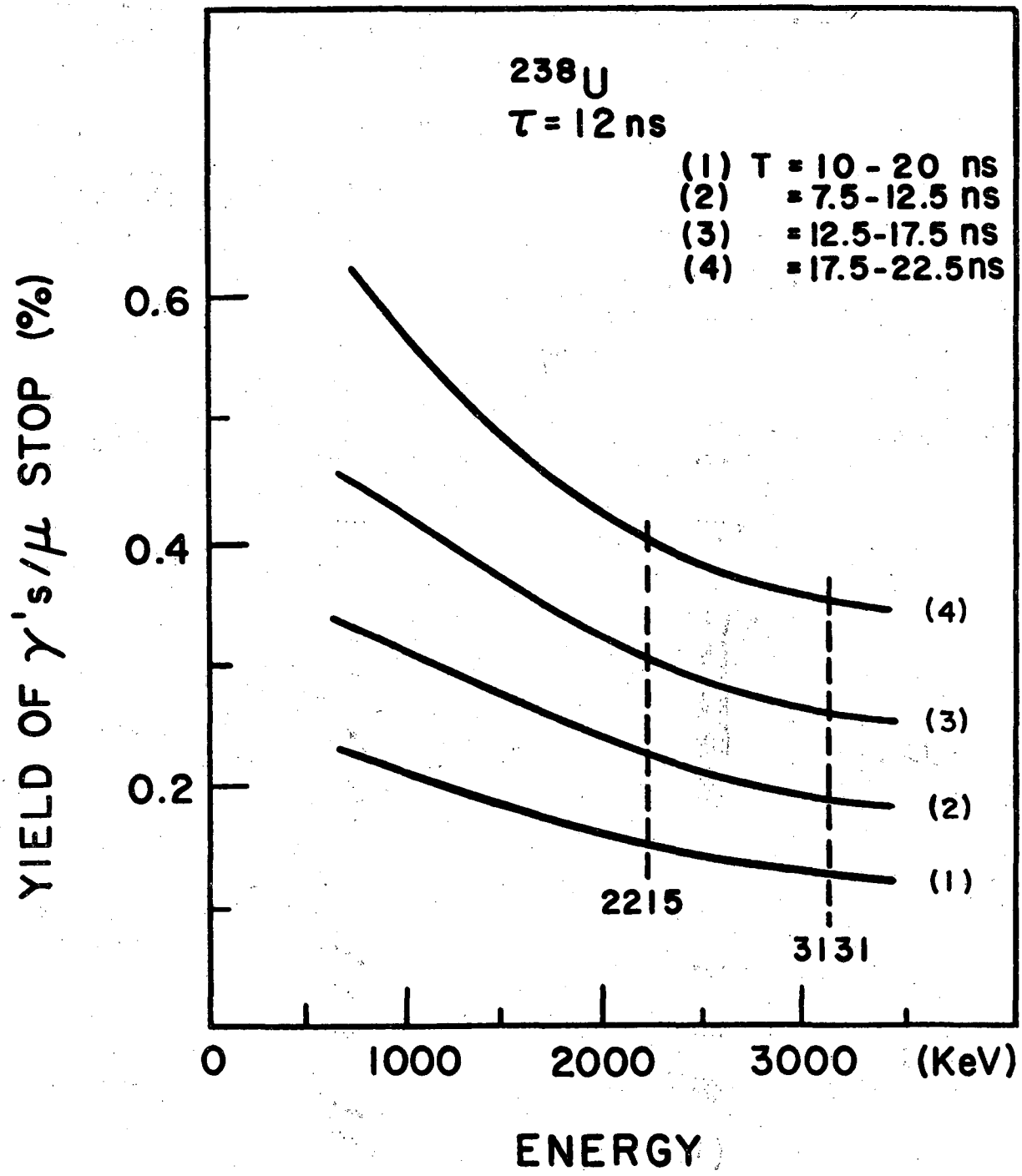


Fig. 5-10 Sensitivity for detecting a back-decay gamma ray of 12 ns mean-life in different time windows

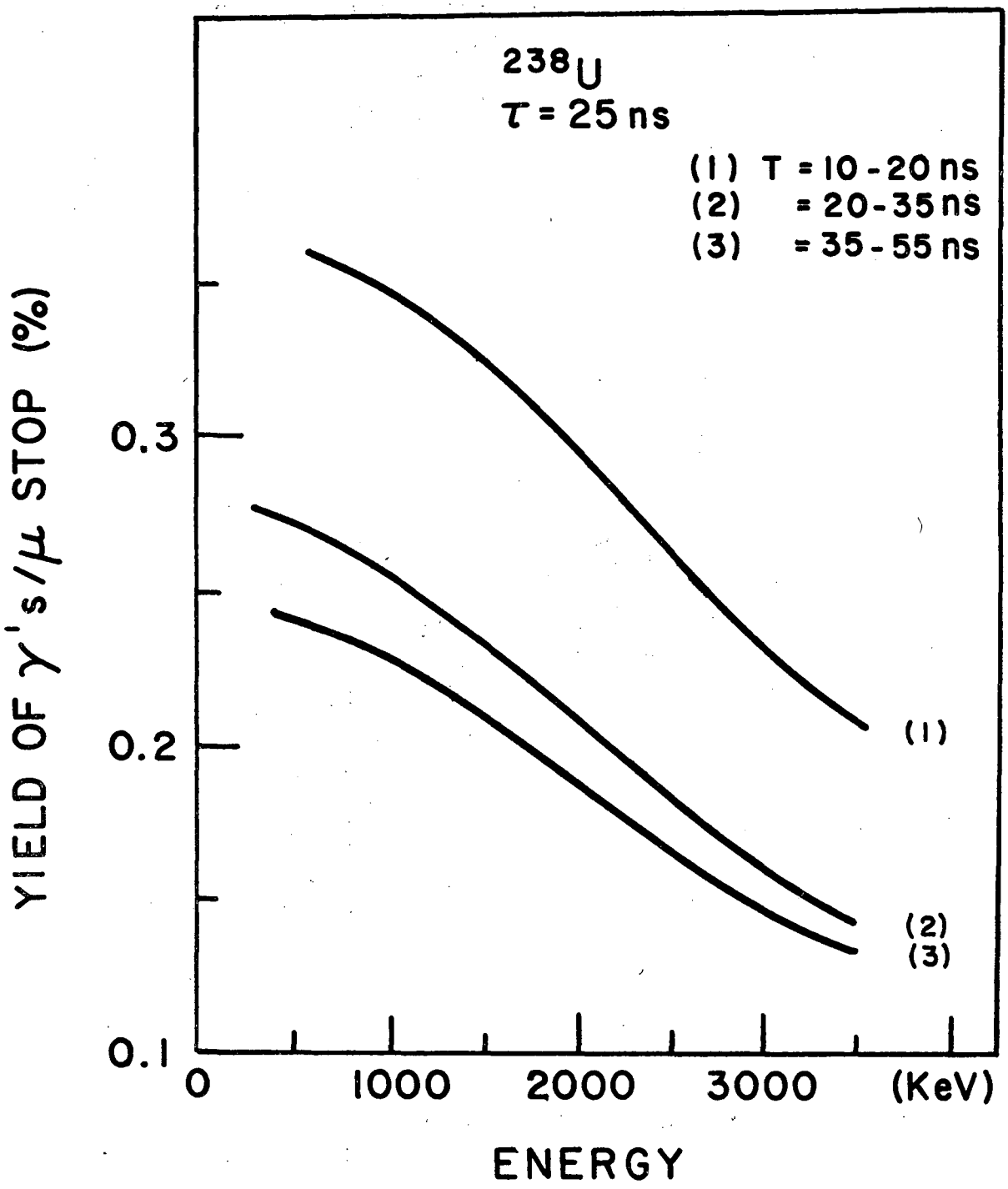


Fig. 5-11 Sensitivity of 3 different time windows for detecting a gamma back-decay of 25 ns life time.

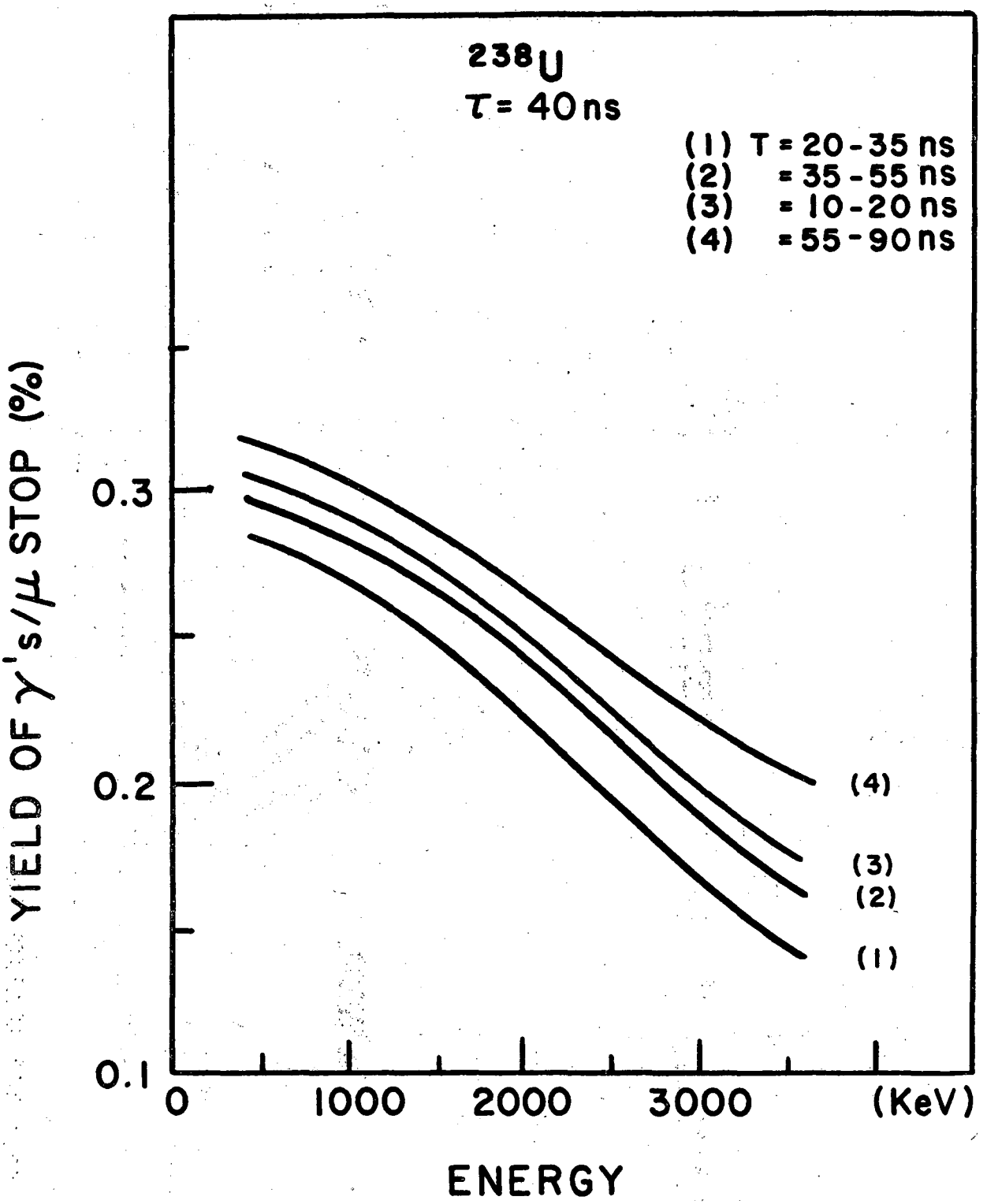


Fig. 5-12 Sensitivity of 4 different time windows for detecting a gamma back-decay of 40 ns mean-life.

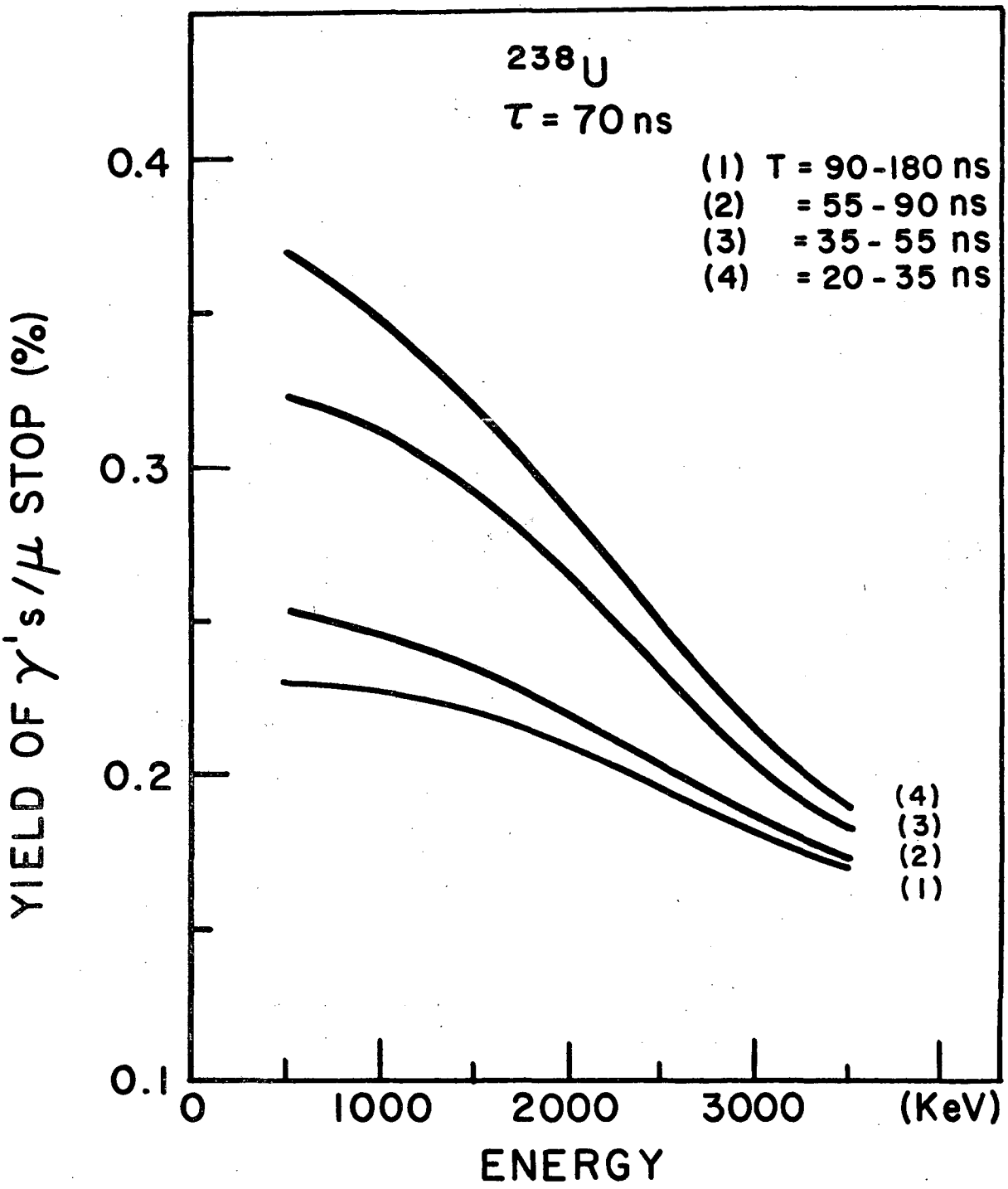


Fig. 5-13 Sensitivity of four different time windows for detecting a gamma back-decay of 70 ns mean-life.

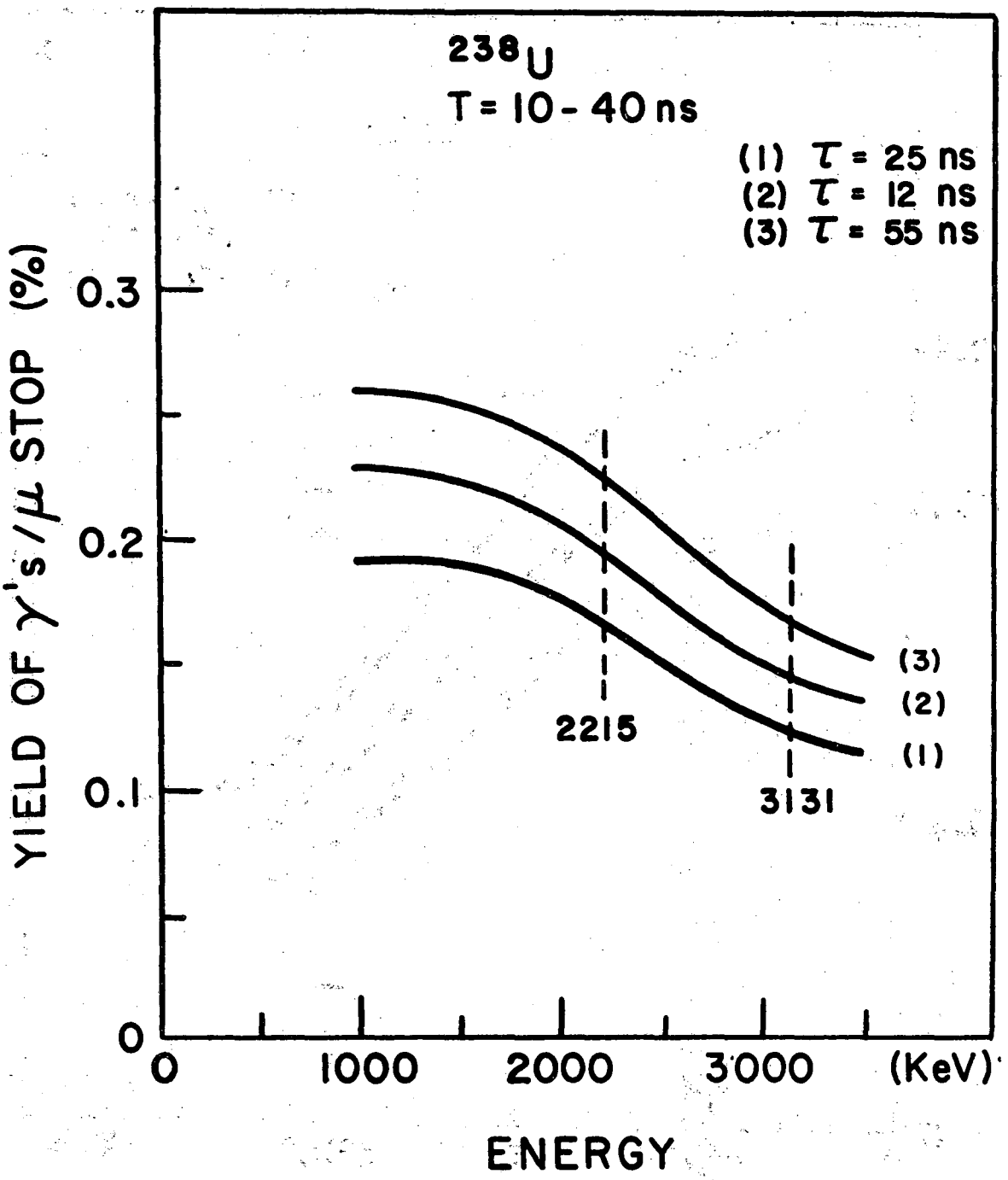


Fig. 5-14 Sensitivity of 10-40 ns time window for detecting gamma back-decays with different mean-lives.

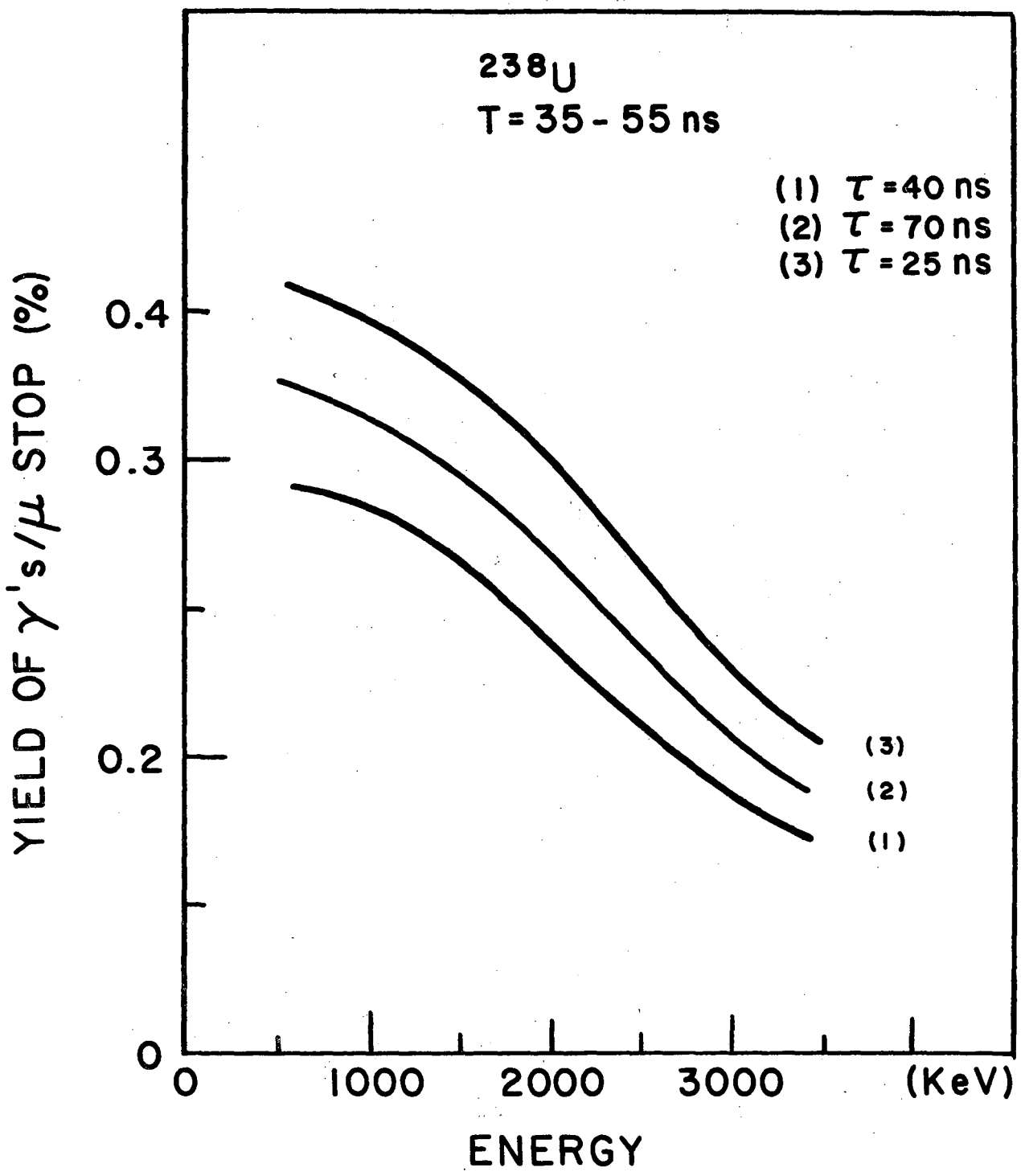


Fig. 5-15 Sensitivity of 35-55 ns time window for detecting gamma back-decays with different mean-lives.

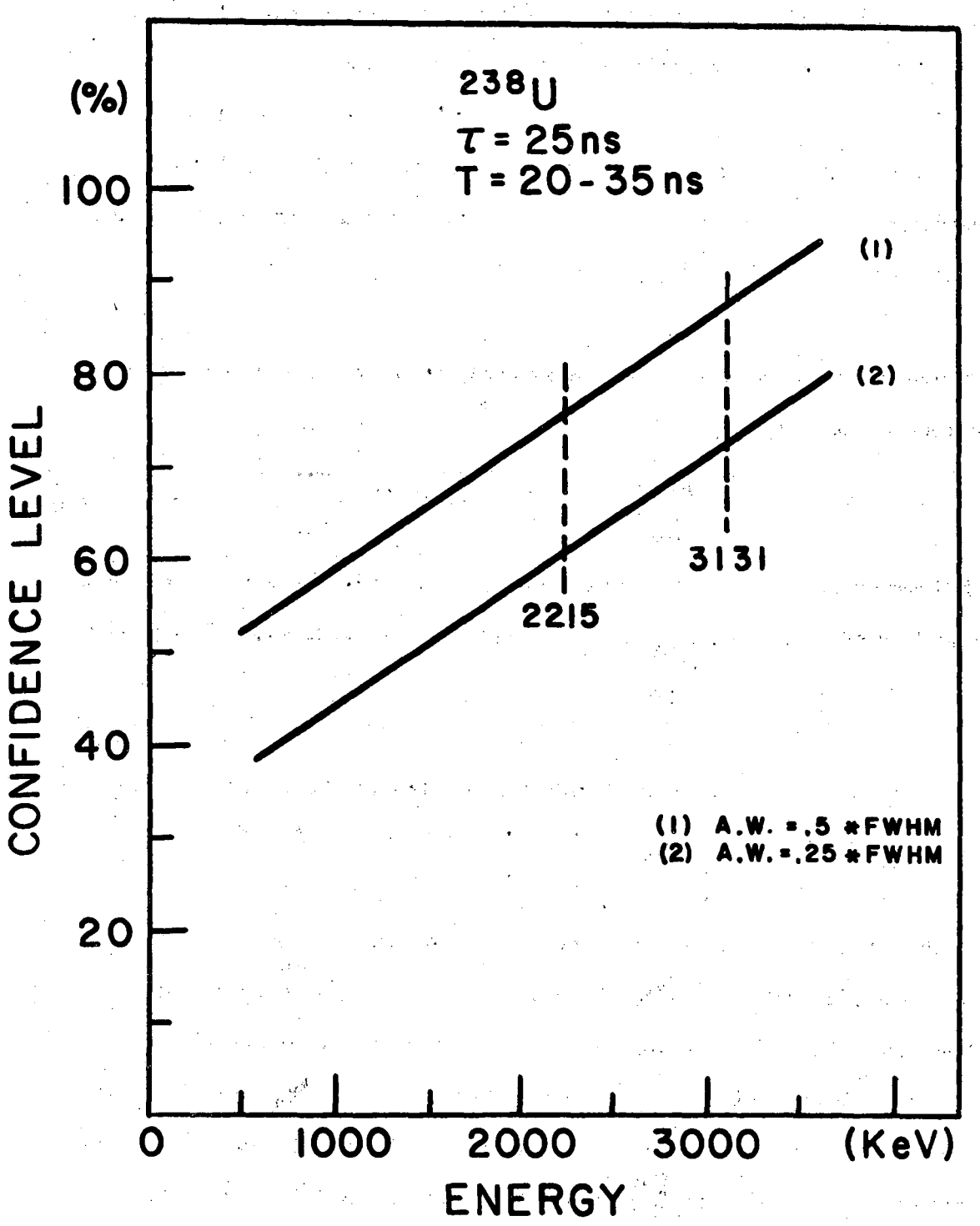


Fig. 5-16 Variation of confidence level with energy for 20-35 ns time window to detect a gamma ray of 25 ns mean-life at a yield limit of 0.2% per μ-stopping.

windows in which the same gamma ray is not observed. Therefore, for the transitions which did not show up in any of our spectra (time windows), we should be able to formulate an "overall confidence level" from the ones found for the individual time windows at a certain yield. Let us denote the confidence level at a yield of $Y_\gamma$ for a certain transition in the iSupth time window searched as $C_i$. Thus, the probability of non-observation of the same gamma ray in that time window would be

$$P_i = 1 - C_i \tag{5-1}$$

Then the probability that the same transition would appear in none of the m successive time windows searched is given by

$$P_{n.o.} = \prod_{i=1}^{m} P_i = (1 - C_1)(1 - C_2)...(1 - C_m) \tag{5-2}$$

The " overall confidence level" is in fact the probability that this transition with the specified yield $Y_\gamma$ appears in at least one of the m time windows under consideration and is expressed by

$$C_L = 1 - P_{n.o.} = 1 - (1 - C_1)(1 - C_2)...(1 - C_m) \tag{5-3}$$

This confidence level can also be interpreted as "defining the probability of that transition to have an upper limit yield ($Y_{u.l.}$) equal to $Y_\gamma$." The "overall confidence level" for the proposed shape isomeric back-decay transitions with $\tau$ = 12 nsec at energies of 2215 and 3131 kev were calculated by considering three 5 nsec wide delayed time windows starting at T = 7.5 nsec after muon stop. The results for $Y_{u.l.}$ = .15% and $Y_{u.l.}$ = .2% per $\bar{\mu}$ stop are given in Table V-1. A similar calculation was performed for a 25 nsec transition using the corresponding confidence levels of the "group 2" spectra (10→20 NS, 20→35 NS, 35→55 NS, and 55→90 NS). The results for $Y_{u.l.}$ = .1, shown in Fig. 5-17 For each value of $Y_{u.l.}$ two curves corresponding to two different choices of acceptance window (A.W. defined in section 5.2.2) are plotted.

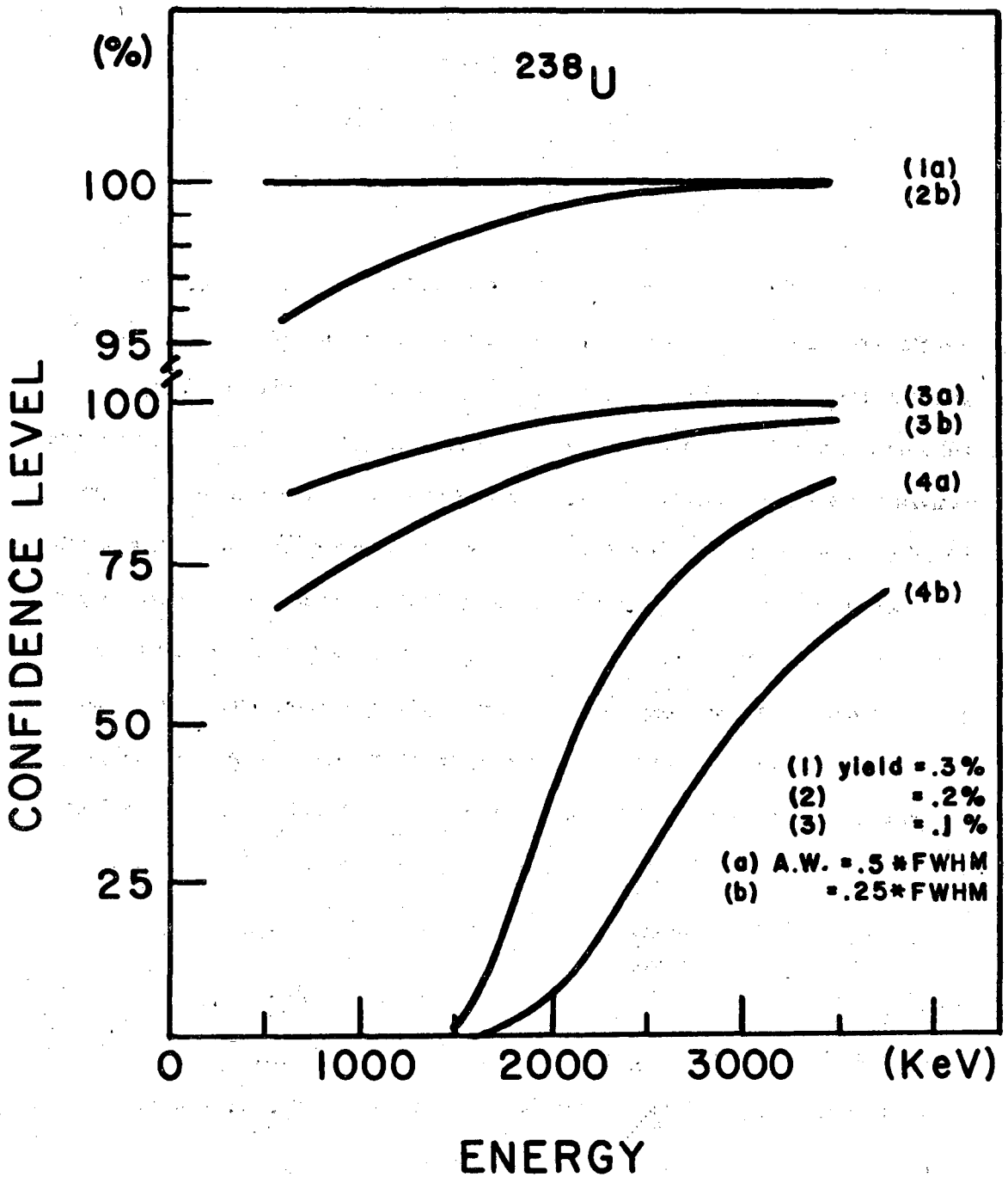


Fig. 5-17 Variation of the overal confidence level with energy for a gamma back-decay with assumed mean life of 25 ns.

Table V-1

| $Y_{u.p.}(/\bar{\mu}$ stop) | .15% | .2% |
|---|---|---|
| $C_{L(2215kev)}$ | 75% | 85% |
| $C_{L(3131kev)}$ | 80% | 95% |

As seen from this figure, the upper limit yield of .3% (per $\bar{\mu}$ stop) has a confidence level of more than 95% over the entire energy range, and even the .2% upper limit yield, in the vicinity of the proposed back-decay energies has a confidence level of about 90%. Earlier in this chapter we talked about the possibility of some spurious peaks being accepted as real spectral peaks by the analyzing program. Therefore it is a legitimate question for the user of that program to ask himself "what would be the chance that a peak accepted by the program would be a fake one?" It is possible to test each spectrum for fake peaks by the statistical method described in the previous section. However, for this case the generated spectrum will not carry any constructed peak on it and consists solely of the background envelope of the real spectrum under test and randomized in the same way and then analyzed by the program. Supposing that in analyzing this spectrum the program accepts $N_F$ peaks over the $N_i$ channels wide range of interest. The probability that an accepted fake peak appears in the channel interaction between x and $x + \Delta x$ would be equal to $\frac{N_F \cdot \Delta x}{N_c}$. In order to obtain a statistically reliable result this procedure should be repeated for the same spectrum for a large number of different random number seeds and the mean number of fake peaks $\bar{N}_F$ be found. Consider the case that a peak appears in K successive energy spectra, not exactly but within a certain precision $\Delta x$ channels, in equal channel numbers, then the probability for that peak to be a fake one is

$$P_F = \prod_i^k \left(\frac{\bar{N}_{Fi} \cdot \Delta n}{N_c}\right) \tag{5-4}$$

where $\bar{N}_{Fi}$ is the mean number of fake peaks accepted by the program in the test analysis of the

$i^{th}$ spectrum. The test was performed for a large number of spectra. Values between 30 and 70 were found for $\bar{N}_{Fi}$ of different spectra. In all these tests a channel number range of 1500-3500 was studied. Now let's consider our criteria for real peaks which required a peak to appear in at least three independent time windows within a precision of 3 channel. With the results of the tests performed, we are able to estimate the confidence of this criteria. This confidence is in fact the probability that the criteria would not admit fake peaks to be accepted as real ones and is equal to $P_R = 1 - P_F$, where $P_F$ is calculated from the expression (5-4) for the three time windows. The minimum confidence calculated on the basis of these results would be

$$(P_R)_{min} = 1 - (P_F)_{max} = 1 - (\frac{70 \times 3}{2000})^3 \approx 99\% \qquad (5\text{-}5)$$

which indicates that the undertaken criteria for accepting real peaks was in fact a very reliable one.

# CHAPTER 6

# CONCLUSION

Searching for back-decay gamma rays from shape isomeric states in U isotopes, at an effective sensitivity of about 0.15% per $\bar{\mu}$-stop in the target, we did not observe any candidate for the case of $^{236}$U and $^{238}$U. For $^{235}$U, we did not have enough counts in the delayed spectra to make a statistically satisfactory analysis.

In the case of $^{238}$U, our finding is at variance with the experimental result of a CERN group (Fromm *et al.* ,1976). They reported two delayed gamma rays at energies of 2215 and 3131 kev. These gamma rays were ascribed to transitions from an energetically shifted (due to muon binding energy) shape isomeric state, with an excitation energy of 3177 kev and life time of 12 ns, to the $2^+$ levels of the $\gamma$-vibrational and ground state band. A systematic search using the GAMANL peak analyzing program, failed to yield any delayed gamma rays over the energy range of 1.5 to 4.5 Mev and life time range of 12 to 70 ns. The previously mentioned .15% yield per muon stop is for the energy range of 2 to 3.5 Mev and should be compared with the .5% value given for the yield of the 2215 and 3131 kev gamma rays by Fromm *et al.* A hand search of the delayed spectra produced four known gamma rays at lower energies and with yields higher than but close to .15% per muon stop. In addition, it found two possible short lived ($\tau$ = 28ns) still unidentified $\gamma$-rays at energies of 2123 and 2693 kev at yields of .19% and .15% per $\mu$-stop, respectively. There are some other unidentified gamma rays with yields as low as .07% per $\mu$-stop. The energies of these gamma rays could not be related to a possible level scheme for transitions from a hypothetically excited shape isomeric state in $^{238}$U. The yield limit for the back decay gamma branch ($Y_\gamma$) can be translated into an upper limit for the probability of the shape isomer excitation (P) through the muon radiationless atomic transition, using the relation;

$$P = Y_\gamma / \left( \frac{\lambda_\gamma^{\,i}}{\lambda_c^{\,i} + \lambda_\gamma^{\,i} + \lambda_f^{\,i}} \right)$$

where $\lambda_c^{\,i}$ is the capture rate, $\lambda_\gamma^{\,i}$ is the back-decay rate, and $\lambda_f^{\,i}$ is the fission rate from the isomeric state. Substituting some typical values for the decay rates and using the value of $Y_\gamma = 0.15\%$ per $\mu^-$-stop, we find that $P \leq 0.15/(0.95) \leq 0.16\%$ per $\bar{\mu}$-stop. The radiationless transitions which are responsible for the excitation of the shape isomer amount to about 25% of the muon cascade (Teller & Weiss, 1979; Balatz *et al.* 1960, 1961). Therefore, the above upper-limit excitation probability (.16%) converts to an upper-bound value of about $6 \times 10^{-3}$ for the feeding probability of the shape isomeric state through radiationless excitations. This feeding probability may be compared with the corresponding value in direct reactions, called "isomer ratio" and defined as: the cross section for isomer production divided by the cross section for formation of the normally deformed nucleus by the same reaction. The value for the isomer ratio for $^{238}U$ in a (d,pn) reaction is given to be: 5 to $25 \times 10^{-4}$ (Russo *et al.* 1974), which is on the order of, or up to an order of magnitude smaller than, our upper-limit value of $6 \times 10^{-3}$ for the shape isomer feeding probability by the muon radiationless transitions. But, since in our experiment we have not found any real value for the probability of the shape isomer population--rather we have set an upper limit -- the real value was thought to be comparable or even less than the direct reaction isomer ratio. Since the radiationless transitions, in contrast with the direct reaction excitations, involve single-energy excitation with an energy comparable to the first barrier height (in $^{238}U$), it was thought to be more efficient in populating the states in the second well. Our upper-limit value is much smaller than the value that Bloom (1974) estimated for the isomer excitation by the muon radiationless processes. The CERN group (Fromm *et al.* 1976) inferred from their results an isomeric state excitation probability of 0.1 which they found to be very large compared with the corresponding values of $10^{-4}$ to $10^{-5}$ from neutron induced excitation or charged particle reactions. They speculated that "the resonance excitation of states in the second minimum via vibrational states in the first well" may be responsible.

Similar negative results were obtained for muonic $^{236}U$ which has not been studied before experimentally. A recent experiment (Butler *et al.* ,1980) using $^{235}U(d,p)\,^{236}U$ reaction to search for the gamma branch of such an isomer also failed to produce any positive result. In this sense our $^{236}U$ experimental result is consistent with their negative finding. Considering that the barrier parameters of $^{236}U$ and $^{238}U$ are very similar and the perturbations due to muon binding energy for the two isotope are not significantly different, from the expression for P given above we may infer that the upper limit for production of the shape isomeric state through the muon radiationless transition in $^{236}U$ is approximately that of $^{238}U$. Nevertheless, it remains a puzzle why the shape isomer in $^{238}U$ (Russo *et al.* 1974) has a $\gamma$-branch of $50 > \lambda_{i\gamma} / \lambda_{if} > 20$ while the shape isomer in $^{236}U$ (Butler *et al.* 1981) appears to have an upper-limit $\gamma$-branch of $\lambda_{i\gamma} / \lambda_{if} < 1.5$ for a single high energy transition (2 to 3 Mev) and $\lambda_{i\gamma} / \lambda_{if} < 4.5$ for a cascade of low-energy $\gamma$-transitions.

In the list of our observed delayed transitions, both for $^{236}U$ and $^{238}U$, there are several gamma rays which are not accounted for and not reported previously. The intensities of most of these gamma rays are within the range of 0.1 to 0.2 % per muon stop.

Prompt spectra included muonic x-rays, their single-escape and double-escape peaks, as well as sums for the transitions between higher orbits. The measured energies and intensities of the x-rays are in good agreement with other experimental and calculated results. Our experimental K x-rays from $^{236}U$ and $^{238}U$ give an isotope shift of about 20 kev. The x-ray spectrum of $^{236}U$ has not been previously reported. The energies of the L, M, and N x-rays for the two even-even isotopes are very close, not distinguishable within experimental errors. The $^{235}U$ x-ray spectrum shows little detailed relationship to those of the other two isotopes. This is understandable in terms of $^{235}U$ being an odd-even nucleus and having a completely different nuclear level structure which results in a different hyperfine splitting of the muonic levels.

## REFERENCES

N. M. M. Al-Qazzaz, G. A. Beer, G. R. Mason, A. Olin, R. M. Pearce, D. A. Bryman, J. A. MacDonald, J. M. Poutissou, P. A. Reeve, M. D. Hasinofff and T. Suzuki, Nucl. Inst. and Meth. 179, 35 (1980).

B. Bach, O. Hanson, H. C. Britt, and D. Garret, Physics and Chemistry of Fission 1973, (IAEA, Vienna, 1974), Vol. 1, p. 3.

B. Bach, O. Hanson, H. C. Britt, and D. Garret, Phys. Rev. C9, 1924 (1974).

H. Bartsch, W. Gunther, K. Huber, V. Kneissl, H. Krieger, and H. J. Alaier, Nucl. Phys. A306, 29-37 (1978).

M. J. Balatz, L. N. Kondratiev, L. G. Landsberg, P. T. Lebedev, Y. V. Obukhov, and B. Pontecorvo, JETP 38, 1715 (1960).

M. Y. Balatz, L. N. Kondratiev, L. G. Landsborg, P. J. Lebedev, B. V. Obukhov, and B. Pontecorva, Soviet Physics JCTP 12, 813 (1961).

M. Brach, J. Damgaard, H. C. Pauli, A. S. Jensen, V. M. Strutinsky, C. Y. Wang, Rev. Mod. Phys. 44, 320 (1972).

S. Bjornholm and L. E. Lynn, Rev. Mod. Phys. 52, 725 (1980).

H. C. Britt, M. Balsterli, J. R. Nix, Phys. Rev C7, 801 (1973). S. D. Bloom, Phys. Lett. 48B, 470 (1974).

H. C. Britt, S. C. Burnett, B. H. Erkkila, J. E. Lynn, and W. E. Stern, Phys. Rev. C4, 1444 (1971).

P. A. Butler, R. Daniel, A. D. Irving, T. P. Morrison, P. J. Nolan, and V. Metag, J. Phys. G:Nucl. Phys. 6, 1165 (1980).

D. A. Close, J. J. Malamfy, and J. P. Davidson, Phys. Rev. C17, 1433 (1978).

J. D. Cramer and J. R. Nix, Phys. Rev. C2, 1048 (1970).

J. Diaz, S. N. Kaplan, B. MacDonald, and R. V. Pyle, Phys. Rev. Lett. 3, 234 (1959).

R. Engfer, H. Schneuwly, J. L. Vuilleumier, H. K. Walter and A. Zehnder, Atomic Data and Nucl. Data Tables 14, 509 (1974).

W. D. Fromm, H. G. Ortlepp, S. M. Polikanov, V. Schmidt, G. N. Zorin, R. Arlt, and G. Musiol, Nucl. Phys. A278, 387 (1977).

E. B. Gai, A. B. Ignatyuk, N. C. Robotnov, G. N. Smyrenkin, Proc. of 2nd Int. Symp. on Physics and Chemistry of Fission, Vienna, 1969, p. 337.

D. Z. Ganzorig, P. G. Hansen, T. Johansson, B. Jonson, J. Konijin, T. Krogulski,

B. Goulard and H. Primakoff, Phys. Rev. C10, 2034 (1974).

L. V.Groshev et al., Nucl. Data Table 5, 416 (1969).

D. Habs, V. Metag, H. J. Specht, G. Ulfort, Phys. Rev. Lett. 38, 387 (1977).

J. Haderman, Phys. Lett. 67B, 35 (1977).

T. Inouye, T. Harper, and N. C. Rasmussen, NIM 67, 125 (1969).

D. L. Hill and J. A. Wheeler, Phys. Rev. 89, 1102 (1953).

D. Hobs, M. Just, V. Metag, E. Mosler, B. Neumann, P. Paul, Singer, H. J. Specht, and G. Vefert, 1975 Jahresbericht Max Plank-Institute fur Kernphysik (Heidelberg) p. 56.

T. Johansson, S. G. Nilsson, and Z. Szymanski, Ann. Phys. 5, 377 (Paris, 1970).

W. John et al., Phys. Rev. C2, 1451 (1970).

S. N. Kaplan, J. A. Monard, and S. Nagamiya, Phys. Lett. 64B, 217 (1976).

A. M. Khan and J. W. Knowles, Nucl. Phys. A179, 333 (1972).

H. J. Krappe and J. R. Nix, Physics and Chemistry of Fission (IAEA, Vienna, 1974), Vol. I, p. 271.

N. Lark, G. Sletter, J. Pedersen, and S. Bjornholm, Nucl. Phys. A139, 481 (1969). G. Leander and P. Moller, Phys. Lett. 52B, 245 (1975).

G. Leander and P. Moller, Phys. Lett. 57B, 245 (1975).

C. Michael Lederer and Virginia S. Shirley, *Table of Isotopes* (Wiley, New York, 1978), seventh edition.

K. P. Lohs, G. Wolschin, and J. Hufner, Nucl. Phys. 28, 177 (1960).

W. R. Mc Murray and I. J. Van Heerden, Z. Phys. 253, 289 (1972).

V. Metag, G. Sletten, Nucl. Phys. A282, 77 (1977).

A. Michaudon, in Proc. Int. Conf. on The Interaction of Neutrons with Nuclei, CONF-760715, Vol. 1, p. 641 (1976).

E. Migneco and J. P. Theobald, Nucl. Phys. A112, 603 (1968).

P. Moller and J. R. Nix, Physics and Chemistry of Fission, 1973, Vol. 1, p. 103 (1973) (IAEA, Vienna, 1974).

B. R. Mottelson and S. G. Nilsson, Mat. Fys. Medd. Dan. Vid. Selsk. 1, no. 8 (1959).

W. D. Myers and W. J. Swiatecki, Ann. Phys. 55, 395 (1969).

W. D. Myers and W. J. Swiatecki, UCRL report 19543 (1970).

W. D. Myers and W. J. Swiatecki, LBL report 1957 (1973).

W. D. Myers and W. J. Swiatecki, Ann. Phys. 84, 186 (1974).

A. I. Muhkin, M. J. Balatz, L. N. Kondratiev, L. O. Landsbert, P. I. Lebedev, Y. V. Chukhow, and B. Pontecorvo, Proc. of 1960 Ann. Int. Conf. on High Energy Physics, Rochester, August 25-September 1 (Interscience Publishers Inc., New York, 1960) p. 550.

S. G. Nilsson, Nucl. Phys. A140, 275 (1970).

S. G. Nilsson, C. F. Tasug, A. Sobeczewski, Z. Szymanski, S. Wycech, C. Gustafson, I. Lam, P. Moller, and B. Nilsson, Nuc. Phys. A131, 1 (1969).

J. R. Nix, Ann. Rev. Nucl. Sci. 22, 65 (1972).

J. R. Nix and G. E. Walker, Nucl. Phys. A132, 60 (1969).

J. Pedersen and B. D. Kuzminov, Phys. Lett. 29B, 176 (1969).

J. Pilochi, Z. Sujkowski, and M. Zielinska-Pfahio, Phys. Lett. 42B, 415 (1972).

S. M. Polikanov and G. Sletten, Nucl. Phys. A151, 656 (1970).

F. A. Rickey, E. T. Jurney and H. C. Britt, Phys. Rev. C5, 2082 (1972).

P. A Russo, J. Pedersen, and F. V. Vandenbosch, Nucl. Phys. A240, 13 (1975).

W. V. Schroder, W. W. Wilcke, M. W. Johnson, D. Hilscher, J. R. Huizenga, J. C. Browne, and D. G. Perry, Phys. Rev. Lett. 43, 672 (1979).

D. K. Sood and N. Sarma, Nucl. Phys. A151, 532 (1970).

H. J. Specht, J. Weber, E. Konechy, D. Heunemann, Phys. Lett. B41, 43 (1972).

Hans J. Specht, Rev. Mod. Phys. 46, 773 (1974).

V. M. Strutinsky, Sov. J. Nucl. Phys. 3, 449 (1966).

V. M. Strutinsky, Nucl. Phys. A95, 420 (1967).

E. Teller and M. S. Weiss, Lawrence Livermore Laboratory Report UCRL-83616 (1979)

L. E. Temple, LBL-781, p. 44 (1972).

C. F. Tsang and S. G. Nilsson, Nucl. Phys. A140, 275 (1970).

R. Vandenbosch and J. R. Huizenga, Nuclear Fission, (Academic Press, New York, 1973).

R. Vandenbosch, Ann. Rev. Nucl. Sci. 27, 1 (1977).

W. W. Wilche, M. W. Johnson, W. V. Schroder, J. R. Huizenga, and D. G. Perry, Phys. Rev. C18, 1452 (1978).

K. L. Wolf, R. Vandenbosh, A. Russo, M. K. Mehta, and C. R. Rudy, Phys. Rev. C1, 2096 (1979).

C. Y. Wong and J. Bang, Phys. Lett. B29, 143 (1969).

# *APPENDIX A*

## *LISTING OF THE FORTRAN SUBROUTINES USED IN MODIFICATION OF THE PHA PROGRAM*

```
C      CLEAR A HISTOGRAM FROM FILE DK TEMP.SP
C     SET UP DISK HISTOGRAM SPACE AND POINTERS
C
C     ***************************************************
C
      SUBROUTINE SETXM(NPAGE,IERR)
      INTEGER FILID(5),BUF(2048)
      INTEGER ANS
      COMMON/DKUP/LPTR,NBUF,FILID
      DATA FILID/'SY','0 ','TM','P.','SP'/
      LPTR=1                    !SET POINTER TO 1
      IERR=0
      LHIST=32*NPAGE            !HISTOGRAM LENGTH IN WORDS
      NBUF=NPAGE/64
D     TYPE*,'NUMBER OF RECORDS =',NBUF
      TYPE *,'RESTOR OLD TMP.SP FILE ?....  YES (1) ,  NO (0) '
      ACCEPT 20,ANS
      IF(ANS.EQ.1)GOTO 35
20    FORMAT(1I)
      OPEN(UNIT=8,NAME='SY0 TMP.SP',ACCESS='DIRECT',BLOCKSIZE=4096,
     1RECORDSIZE=1024,ERR=10,INITIALSIZE=NBUF)
      GO TO 50
35    OPEN(UNIT=8,TYPE='OLD',NAME='SY0 TMP.SP',ACCESS='DIRECT'
     1,BLOCKSIZE=4096,RECORDSIZE=1024,ERR=10,INITIALSIZE=NBUF)
      GOTO 90
50    DO 5 I=1,2048
      BUF(I)=0
```

```
5    CONTINUE
     DO 8 J=1,NBUF
     IRC=J
     WRITE (8'IRC,ERR=10)BUF
8    CONTINUE
10   CALL ERRSNS(IERR)
90   RETURN
     END
```

```
C      DISK HISTOGRAM UPDATING
C
C      ***********************************************
C
       SUBROUTINE INCXM(IB,ID,IERR)
       INTEGER BUF(2048),LIST(4096)
C      BUF IS BUFFER FOR DISK HISTOGRAMS AND LIST CONTAINS STARTING
C      PAGE ADDRESS ANND DISPLACEMENNT OF CHANNEL TO BE INCREMENTED
       COMMON/DKUP/LPTR,NBUF,FILID
       IF(ID.EQ.-1)GO TO 50          !TO EMPTY LAST BUFFER
       KD=32*IB+ID-1
       K=MOD(KD,2048)                !POINTER TO DISPLACEMENT IN THE BUFFER
       LIST(LPTR)=1+KD/2048          !POINTER TO BUFF NO.
       LIST(LPTR+1)=K+1
```

```
      LPTR=LPTR+2
      IF(LPTR.LE.2048)RETURN        !LIST NOT FULL
C     DISK HISTOGRAM UPDATE
50    LLIST=LPTR-2
      IF(LLIST.LE.0)RETURN
      DO 200 J=1,NBUF               !LOOP ON DISK BUFFERS
      IUPD=0
      I=1
      M=-1
C     LOOP THROUGH LIST
100   IF(LIST(I).NE.J)GO TO 150
      IF(LIST(I).EQ.M)GOTO 120
      IREC=J
      IF(IUPD.EQ.0)READ(8'IREC,ERR=250)BUF
120   M=LIST(I)
      BUF(LIST(I+1))=BUF(LIST(I+1))+1   !INCREMENT HISTOGRAM
      IUPD=1
      IF(I.GE.LLIST)GO TO 160         !NO MORE DATA FOR THIS BUFFER
      LIST(I)=LIST(LLIST)             !REPLACE WITH LAST LIST ENTRY
      LIST(I+1)=LIST(LLIST+1)
      LLIST=LLIST-2                   !SHORTEN LIST
      GO TO 100
150   I=I+2                           !NEXT ENTRY
      IF(I.LE.LLIST)GO TO 100
160   IF(IUPD.EQ.1) WRITE(8'IREC,ERR=250)BUF  !WRITE TO DISK BUFFER
200   CONTINUE
      LPTR=1
```

```
250   CALL ERRSNS(IERR)
      RETURN
      END



C     WRITE SPECTRUM  ON DK TEMP.SP
C
C     ************************************************
C
      SUBROUTINE PUTXM(IB,ID,JHIST,NWCN,IERR)
      INTEGER BUF(2048)
      DIMENSION JHIST(1024)
      COMMON/DKUP/LPTR,NBUF,FILID
      KD=32*IB+ID-1
      NHSC=MOD(KD,2048)+1                !DISPLACEMENT IN THE BUFF.
      NHEC=NHSC+NWCN-1
      IREC=1+KD/2048              !RECORD NO.
      J=0
      M=NHEC
10    READ(8'IREC,ERR=20)BUF
      IF(NHEC.GE.2048)NHEC=2048
      DO 15 I=NHSC,NHEC
      J=J+1
      BUF(I)=JHIST(J)
```

```
15    CONTINUE
      WRITE(8'IREC,ERR=20)BUF
      IF(M.LE.2048)RETURN
      IREC=IREC+1
      NHSC=1
      NHEC=M-2048
      M=0
      GO TO 10
20    CALL ERRSNS(IERR)
      RETURN
      END


      SUBROUTINE CLRXM(IB,ID,NWCN,IERR)
C
C     ************************************************
C
      INTEGER BUF(2048)
      COMMON/DKUP/LPTR,NBUF,FILID
      KD=32*IB+ID-1
      NHSC=MOD(KD,2048)+1          !DISPLACEMENT IN THE BUFFER
      NHEC=NHSC+NWCN-1
      IREC=1+KD/2048
      M=NHEC
```

```
5     READ(8'IREC,ERR=20)BUF
      IF(NHEC.GE.2048)NHEC=2048
      DO 10 I=NHSC,NHEC
      BUF(I)=0
10    CONTINUE
      WRITE(8'IREC,ERR=20)BUF
      IF(M.LE.2048)RETURN
      IREC=IREC+1
      NHEC=M-2048
      NHSC=1
      M=0
      GO TO 5
20    CALL ERRSNS(IERR)
      RETURN
      END



C     FETCH BLOCK FROM DISK HISTOGRAM SPACE
C
C     ******************************************************
C
      SUBROUTINE GETXM(IB,ID,IHIST,NWCN,IERR)
      INTEGER BUF(2048),IHIST(1024)
      COMMON/DKUP/LPTR,NBUF,FILID
```

```
      KD=32*IB+ID-1
      NHSC=MOD(KD,2048)+1          !DISPLACEMENT IN THE BUFFER
      NHEC=NHSC+NWCN-1
      IREC=1+KD/2048
C     TYPE*,'IREC.....=',IREC
      J=0
      M=NHEC
10    READ(8'IREC,ERR=20)BUF
      IF(NHEC.GE.2048)NHEC=2048
      DO 15 I=NHSC,NHEC
      J=J+1
      IHIST(J)=BUF(I)
15    CONTINUE
      IF(M.LE.2048)RETURN
      IREC=IREC+1
      NHSC=1
      NHEC=M-2048
      M=0
      GO TO 10
20    CALL ERRSNS(IERR)
D     TYPE*,'LAST VALUE OF IREC ,IB =',IREC,IB
      RETURN
      END
```

```
C                    OPEN TAPE MT1
C  THE FOLLOWING SUBROUTINES PERFORM ALL TAPE I/O PROCESSES NECESSARY
C  FOR PROGRAM PHA.
C
C     ***************************************************************
C
      SUBROUTINE MTOPEN (IRCODE)
      DIMENSION ISB(2)
      IOATT = "1400          !ATTACH CODE

C     CALL ASNLUN (10,MT,1,IDS)       !ASSIGN UNIT 10 TO MT1
C     IF (IDS. NE. 1) GOTO 10
      CALL WTQIO (IOATT,10,1,,ISB)          !ATTACH P
      IRCODE = ISB (1)
      IF (ISB(1).NE.1) GOTO 20
      RETURN
10    IRCODE = IDS
      TYPE *,'FAILURE IN ASSIGN!'
      RETURN
20    TYPE *,'FAILURE IN ATTACH  !'
      RETURN
      END

C                    CLOSE TAPE MT1
C     ***********************************************
C
      SUBROUTINE MTCLOS (IRCODE)
```

```
C
      DIMENSION ISB (2)
      IODET = "2000          !DETACH CODE
C
      CALL WTQIO (IODET,10,1,,ISB)          !DETACH MT1
      IRCODE= ISB (1)
      IF (IRCODE .NE. 1) GOTO 5
      RETURN
5     TYPE *,'FAILURE IN DETACH!'
      RETURN
      END

                    READ DATA FROM TAPE
C     ************************************************
C
C
      SUBROUTINE MTGET (LENBUF,IBCNT,IRCODE)
C
      COMMON /REC/NDD(4096)
      DIMENSION  ISB (2), IADR (6)
      IORLB = "1000          !READ CODE
C
      IADR (2) = LENBUF + LENBUF
      CALL GETADR (IADR (1), NDD (1) )
C
      CALL WTQIO (IORLB,10,1,,ISB,IADR)          !READ BLOCK
      IRCODE = ISB (1)
```

```
      IBCNT = ISB (2)
      RETURN
      END

C                WRITE DATA INTO THE TAPE
C     ************************************************
C
C
      SUBROUTINE MTPUT0 (IBUF, IWCNT, IRCODE)
      DIMENSION IBUF (512), ISB (2), IADR (6)
      IOWLB = "0400          !WRITE CODE
C
      IADR (2) = IWCNT + IWCNT
      CALL GETADR (IADR (1),IBUF (1) )
C
      CALL WTQIO (IOWLB,10,1,,ISB,IADR)          !WRITE BLOCK
      IRCODE = ISB (1)
      RETURN
      END

C                MARK EOF ON THE TAPE
C     ************************************************
C
      SUBROUTINE MTMARK (IRCODE)
C
      DIMENSION ISB (2)
      IOEOF = "3000          !EOF CODE
```

```
C
      CALL WTQIO (IOEOF,10,1,,ISB)        !MARK EO
F
      IRCODE = ISB (1)
      RETURN
      END

C                REWIND THE TAPE
C     ***********************************************
C
      SUBROUTINE MTRWD0 (IRCODE)
C
      DIMENSION ISB (2)
      IORWD = "2400          !REWIND CODE
C
      CALL WTQIO (IORWD,10,1,,ISB)          !REWIND
      IRCODE = ISB (1)
      RETURN
      END

C                REWIND THE TAPE AND UNLOAD
C     ***********************************************
C
      SUBROUTINE MTRWD1 (IRCODE)
C
      DIMENSION ISB (2)
      IORWU = "2540          !REWIND CODE
```

```
C
      CALL WTQIO (IORWU,10,1,,ISB)          !REWIND AND UNLOAD
      IRCODE = ISB (1)
      RETURN
      END

C                BLOCK SPACE FORWARD
C     ***********************************************
C
      SUBROUTINE MTBLKF (NUMBER, BCOUNT, IRCODE)
C
      DIMENSION ISB (2)
      IOSPB = '2420                !BSF CODE
      NBS = NUMBER
C
      CALL WTQIO (IOSPB,10,1,,ISB,NBS)          !NBS FORWARD
      IRCODE = ISB (1)
      BCOUNT = ISB (2)             !NBS ACTUALLY FORWARDED
      RETURN
      END

C                BLOCK SPACE BACKWARD
C     ***********************************************
C
      SUBROUTINE MTBLKB (NUMBER, BCOUNT, IRCODE)
C
      DIMENSION ISB (2)
```

```
      IOSPB = "2420                !BLOCK SPACING CODE
      NBS = -NUMBER
C
      CALL WTQIO (IOSPB,10,1,,ISB,NBS)        !NBS BACKWARD
      IRCODE = ISB (1)
      BCOUNT = -ISB (2)            !NBS ACTUALLY BACKWARDED
      RETURN
      END

C               FILE SPACE FORWARD
C     ***********************************************
C
      SUBROUTINE MTFILF (NUMBER, BCOUNT, IRCODE)
C
      DIMENSION ISB (2)
      IOSPF = "2440                !FILE SPACING CODE
      NES = NUMBER
C
      CALL WTQIO (IOSPF,10,1,,ISB,NES)            !NES FORWARD
      IRCODE = ISB (1)
      BCOUNT = ISB (2)        !NO. OF EOF'S ACTUALLY FORWARDED
      RETURN
      END

C               FILE SPACE BACKWARD
C     ***********************************************
C
```

```
      SUBROUTINE MTFILB (NUMBER, BCOUNT, IRCODE)
C
      DIMENSION ISB (2)
      IOSPF = "2440                !FILE SPACING CODE
      NES = -NUMBER
C
      CALL WTQIO (IOSPF,10,1,,ISB,NES)    !NES BACKWARD
      IRCODE = ISB (1)
      BCOUNT = -ISB (2)          !NO. OF EOF'S ACTUALLY BACKWARDED
      RETURN
      END
```

# *APPENDIX B*

## *LEAST SQUARES FITTING PROGRAM USED FOR ENERGY CALIBRATION*

In an ordinary linear least squares fitting problem there is only one polynomial whose parameters are to be determined. In the special case that we are dealing with, there are two polynomials (eq.'s 4-8 and 4-9) which involve only one set of parameters. Applying least squares method to both of the polynomials results in the following sets of equations;

$$\frac{\partial}{\partial a_m} \sum_{i=1}^{N} (E_i - \sum_{m=o}^{3} a_m x_i^{\,m})^2 w_i = 0. \quad m=0,1,2,3 \tag{B-1}$$

$$\frac{\partial}{\partial a_m} \sum_{j=1}^{K} (\delta E_j - \sum_{m=o}^{3} a_m (x_j^{\,m} - x'^{\,m}_j))^2 w_j = 0. \quad m=1,2,3 \tag{B-2}$$

$w_i$ and $w_j$ are the statistical weights attributed to the $i^{th}$ and $j^{th}$ data points respectively, and there are 7 equations to be solved for only four unknowns ($a_o$.....$a_3$). One approach for obtaining a unique set of solutions from these two sets of equations appear to be solving them simultaneously and imposing the condition that the solutions of the two systems be equal.

However, the program CALIB presented in this appendix defines the least square fit problem in a matrix form appropriate to be solved by subroutine LINLSQ. This core library subroutine is designed in a form to be able to handle linear least squares problems more complex than a simple polynomial fitting. It also uses a "Householder transformation" method (G.H.Golub, 1965) which has proven to be numerically more stable than other common methods. The subroutine minimizes the following expression;

$$\sum_{I=1}^{M} w_I * [B_I - F(X_I, a_o, \ldots\ldots a_m)]^2 \tag{B-3}$$

where,

$$F(X_I,a_o,.....a_m) = \sum_{J=0}^{m} a_J * A(I,J) \qquad (B\text{-}4)$$

with,

$$A(I,J) = \begin{cases} x^J & \text{for } 1 \le I \le N \\ x^J - x'^J & \text{for } N+1 \le I \le N+K \end{cases} \qquad (B\text{-}5)$$

and

$$B_I = \begin{cases} E_I & \text{for } 1 \le I \le N \\ \delta E_I & \text{for } N+1 \le I \le N+K \end{cases} \qquad (B\text{-}6)$$

where w's, a's, x's, N, and K are the same as used in eq.'s B-1 and B-2. The listing of the FORTRAN program is given in the next page. The values for the channel numbers and the associated energies along with the attributed weights for all calibration points are read in as input data and the matrix A(I,J) is formed.

```
      PROGRAM CALIB(INPUT,OUTPUT,TAPE5=INPUT,TAPE6=OUTPUT)
     REAL C(40),E(40),C1(40),C2(40),W(40),A(40,4)
     REAL X(4),COVMAT(4,4),U(40),SIGMA(4)
     READ(5,300)NR
300  FORMAT(I10)
     WRITE(6,500)
500  FORMAT(1H1,//,20X,*INPUTDATA*,/////5X,*CHANNEL*,13X,*EN
    +ERGY*,14X,*WEIGHT*/)
     DO 20 I=1,10
     READ(5,1000)C(I),E(I),W(I)
     WRITE(6,1050)C(I),E(I),W(I)
20   IF(C(I).EQ.0.)GOTO 25
25   NP=I-1
     WRITE(6,600)
600  FORMAT(//5X,*CHANNEL1*,12X,*CHANNEL2*,12X,*ENERGYDIF*,11X,*WEIGHT*
    +/)
     DO 30 J=I,40
     READ(5,1100)C1(J),C2(J),E(J),W(J)
     WRITE(6,1150)C1(J),C2(J),E(J),W(J)
30   IF(C1(J).EQ.0.)GOTO 35
35   M=J-1
1000 FORMAT(2F10.3,F10.5)
1050 FORMAT(5X,F10.3,10X,F10.3,10X,F10.3)
1100 FORMAT(3F10.3,F10.5)
1150 FORMAT(5X,F10.3,10X,F10.3,10X,F10.3,10X,F10.5)
     MODE=1
     IDIM=40
```

```
      ICM=4
      DO 50 I=1,NP
      DO 40 J=1,NR
      N=NR-J
   40 A(I,J)=C(I)**N
   50 CONTINUE
      K=NP+1
      DO 100 I=K,M
      DO 80 J=1,NR
      N=NR-J
   80 A(I,J)=ABS(C1(I)**N-C2(I)**N)
  100 CONTINUE
      CALL LINLSQ(MODE,M,NR,A,IDIM,X,E,W,COVMAT,ICM,RES,U,IERR)
      DO 120 I=1,NR
  120 SIGMA(I)=SQRT(COVMAT(I,I))
      WRITE(6,1500)RES,IERR
      WRITE(6,1700)(X(I),SIGMA(I),I=1,NR)
 1500 FORMAT(1H1,//10X,*RESNMR=*,E9.03/10X,*IERR=*,I2//)
 1700 FORMAT(10X,*CALIBRATION PARAMETER*,5X,*UNCERTAINITY*,(/15X,E14.07,
     +10X,E14.07))
      WRITE(6,2000)
      DO 200 I=1,NP
      EJ=0.
      DO 150 J=1,NR
      N=NR-J
  150 EJ=EJ+X(J)*C(I)**N
      E(I)=EJ
```

```
200  WRITE(6,2100)C(I),E(I)
2000 FORMAT(//10X,*CHANNEL*,13X,*CALCULATED ENERGY*)
2100 FORMAT(10X,F10.3,10X,F10.3)
     STOP
     END
```

# *APPENDIX C*

## *APPARENT LIFETIME IN DELAYED COINCIDENCE*

The experimental lifetime of a $\gamma$-ray measured in delayed coincidence with background can be derived from the time distribution of the coincidence probability. The probability $P_c(t)$ of one $\gamma$-ray emitted at time t being followed by another $\gamma$-ray in no later than D ns after its emission would be

$$P_c(t) = P_1(t) \int_t^{t+D} P_2(t')\, dt' \tag{C-1}$$

where $P_1(t)$ and $P_2(t)$ are emission probability per unit time at time t of the first and second $\gamma$-ray, respectively. Consider the following three cases :

-- The general case in which the first $\gamma$-ray has a lifetime of $\tau_1$ and the second $\gamma$-ray lifetime is $\tau_2$. In this case the probabilities are expressed as

$$P_1(t)\, dt = \frac{1}{\tau_1} e^{-t/\tau_1}\, dt \tag{C-2}$$

$$P_2(t)\, dt = \frac{1}{\tau_2} e^{-t/\tau_2}\, dt \tag{C-3}$$

$$P_c(t)\, dt = \frac{1}{\tau_1} e^{-t/\tau_1}\, dt \int_t^{t+D} \frac{1}{\tau_2} e^{-t'/\tau_2}\, dt' \tag{C-4}$$

This equation is simply reduced to

$$P_c(t)\, dt = \frac{(1 - e^{-D/\tau_2})}{\tau_1} e^{-t\left(\frac{\tau_1+\tau_2}{\tau_1\tau_2}\right)} \tag{C-5}$$

From the above expression, the experimental lifetime $\tau_e$ is seen to be

$$\tau_e = \frac{\tau_1 \tau_2}{\tau_1 + \tau_2} \tag{C-6}$$

which is always smaller than or equal to either of the two lifetimes.

-- A constant-rate background is followed by a $\gamma$-ray with a real lifetime $\tau_2$. The $P_2(t)$ remains unchanged and the expression for background emission probability is the limit of $[C\tau_1 P_1(t)]$ as $\tau_1$ goes to infinity. Similarly, the time distribution of the coincidence probability for this case can be deduced from the expression (C-5) and is given as

$$P_c(t)\, dt = C(1 - e^{-D/\tau_2})e^{-t/\tau_2}\, dt \tag{C-7}$$

which indicates that in this case the experimental lifetime is equal to the lifetime of the second $\gamma$-ray.

-- The background is a combination of constant-rate and decaying components, namely,

$$P_1(t)\, dt = (C + \frac{1}{\tau_1} e^{-t/\tau_1})\, dt \tag{C-8}$$

In this case the experimental decay curve will consist of a combination of two exponentials with time constants of $\tau_2$ and $\frac{\tau_1 \tau_2}{\tau_1 + \tau_2}$, respectively.

It is easy to show that in the reverse situation, namely the situation in which a source $\gamma$-ray is followed by a background $\gamma$-ray, the experimental lifetimes will hold the same relations with the real lifetimes as we derived above.

*TECHNICAL INFORMATION DEPARTMENT*
*LAWRENCE BERKELEY LABORATORY*
*UNIVERSITY OF CALIFORNIA*
*BERKELEY, CALIFORNIA 94720*